Development of nanoscale sensors for scanning Hall probe microscopy and investigations of novel vortex phases in highly anisotropic superconductors

Mohammed, Hussen

Award date:
2015

Awarding institution:
University of Bath

Development of nanoscale sensors for scanning Hall probe microscopy and investigations of novel vortex phases in highly anisotropic superconductors

Submitted by

Hussen Ali Mohammed

A thesis submitted for the degree of Doctor of philosophy

Department of Physics

University of Bath

December 2014

COPYRIGHT

Signed:

Hussen Mohammed

Abstract

Bismuth Hall effect sensors with active sizes in the range 0.1μm - 2μm have been fabricated by electron beam lithography and lift-off techniques for applications in scanning Hall probe microscopy (SHPM). The key figures of merit of the sensors have been systematically characterised as a function of device size. The miniumum detectable field of 100nm probes at room temperature is found to be B_{min}=0.9mT/Hz$^{0.5}$, with scope for more than a factor of ten reduction by using higher Hall probe currents. This is significantly lower than in similar samples fabricated by focussed ion beam (FIB) milling of continuous Bi films, suggesting that the elimination of FIB damage and Ga^+ ion incorporation through the use of lift-off techniques leads to superior figures of merit. A number of ways in which the T=300K performance of our sensors could be improved still futher are discussed.

High resolution scanning Hall probe microscopy (SHPM) with semiconductor 2DEG Hall probe devices has been used to search for novel phases of vortex matter in single crystals of the high temperature superconductor $Bi_2Sr_2CaCu_2O_{8+\delta}$. In the crossing lattices regime of these highly anisotropic superconductors under tilted magnetic fields two orthogonal types of flux structure are formed known as Josephson and pancake vortices (JVs and PVs). SHPM has been used to study interacting JV-PV matter with very high in-plane fields. The spacing of JV chains has been systematically quantified as a function of both in-plane and out-of-plane fields. Surprisingly, it is found that the JV chain spacing is not solely a function of the in-plane field, as previously assumed, and the effective anisotropy, γ_{eff}, is shown to depend strongly on the out-of-plane field strength. Moreover, for a fixed in-plane field the JV stack spacing shows pronounced sawtooth-like oscillations as a function of the out-of-plane field. These measurements are giving us unique new insights into the properties of crossing vortex lattices in highly anisotropic cuprate superconductors at high Josephson vortex stack densities.

Acknowledgment

I am truly grateful to numerous people who have helped and encouraged me for my doctoral study at the University of Bath.

I would like to thank my supervisor Professor Simon Bending for his never-ending patience, encouragement, generous support, helpful guidance and understanding during my PhD project. Many thanks for Dr. Peter Curran's help including project discussions and the sharing of expertise. Also, I would like to thank the Iraqi government (Ministry of Higher Education) for funding and continuous care and support. Appreciations go to my wife and my children (Mena & Sima) as well as all other members of my family (Sabiha Ali and Nawzad Darweesh). I will not forget my wife (Nadia Darweesh) for her patience and continuous support. I am truly grateful to numerous people who have helped and encouraged me during my doctoral study at the University of Bath.

I am indebted to many colleagues that I have met during my studies at the University of Bath. A great deal of help was provided by the technicians; in particular I would like to thank, Dr. Sivapathasundaram Sivaraya and Dr. Stephen Wedge for their generous help with my research. In addition, my deepest thanks go to all members of the Physics Department, especially our group members for their many insightful discussions such as Dr. Sara Dale, Dr. Peter Curran, Wendy Lambson, Dr. Waled Desoky and Dr. Mohammed El Bana.

I would particularly like to express my deepest gratitude to my supervisor Prof. Dr. Simon Bending for his sincere supervision and valuable remarks regarding my research.

Common Symbols

$\mathbf{T_c}$	Critical Temperature
$\mathbf{H_c}$	The Critical Magnetic Field
$\boldsymbol{n}$	Carrier Concentration
$\boldsymbol{e}$	The Electronic Charge
J_c	Critical current density
$\boldsymbol{\sigma}$	The Surface Energy
$\boldsymbol{\mu}$	Carrier Mobility
$\boldsymbol{D}$	Diffusion Constant
$\mathbf{T}$	Temperature
$\boldsymbol{\psi(r)}$	Order parameter of Ginzburg–Landau (GL) theory
$\boldsymbol{\varepsilon_0}$	The Permittivity of Free Space
$\mathbf{H}$	The Magnetic Field Intensity
$\boldsymbol{\chi}$	The Magnetic Susceptibility
$\boldsymbol{B}$	The Magnetic Induction
$\boldsymbol{M}$	The Magnetisation
$\boldsymbol{H_c}$	The Critical Magnetic Field
$\boldsymbol{\lambda_L}$	Magnetic Field Penetration Depth
$\boldsymbol{\xi}$	Coherence Length
$\boldsymbol{A}$	The magnetic vector potential
Δf	The measurement bandwidth
$\boldsymbol{k_B}$	The Boltzmann constant
$\boldsymbol{I_c}$	Critical Current
$\boldsymbol{V_H}$	Hall Voltage

$H_{c2}(0)$ Upper Critical Field of Type II Superconductors

$\xi(0)$ Zero-Temperature Ginzburg-Landau Coherence Length

n_n The Normal Electron Density

n_s The superconducting Electron Density (superelectron density)

E The Electric Field

m The Electron Mass

v_s The Superelectron Velocity

j_s The Supercurrent Density

m^* The Mass Of The Cooper Pair

e^* The Charge Of The Cooper Pair

f_s The Free Energy Density of The Superconducting State

f_n The Free Energy Density of The Normal State

$H_{c1}(0)$ Lower Critical Field of Type II Superconductors

$\hbar$ Planck's constant ÷ 2π

κ The Ginzburg-Landau parameter

$\Delta(T)$ The energy gap

$\hbar\omega_D$ Phonon energy

Φ_0 Flux quantum

$\overrightarrow{F_L}$ The force per unit length on the flux line

$\vec{j}$ The current density

$\overrightarrow{\phi_0}$ Vector along the length of the vortex with the value of the flux quantum

$\vec{v}$ The velocity of the vortex

F_v The Force on a moving vortex

η The viscosity

γ	The anisotropy parameter
R_H	Hall coefficient
R_{off}	The offset resistance
$V_n(f)$	The noise voltage
V_J	The thermal Johnson noise
I_H	The Hall Current
V_n	Room temperature noise spectral density
B_{min},	The minimum detectable field
d_3	The piezoelectric coefficient
$\mathbf{F_e}$	The electric force
F_L	The Lorentz force
v_d	The drift velocity of the carriers
w	The width of the conductor
d	The sample thickness
Q	The total charge moving with the drift velocity
λ_F	Fermi wavelength
$H_{//}$	In-plane magnetic field
H_z	Out of plane magnetic field
PVs	pancake vortex stacks
JVs	Josephson vortex stacks
C_y	Distance between JVs
h	Thickness of piezo.

Table of Contents

List of figures

List of table

Chapter one

1.1. Structure of thesis

The thesis is divided into seven chapters: Before embarking on the main body of the work, a general overview of the thesis is presented in this introductory chapter. Chapter two covers the theoretical background of superconductivity, its basic theories such as the London equation, the Meissner effect, the Ginzburg-Landau and the Bardeen - Cooper - Schrieffer (BCS) theory of superconductivity, which are fundamental in describing the behaviour of superconductors. It includes the key concept of the distinction between type I and type II superconductors as well as the behaviour of vortices in High-Temperature Superconductors (HTS), e.g., $Bi_2Sr_2Ca_1Cu_2O_{8+\delta}$ (Bi-2212). Chapter two also covers two types of vortex matter in highly anisotropic $Bi_2Sr_2Ca_1Cu_2O_{8+\delta}$ (Bi-2212), Pancake vortices (PVs) and Josephson vortices (JVs). The Josephson coupling between pancake vortices (PVs) in adjacent CuO_2 layers is very weak and magnetic coupling dominates. In-plane fields only interact with PV stacks via this weak Josephson coupling. A homogeneous tilt of the PV stacks costs magnetic energy and for a wide range of applied field angles the ground state consists of coexisting, perpendicular Josephson and Pancake vortex lattices. As a result, Pancake vortices lying on stacks of Josephson vortices (JVs) become displaced due to interactions with the JV supercurrents leading to an attractive interaction.

In chapter three, the basic principles of magnetic imaging techniques are described (i.e., Bitter decoration, magnetic force microscopy (MFM), scanning superconducting quantum interference (SQUID) and scanning Hall probe microscopy (SHPM)) with a more detailed discussion of the principles of SHPM being presented. It is explained how Hall probes can be used to characterise the magnetic properties of superconductors and describes the low temperature scanning Hall probe microscopy (SHPM) technique which makes it possible to obtain local magnetic images of superconducting samples.

Bismuth Hall probe fabrication and characterisation is explained in detail in chapter four. Bi Hall effect sensors with active sizes in the range 0.1 - 2 μm have been fabricated by electron beam lithography and lift-off techniques for applications in

scanning Hall probe microscopy. Chapter five presents the characterisation of the nanoscale Bi Hall probes for two different Bi film thicknesses (50 nm and 70 nm) at 300K. The Hall coefficient, offset resistance, noise and minimum detectable fields are presented as a function of Hall cross active width and film thickness. Chapter six covers the results of SHPM imaging of decorated JV stack spacing as a function of both in-plane field and PV density. JV stacks can clearly be identified in the SHPM images via the PVs that 'decorate' them when small out-of-plane fields (H_z~0.5-10.0 Oe) are combined with very high in-plane fields ($H_{//}$~50-650 Oe). JV stack spacing has been systematically studied as a function of $H_{//}$ at fixed H_z, and as a function of H_z at fixed in-plane field. Finally, conclusions and future work are presented in chapter seven.

Chapter two

Superconductivity

2.1. Introduction to superconductivity

The study of superconductivity began with the discovery by Kamerlingh Onnes in 1911 that the resistance of mercury exhibits an abrupt drop to zero at 4.2K. This new phenomenon of zero resistance at low temperature was soon found in many other metals and alloys. It is well established that the electrical resistivity of a superconducting material is a function of temperature. The resistivity at high temperatures is dominated by phonon scattering, and so increases as temperature increases. However, at lower temperatures, the resistivity flattens off as the fixed amount of scattering from impurities and lattice dislocations etc becomes dominant. Once the resistivity drops to zero at low temperature, currents can flow without any voltage drop [1-3].

In 1933 Meissner and Ochenfeld discovered that a superconductor will expel magnetic flux at fields up to a critical field $\mathrm{H_c}$ at which point the superconducting state is destroyed [4]. For several decades theorists subsequently struggled to find a microscopic theory for superconductivity. In 1935, a major advances was made with the development of the London theory which consists of a set of equations that describe the Meissner effect and define the length scale over which the magnetic field can vary within a superconductor, the London penetration depth, λ_L [5]. Another leap forward was made by Ginzburg-Landau theory in 1950 [6]. Ginzburg and Landau discussed superconductivity based on the concept of an order parameter and characteristic superconducting length scales [7]. Using the G-L theory, Abrikosov showed that superconducting materials can be divided into two categories; type I and type II as defined by the G-L ratio, $\kappa = \lambda/\xi$. In type I superconductors $\kappa < \frac{1}{\sqrt{2}}$ and in type II $\kappa > \frac{1}{\sqrt{2}}$ [7]. In 1957, Bardeen, Cooper and Schieffer (BSC) presented a microscopic theory [8] which successfully explained superconductivity. The basis of this theory is the representation of the conduction electrons as a nearly free electron gas where the electrons interact pair-wise in a phonon mediated attractive potential. This theory was able to explain nearly all the electromagnetic properties of superconductors. The first superconductors were all pure elements or alloys with critical temperatures much lower than the boiling point

of liquid nitrogen (77K), which made experiments expensive, as they needed to be cooled in liquid helium.

In the eighties high temperature cuprate superconductors such as $YBa_2Cu_3O_{7-\delta}$ (YBCO), $Bi_2Sr_2Ca_1Cu_2O_{8+\delta}$ (Bi-2212) and $La_{5-x}Ba_xCuO_{5(3-y)}$ (LBCO), with critical temperatures as high as 133K were discovered, allowing greater experimental freedom as much cheaper liquid nitrogen cryostats can be used at this temperature.

The highest transition temperatures for a conventional superconductor was stuck at 23K in the compound Nb_3Ge, until Bednorz and Mueller reported possible superconductivity at a temperature of 30K in $La_{5-x}Ba_xCuO_{5(3-y)}$ in 1986. They had discovered copper-oxide superconducting materials which represented a new era of high temperature superconductivity HTSC that encouraged researchers to attempt to discover other compounds having high T_c [9]. Currently, the best known high T_c superconductors HTSs are $YBa_2Cu_3O_{7-\delta}$ with a T_c of 92K discovered in 1987,and the $Bi_2Sr_2Ca_2Cu_3O_{10+\delta}$ system with a T_c up to 110K discovered in 1988. Following their discovery, high-T_c superconductivity has been found in several other oxides such as $Tl_mBa_2Ca_{n-1}Cu_nO_{2n+m+2}$ (TBCCO) with transition temperatures as high as 125K and 135K in $HgBa_2Ca_2Cu_3O_{1+x}$ [10-12]. In 2001 Japanese scientists discovered the superconducting properties of MgB_2 which has a T_c of 39K [13]. In 2008, another Japanese group discovered Fe-based superconductivity in F-doping LaFeAsO, which has a T_c 26K [14,15]. Subsequently, the family of iron-based superconductors has become extremely interesting and is attracting a great deal of attention in the superconductivity community. Some of the known superconductors are illustrated in figure 2.1 [16].

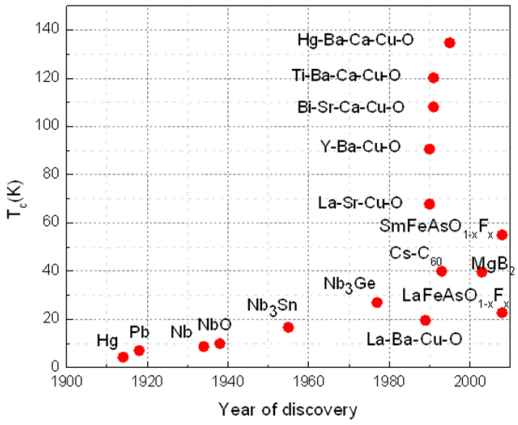

Figure 2.1: History of the superconducting materials discovered since 1911 [16].

2.2. Zero resistance

The phenomenon of superconductivity arises below a critical temperature, T_c at which a transition occurs to zero electrical resistance (c.f., figure 2.2). Therefore, it can be studied through experiments involving persistent supercurrents, which can last for many years. As well as the discovery of the zero resistance state, it was also found that when a superconductor is placed in a sufficiently strong magnetic field, superconductivity is destroyed. Superconductivity reappears when the applied magnetic field is removed. The minimum magnetic field required to destroy superconductivity depends on the shape and orientation of the sample at a given temperature. In practice, the superconducting state can be destroyed by raising the temperature above T_c, by applying a magnetic field in excess of a critical field, $H_c(T)$, or by passing a current in excess of a critical current density, $J_c(T,H)$. As shown in figure 2.4 [1].

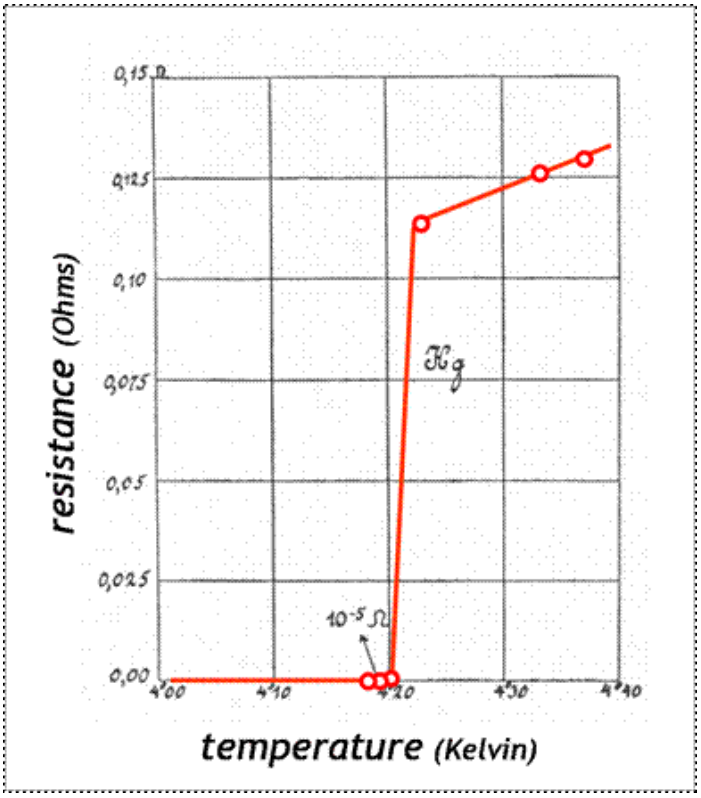

Figure 2.2 : Onnes' original data showing the superconducting transition temperature of mercury when the resistance drops to zero [1].

2.3. Meissner effect

It was not until 1933 that the next significant breakthrough was made and a second fundamental characteristic of superconductivity was discovered by Meissner and Ochsenfeld. The so- called Meissner effect is considered to be one of the defining characteristics of superconductivity. These authors found that, below the critical temperature, a superconducting material completely expels magnetic flux; in effect it displays the characteristics of a perfect diamagnetic [17,18]. This is illustrated in figure 2.3.

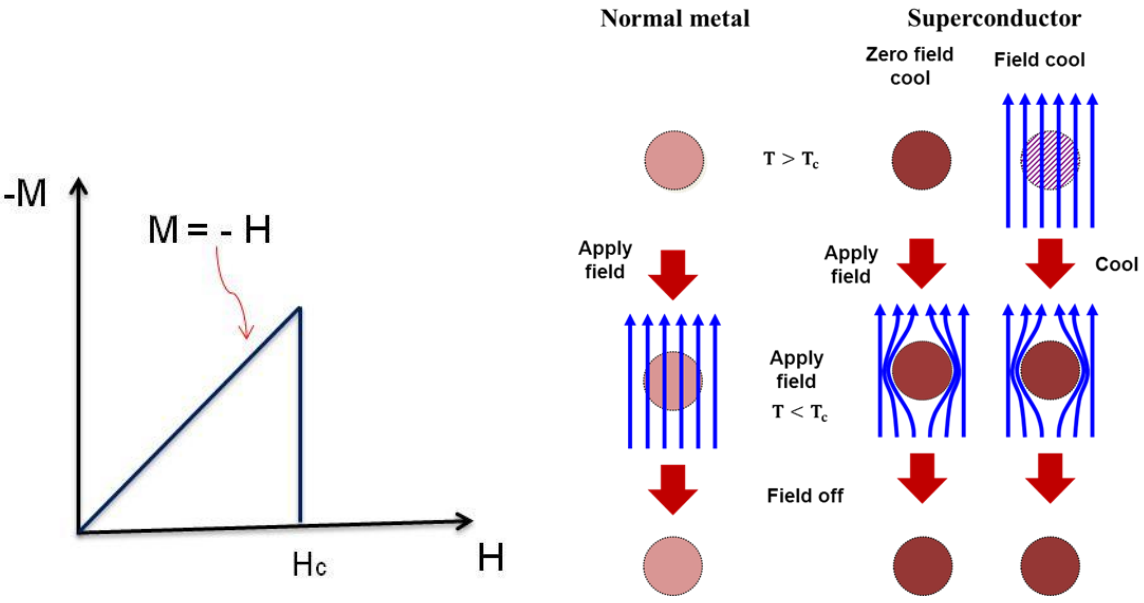

(a) (b)

Figure 2.3: (a) Magnetisation behaviour that arises due to the Meissner effect in a type I superconductor (b). The effect of Zero-Field Cooling and Field Cooling on a normal and a superconducting metal [19].

This complete expulsion of magnetic flux is understood to arise because of the zero resistance behaviour of the electrons. The applied field sets up supercurrents at the sample surface that generate fields that exactly cancel the applied field. At a critical magnetic field value superconductivity is destroyed and flux penetrates the material. The critical field, H_c, is temperature dependent and was empirically found to take the form:

$$H_c(T) = H_c(0)\left[1 - \left(\frac{T}{T_c}\right)^2\right] \quad , \tag{2.1}$$

where $H_c(0)$ denotes the critical field at zero temperature and T_c is the transition temperature of the superconductor.

The magnetic induction, B, and magnetic field, H, in the material medium are related by the equation

$$B = \mu_0 H + \mu_0 M = \mu_0(1+\chi) H, \qquad (2.2)$$

where M is the magnetization of the sample and μ_0 the permeability of the vacuum. The magnetization is proportional to the field and given by

$$M = \chi H \ , \qquad (2.3)$$

where χ is the magnetic susceptibility [20].

In the ideal case for a type I superconductor

$$M = - H \qquad \text{when } T < T_c .$$

As a result, the magnetization is equal and opposite to H. The medium is therefore diamagnetic, and the susceptibility χ = -1 as for a perfectly diamagnetic material. Hence, $B = \mu_0 H(1-1) = 0$ inside the superconducting sample and the magnetic field has been completely expelled from inside the sample.

The flux density does not fall abruptly to zero at the boundary of the superconductor however; but dies away within the region where the screening currents are flowing. The length scale over which B falls to zero is called the penetration depth, λ, which is of the order of 100 μm and much smaller than most superconducting samples [10].

In general, there are three critical parameters for the superconducting state, namely the critical temperature, T_c, magnetic field , B_c, and the current density, J_c, as shown in figure 2.4.

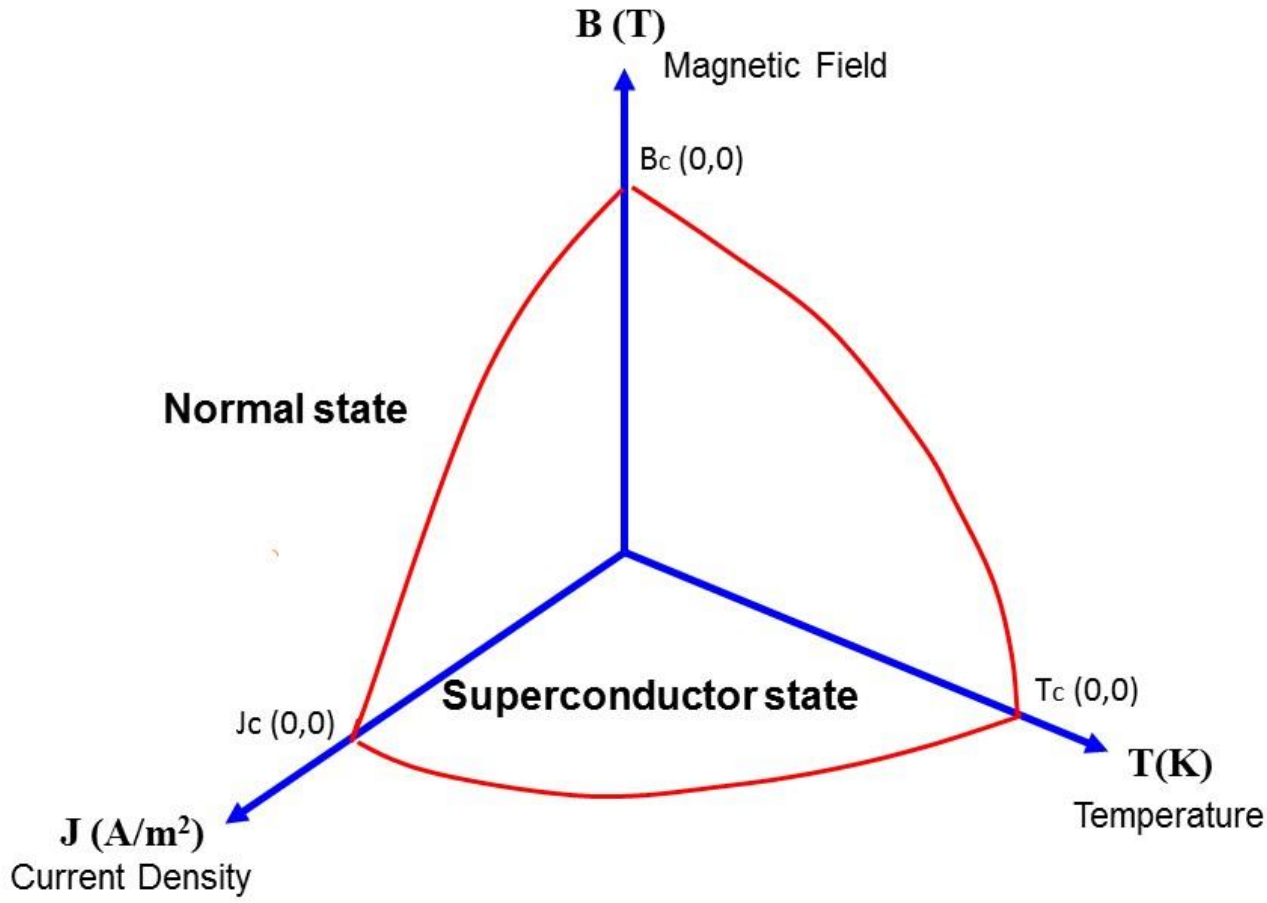

Figure 2.4: An illustration of the superconducting critical surface which is defined by the three critical parameters, J_c, B_c, and T_c.

2.4. London theory

The two basic phenomena of superconductivity are well described by the equations proposed by the London brothers in 1935. They realised that the currents responsible for the Meissner effect do not emerge naturally from Maxwell's equations and new equations were required [5]. The London equations are based on the principle of the two fluid model [21,22] in which there is a mix of two kinds of electron density, normal, n_n, and superconducting, n_s, the total density of free electrons being given by $n_{total} = n_n + n_s$.

The London brothers proposed two equations to describe the two fundamental phenomena of superconductivity [5]. Their development began with a description of the motion of superconducting electrons in an electric field, E, as given by

$$m\frac{dv_s}{dt} = eE, \tag{2.4}$$

where e is electronic charge, m, is electron mass and v_s, is superelectron velocity.

The supercurrent density can be defined as:

$$j_s = en_s v_s. \tag{2.5}$$

By substitution of equation 2.5 in equation 2.4, the first London equation becomes:

$$E = \frac{m}{e^2 n_s}\frac{dj_s}{dt}. \tag{2.6}$$

Equation 2.6 describes the zero resistance state (resistanceless), since any electric field accelerates the superconducting electrons rather than simply sustaining their velocity against resistance as described in Ohm's law in a normal conductor. By taking the curl of equation 2.6 and combining it with one of Maxwell's equations:

$$\nabla \times E = -\frac{dB}{dt}, \tag{2.7}$$

$$\frac{dB}{dt} = -\frac{m}{n_s e^2}\left(\nabla \times \frac{dj_s}{dt}\right). \tag{2.8}$$

In the Meissner state the magnetic flux within the superconductors must be a constant with a value of zero; this can be only the case if B dies away rapidly with

distance, so they assumed that equation 2.6 not only applies to dB/dt but to B itself.

$$B = -\frac{m}{n_s e^2}\nabla \times j_s. \tag{2.9}$$

Equation 2.7 is the second London equation which describes the diamagnetism exhibited by the superconductor. Using Maxwell's equation

$$\nabla \times B = \mu_0 j_s \tag{2.10}$$

and

$$\nabla \times (\nabla \times A) = \nabla(\nabla \cdot A) - \nabla^2 A, \tag{2.11}$$

equation (2.9) becomes

$$\nabla^2 B = \frac{1}{\lambda_L^2} B, \tag{2.12}$$

where the length scale λ_L (magnetic field penetration depth) is defined by:

$$\lambda_L = \sqrt{\frac{mc^2}{4\pi n_s e^2}}\,. \tag{2.13}$$

Here n_s , and λ_L are the number density of the superelectrons and the penetration depth respectively.

From equation 2.12, it can be seen that the external magnetic field decays exponentially with a characteristic length λ_L when a superconducting slab is in the presence of a magnetic field. In addition, the current density decays exponentially with the penetration depth to screen the magnetic field from the interior of the superconductor (c.f., figure 2.5) [23].

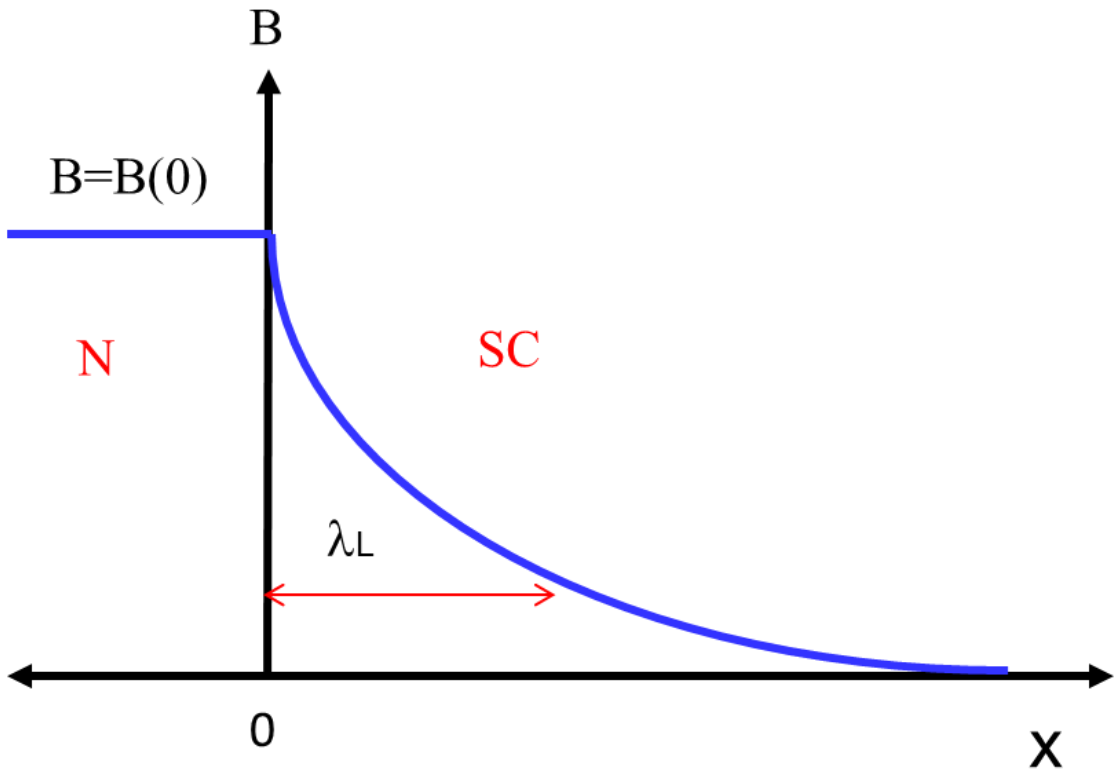

Figure 2.5: The London equation predicts the exponential decay of a magnetic field over a length scale λ_L into a superconductor occupying the region x> 0 .

Assuming that all the electrons are superconducting at T=0 and $n_s = n/2$ =10^{29} m^{-3}, a typical conduction electron concentration in a superconducting metal, one obtains

$$\lambda = \lambda_L(0) \sim \sqrt{\frac{m}{\mu_0 n \ e^2}} \sim 17 \text{ nm} . \qquad (2.14)$$

The London theory provides a good qualitative description of the Meissner effect, but is essentially a phenomenological, classical theory. Whereas they describe type I superconductors quite well they fail when the supercurrent density varies spatially, for example in type II superconductors and for thin films and high fields.

The London penetration depth is temperature-dependent and often well described by

$$\lambda_L(T) = \frac{\lambda_L(0)}{\sqrt{1-(\frac{T}{T_c})^4}}, \qquad T<T_c \qquad (2.15)$$

where $\lambda_L(0)$ is the value of the penetration depth at 0 K.

The London theory assumes that the penetration depth is independent of the strength of the applied field and the dimensions of the sample. However, in practice the superconducting condensate is also described by a second length scale, the coherence length, ξ, which is not present in the London model.

2.5. Ginzburg-Landau theory

The behaviour of type I and type II superconductors is much more rigorously described using the Ginzburg – Landau (GL) theory [24]. Although this is a better "quantum mechanical" description it remains, in essence, a phenomenological theory and not a true microscopic one like the later BCS theory. Ginzburg and Landau assumed a complex order parameter, $\psi(r)$, to describe the behaviour of the superconducting electrons where the density of the super electrons is given by

. $$n_s = |\psi|^2 \ . \qquad (2.16)$$

The superelectron density, n_s, varies with temperature and drops to zero at the critical temperature. Landau and Ginzburg sought a theory for a superconductor near the critical temperature,T_c, in terms of the difference in the free energy of the superconducting and normal states. Near T_c, the density of superelectrons is sufficiently small for it to be used as an expansion parameter. The free energy equation can then be expressed in terms of the series expansion

$$f_s = f_n + \alpha|\psi|^2 + \frac{\beta}{2}|\psi|^4 + \frac{1}{2m^*}\left|\left(\frac{\hbar}{i}\nabla - e^*A\right)\psi\right|^2 + \frac{\mu_o}{2}|H_a - H|^2. \qquad (2.17)$$

The first three terms on the right hand side come from Landau's theory of second order phase transitions. The fourth term describes the kinetic energy by analogy with Schrodinger quantum mechanics. The fifth term is the field energy. Here f_s is the free energy density of the superconducting state and f_n is the free energy density of the normal state, m^*, and e^* are the mass and charge of the Cooper pairs respectively .

We now know that $m^* = 2m$ and $e^* = 2\mathrm{e}$ for Cooper pairs.

In addition, α and β are G-L coefficients and A is the magnetic vector potential described by $B = \nabla \times A$.

If we now consider the case where $\psi \neq 0$ and there are no fields currents or gradients, equation 2.17 can be expressed as

$$f_s = f_n + \alpha|\psi|^2 + \frac{\beta}{2}|\psi|^4 \quad . \qquad (2.18)$$

$$f_s = f_n + \alpha\, n_s^* + \frac{\beta}{2}(n_s^*)^2$$

Minimising the energy with respect to n_s^* ($\frac{dF_s}{dn_s^*}$= 0) leads to the condition:

$$|\psi|^2 = -\frac{\alpha}{\beta} \quad , \tag{2.19}$$

and the minimum energy is given by $f_s = f_n - \frac{\alpha^2}{2\beta}$.

Hence β must be positive if the superconductor is to have lower energy.

There are two possible conditions for α. If α is positive, this corresponds to a minimum in the free energy at $|\psi|^2 = 0$ (the normal state). If α is negative, the minimum energy occurs at a finite value of ψ (the superconducting state).

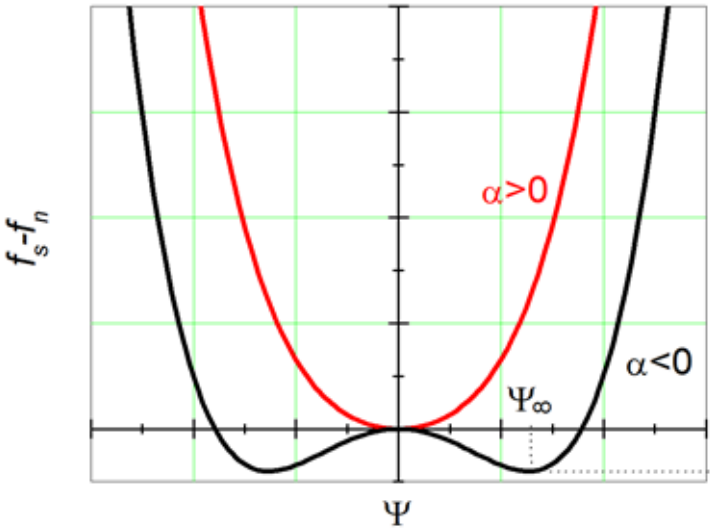

Figure 2.6: The free energy for the normal and superconducting states. In the normal state $\alpha > 0$ and there is one stable state, with an energetic minimum at $f_s - f_n = 0$. Only when $\alpha < 0$ does the order parameter have two stable non-zero states, at which the energy is equal to the condensation energy.

The most useful feature of GL theory for applications to inhomogeneous superconductors arises from the minimisation of the overall free energy of equation 2.17 by following a standard variational procedure, leading to the two Ginzburg-Landau equations:

$$\alpha\,\psi + \beta|\psi|^2\psi + \frac{1}{2m^*}\left(\frac{\hbar}{i}\nabla - e^*A\right)^2\psi = 0 \tag{2.20}$$

and

$$J_s = \frac{e^*\hbar}{2m^*i}\left(\psi^*\nabla\psi - \psi\nabla\psi^* - \frac{e^{*2}}{m^*}\psi^*\psi A\right), \tag{2.21}$$

where J_s, is the supercurrent density

Assuming no magnetic fields or currents equation 2.20 can be rearranged to give

$$\psi + \frac{\beta}{\alpha}|\psi|^2\psi - \frac{\hbar^2}{2m^*\alpha}\nabla^2\psi = 0 \tag{2.22}$$

This defines a second characteristic length scale for variations in the wave function called the coherence length,

$$\xi = \sqrt{\frac{\hbar^2}{2m^*|\alpha|}} \quad , \tag{2.23}$$

in addition to the penetration depth

$$\lambda_L = \sqrt{\frac{m\beta}{2\mu_0 e^2|\alpha|}} \quad . \tag{2.24}$$

The coherence length is the shortest length over which the order parameter can vary. These two characteristic lengths are crucial in determining whether a superconductor is type I or type II ,as shown in figure 2.7 [10].

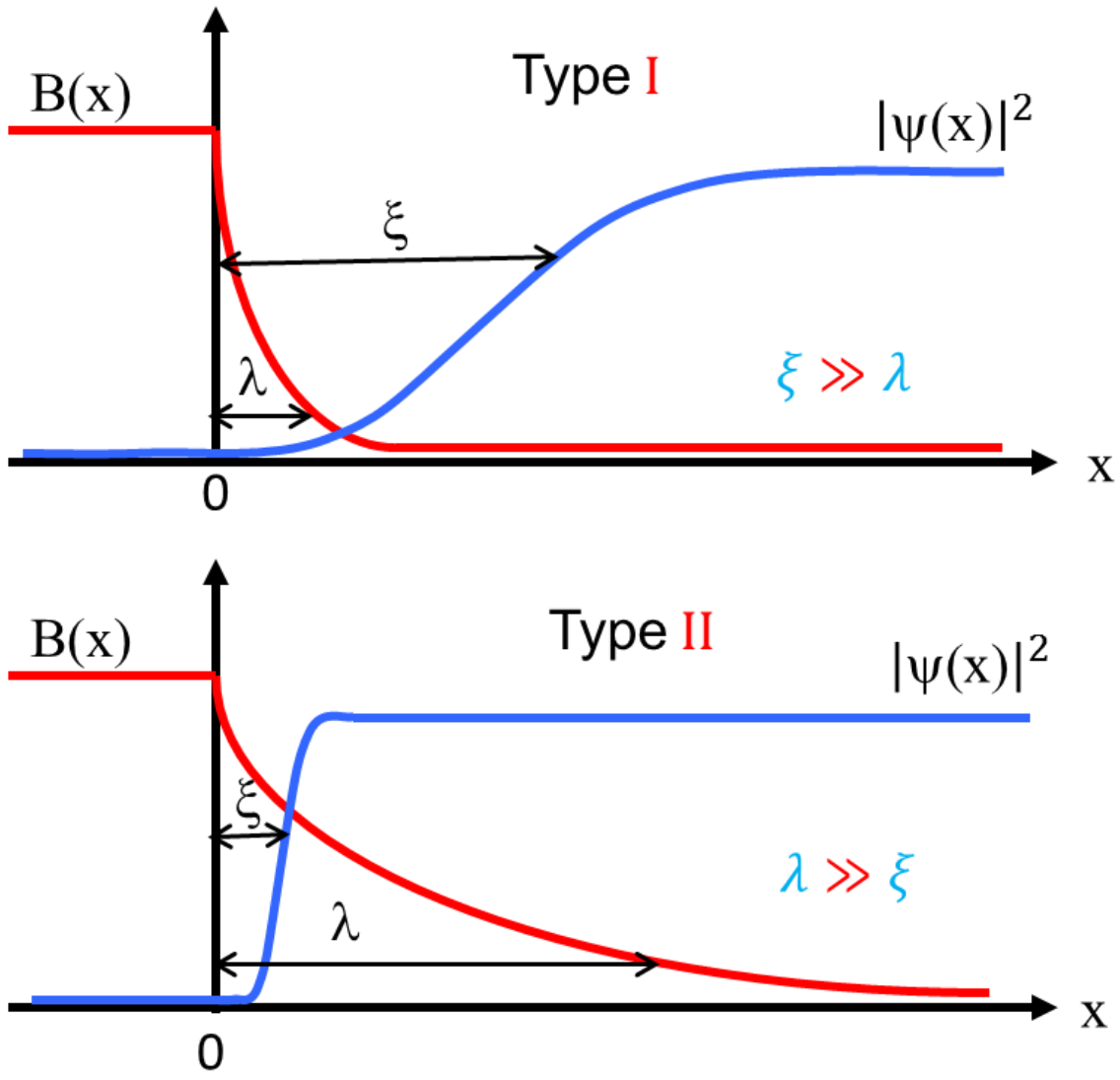

Figure 2.7: Schematic diagram of the variation of B and ψ at a superconductor-normal interface, where $\lambda \ll \xi$ for a type- I superconductor and $\lambda \gg \xi$ for a type-II superconductor [10,25] .

The ratio of penetration depth to the coherence length is called the GL parameter:

$$\kappa = \frac{\lambda(T)}{\xi(T)} \ . \qquad (2.25)$$

A superconductor is of type I or type II depending on whether κ is smaller or larger than $\frac{1}{\sqrt{2}}$.

The surface energy at the interface between normal and superconducting phases gives an additional contribution to the Gibbs free energy which is proportional to the

total area of the boundary between normal and superconducting phases within G-L theory.

$$\frac{1}{2}\mu_0 H_c^2 = f_n - f_s \quad . \tag{2.26}$$

The reduced volume of the superconducting region at the S/N interface leads to a positive contribution to the interface energy, given by $(f_n - f_s)A\xi$. On the other hand the additional penetration of the magnetic field at the interface leads to a negative contribution $-\frac{1}{2}\mu_0 H_c^2 A\lambda_L$ to the interface energy and, it is energetically advantageous to have interfaces between the two materials. Hence the net interface or surface energy is given by

$$\sigma \simeq \frac{1}{A}((f_n - f_s)A\xi - \frac{1}{2}\mu_0 H_c^2 A\lambda_L) \simeq \frac{1}{2}\mu_0 H_c^2(\xi - \lambda_L). \tag{2.27}$$

We see that, if the coherence length is longer than the penetration depth, the surface energy is positive. Alternatively, if the coherence length is shorter than the penetration depth, the surface energy is negative [26]. If $\sigma > 0$, (type I) interfaces are energetically unfavourable and if $\sigma < 0$ (type II) it becomes favourable to increase the amount of boundary. The latter situation generates a “mixed” state, also known as the Schubnikov phase, with coexisting regions of superconducting and normal material.

2.6. Bardeen Cooper Schrieffer (BCS) theory

The concept of pairs of electrons as being central to superconductivity was developed by Cooper in 1956. Cooper pairs involve bound pairs of electrons, each having equal but opposite spin and momentum. In conventional superconductors the pairs are bound together by an electron-phonon interaction [27]. In 1957, Bardeen, Cooper and Schrieffer fully explained all features of superconductivity by a microscopic theory in which they proposed that the electron-phonon interaction could lead to correlated electron pairs in the superconducting state [8]. Their microscopic model also allowed calculation of the energy gap and the coherence length [10]. Essentially, they showed that normal state electrons are unstable in the presence of an attractive electron-phonon interaction giving rise to a new correlated paired state.

Cooper pairs overcome their mutual repulsion by the polarisation (distortion) of the surrounding lattice. A fast moving electron will attract the lattice ions, leaving an apparent cloud of positive charge behind it which will attract the second electron. In this way they become bound with a separation characterised by the BCS coherence length, ξ_0. This indirect attraction can overcome the Coulomb force repulsion between the two electrons and they can become bound, as sketched in figure 2.8.

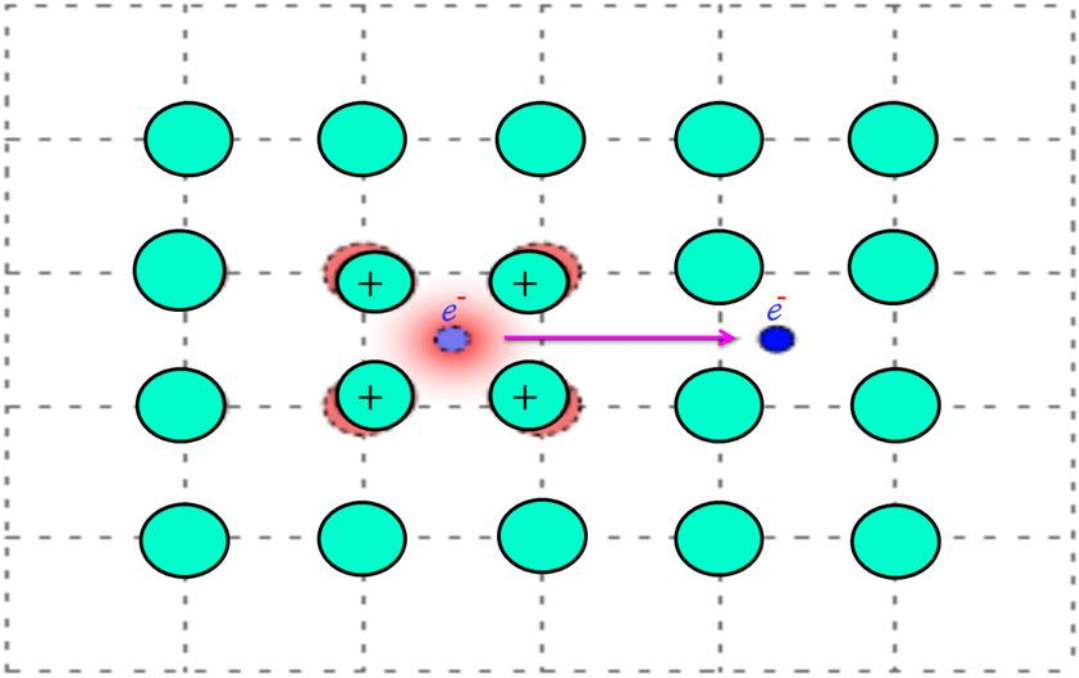

Figure 2.8: Schematic diagram of the formation of a bound Cooper pair via the electron-lattice interaction.

The quantum explanation for the Cooper pair, the key to zero resistance in the BCS model, is a rapid exchange of virtual phonons, a process called phonon-mediated attraction. The interaction between electrons is attractive when the electron states are less than a typical phonon energy $\hbar\omega_D$ from the Fermi surface [28,29]. The Cooper pair binding energy is maximum when they have opposite momenta $(k, -k)$, and the exchange correlation energy will be minimum when they have opposite spins (↑,↓). Electrons with opposite spin and momentum form an s-wave pair with zero angular momentum. For this configuration BCS theory predicts an energy gap which has the limiting value of $2\Delta(0) = 3.52\ k_B T_c$ in the weak coupling limit [30]. The temperature-dependent BCS energy gap, Δ(T), falls to zero at T_c, when Cooper pairs are destroyed [31].

2.7. Type I and Type II superconductors

Superconductors are classified as type I and type II superconductors according to their magnetization behaviour. However, both categories have one common feature; the resistance vanishes below the critical temperature T_c [7]. Type I materials are usually pure metals which display a complete Meissner effect up to a certain critical field, H_c, when the sample becomes normal. The behaviour as a function of applied field and temperature is shown in figures 2.9 (a), (c) [32]. Type II superconductors are usually made of compounds and characterized by two critical fields, the lower critical field, H_{c1}, below which the magnetic flux is completely expelled (Meissner state) and the upper critical field, H_{c2}, above which the superconductor reverts fully to the normal state. Between the lower and upper critical field they exhibit a so-called mixed state. In the mixed state, type II superconductors contain a lattice of small regions of non-superconducting or "normal" material called vortex cores, as shown in figure 2.9 (b), (d). The mixed vortex state is an intrinsic feature of type II superconductors and exists for magnetic fields such that $H_{c1} < H < H_{c2}$. Vortices allow the magnetic field to penetrate the sample to lower the magnetostatic energy. Penetration occurs in the form of tubes of quantised magnetic flux contained in a normal core surrounded by circulating supercurrents that shield the magnetic field. Two characteristic length scales must now be introduced to describe the spatial variation of the magnetic field and the density of superconducting charge carriers within a superconductor.

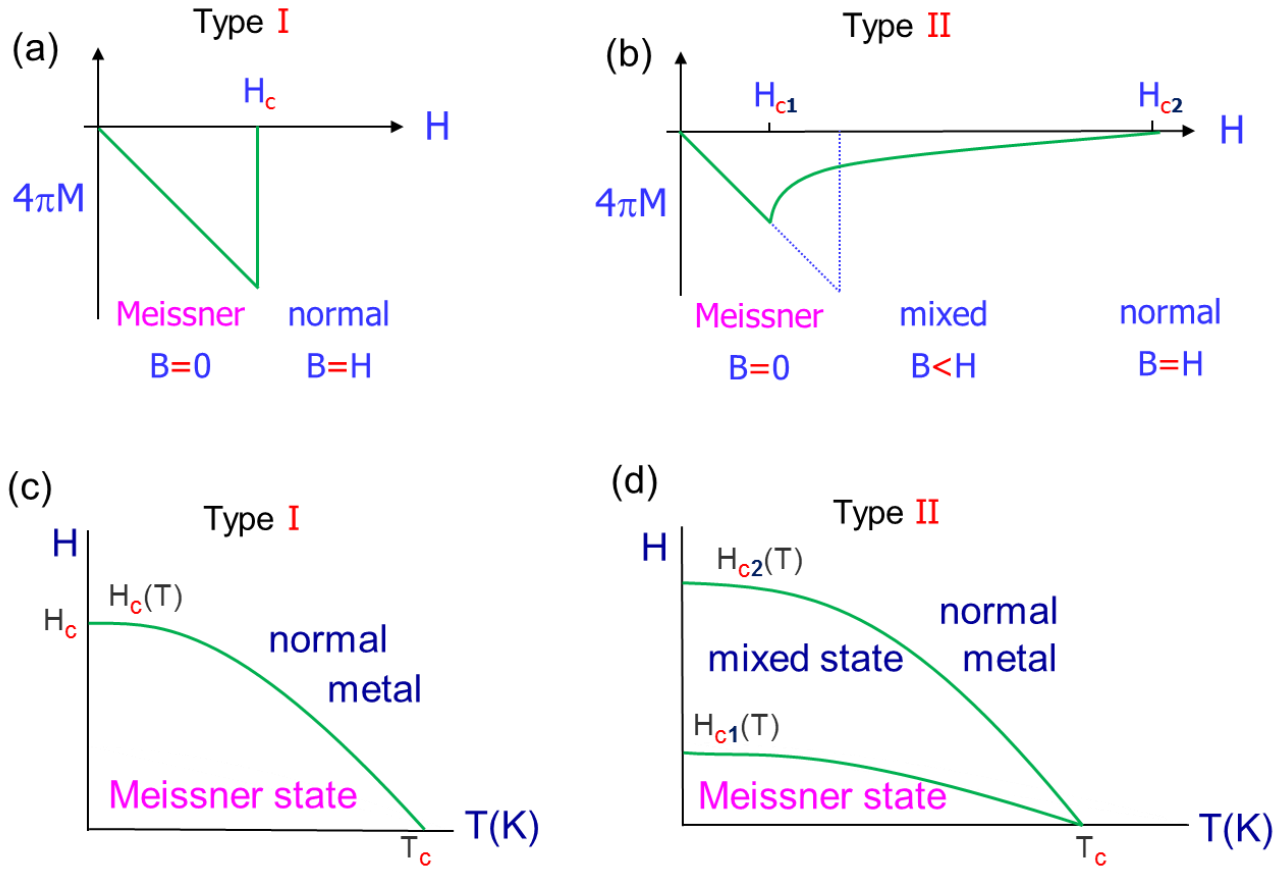

Figure 2.9: Magnetization behaviour of (a) type I and (b) type II superconductors. (c), (d) show the H-T phase diagrams for type I and type II superconductors respectively [33].

2.8. Introduction to vortices and vortex matter in conventional type II superconductors

We have seen that in a type II superconductor, the wall energy is negative and a mixed state (vortex state) exists above Hc_1 when flux penetrates in the form of cylindrical tubes, called vortices or flux lines (FLs) containing a single flux quantum, $\Phi_0 = {}^{h}/_{2e} = 2.068 \times 10^{-15}$Wb, [34] (c.f., figure 2.10 (a)).

The core of a vortex is non superconducting and contains the magnetic field and is enclosed by circulating superconducting currents. The number of vortices increases with applied field until superconductivity is destroyed at the upper critical magnetic field, Hc_2 [35]. The critical fields Hc_1 and Hc_2 can be calculated using the following equations [36,37]

$$Hc_1 = \frac{\Phi_o}{4\pi {\lambda_L}^2}, \qquad (2.28)$$

and

$$Hc_2 = \frac{\Phi_o}{4\pi \xi^2} \quad . \qquad (2.29)$$

Hence the Ginzburg-Landau parameter, κ, can also be approximately described [38]

$$\kappa^2 \approx \frac{H_{c2}}{H_{c1}} \quad . \qquad (2.30)$$

The interaction between two adjacent vortices is mutually repulsive. The supercurrent of one vortex acts on the magnet flux of the other to generate a repulsive Lorentz force.

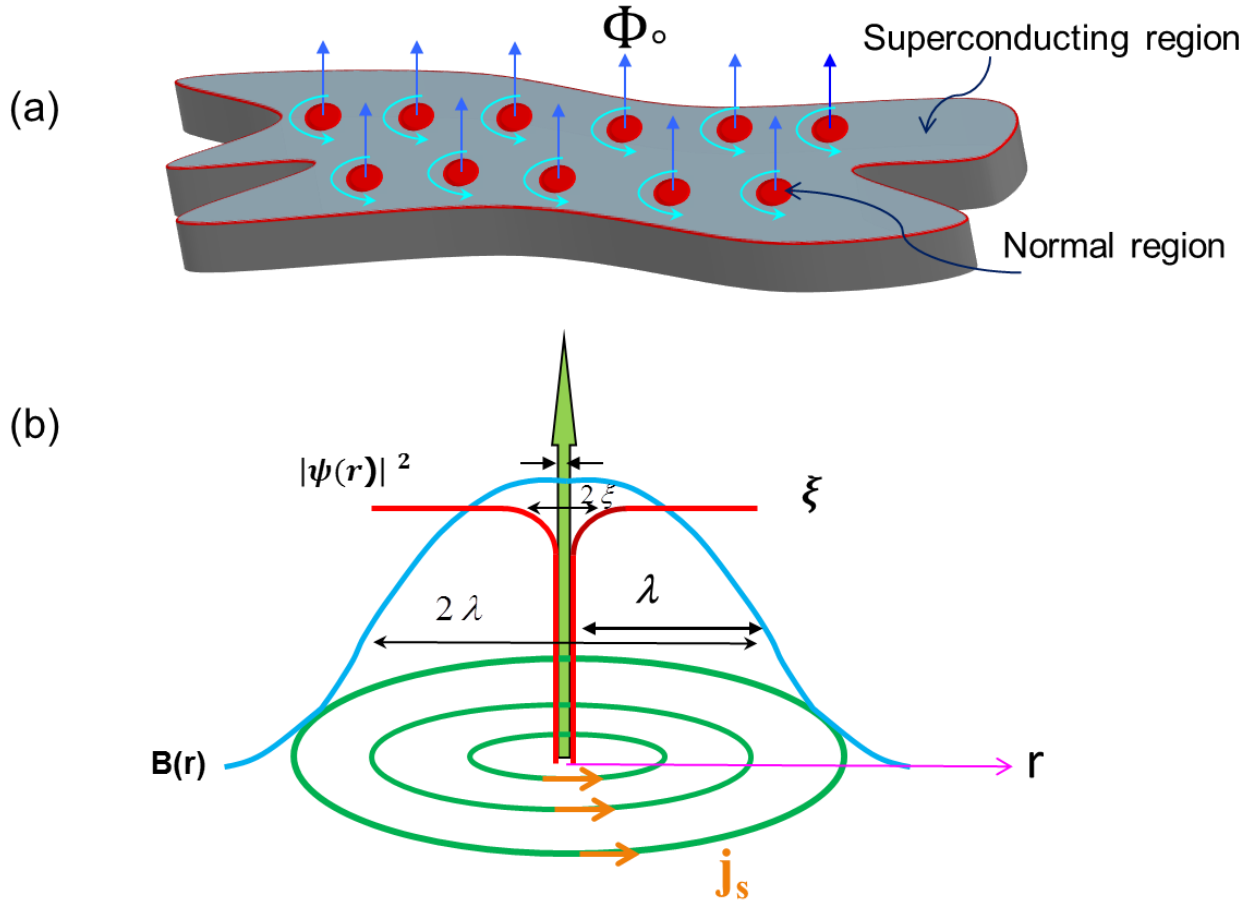

Figure 2.10: (a) Sketch of an Abrikosov vortex lattice vortex composed of lines of flux surrounded by a circulating supercurrents. (b) The magnetic flux density and current density for a single vortex as a function of radius r from centre of the vortex core.

In 1957, Abrikosov used G-L theory to predict the existence of vortices in type II materials. He showed that in an idea sample these form a lattice-like structure in the material [39] as shown in figure 2.11.

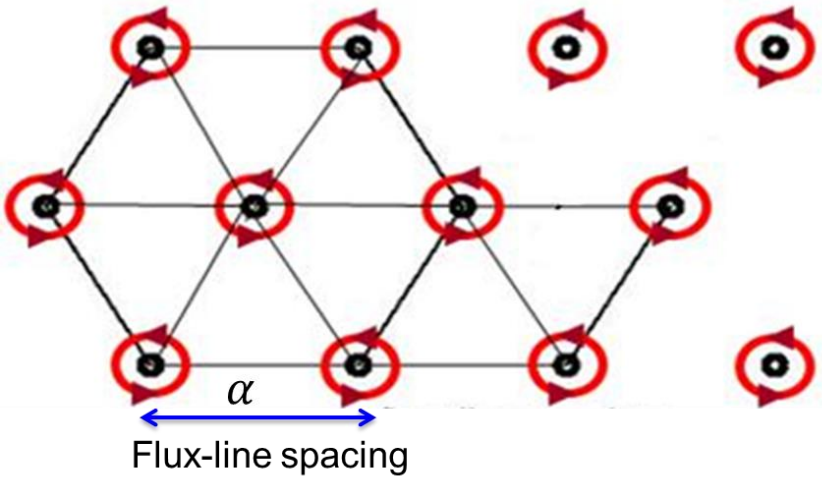

Figure 2.11: Sketch of part of a triangular Abrikosov vortex lattice.

For the triangular vortex lattice, which is expected to have the lowest energy, the lattice parameter is given by [40] .

$$\alpha = \sqrt{\frac{\sqrt{3}}{2}\frac{\Phi_0}{B}} \tag{2.31}$$

As B is increased, the lattice spacing reduces until when the applied field approaches Hc_2 the vortices begin to strongly overlap, at which point the superconductor becomes normal.

2.8.1 Vortex pinning and vortex motion

In an ideal type II superconductor, vortices move under the Lorentz force due to a transport current. However, most type II superconductors contain imperfections, such as dislocations, grain boundaries and inhomogeneities, which are known to act as vortex pinning centres. These impede the motion of flux vortices and oppose the Lorentz force. In order to obtain high critical currents in type II superconductors, the maximum pinning forces should be produced in the material by introducing metallurgical defects, such as point, line, surface and volume defects. Optimum pinning occurs when the defect size is comparable to the vortex core size. If the defect size is smaller than the core size, the core can cover several defects at once, averaging out their effect and typically drastically reducing the pinning force [41].

The Lorentz force on any flux line due to an applied supercurrent density is given by

$$\overrightarrow{F_L} = (\vec{J} \times \overrightarrow{\phi_0}), \tag{2.32}$$

where, $\overrightarrow{F_L}$ is the force per unit length on the flux line, $\vec{J}$ is the current density and $\overrightarrow{\phi_0}$ is a vector along the length of the vortex with the value of the flux quantum. The resulting flux line motion is perpendicular to the current flow leading to the generation of an electric field described by

$$\vec{E} = \vec{B} \times \vec{v}, \tag{2.33}$$

where $\vec{v}$ is the velocity of the vortex.

The vortices will not move if the Lorentz force is less than the characteristic pinning force. However, at a critical current density, J_C, when the Lorentz force exceeds the pinning force, vortices start to move freely through the sample giving rise to dissipation and resistance. In general, the friction force that opposes the motion of a vortex is defined by [42]

$$F_\nu = \eta\nu \tag{2.34}$$

Hence

$$F\nu = F_L - F_{p=} \eta\nu \quad ,$$

$$\eta\nu = (\hat{J} \times \hat{\Phi_0}) - (\hat{J}c \times \hat{\Phi_0}) = (\hat{J} - \hat{J}c) \times \hat{\Phi_0} \quad . \tag{2.35}$$

Hence

$$\nu = (\hat{J} - \hat{J}c) \times \Phi_0^{\wedge} \times \frac{1}{\eta} \quad . \qquad (2.36)$$

Where Ƞ, is the vortex viscosity [43]. In some cases, even if the Lorentz force is smaller than the pinning force, the flux vortices may move very slowly. This phenomenon is called flux creep whereby vortices hop between pinning sites [44,45], (c.f., figure 2.12).

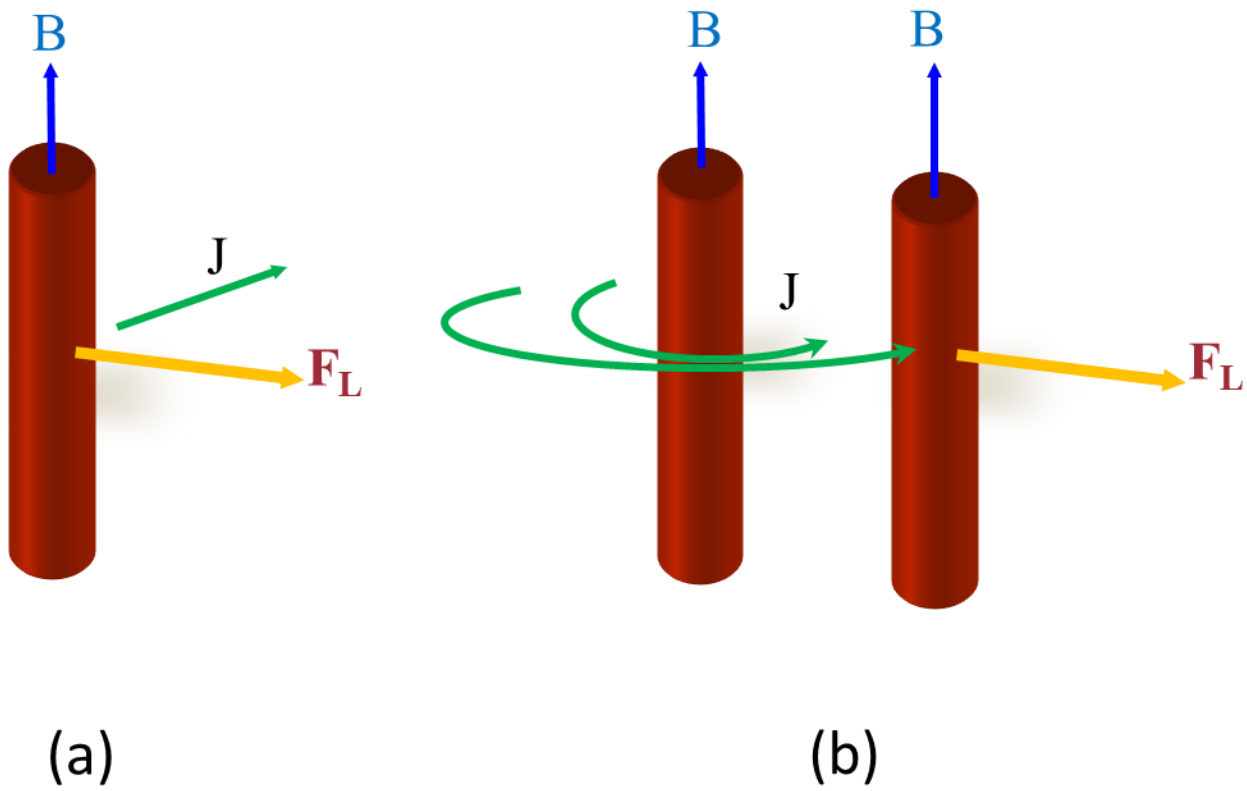

Figure 2.12: Schematic diagram showing (a) the Lorentz force driven vortex motion and (b) mutual vortex-vortex repulsion.

2.9. High-Temperature Superconductors (HTS) and the structure of $Bi_2Sr_2Ca_1Cu_2O_{8+\delta}$

High temperature superconductivity (HTS) refers to superconductivity at temperatures greater than 30K. Despite the obvious advantages of a high temperature superconductor, it was not until 1986 that a real jump in the highest known critical temperature was made when Bednorz and Muller first discovered the copper oxide based superconductors. From 1911 until 1986 the maximum critical temperature had been 23.1K for Nb_3Ge discovered by Gavaler [35]. In the space of seven years following 1986 this had leaped to 138 K, all such superconductors being based upon the copper oxides [46]. One prominent feature of all copper oxide high temperature superconductors is the anisotropy of their structure. They also have small coherence lengths combined with relatively large penetration depths, resulting in large values of the Ginzburg-Landau parameter, making them extreme type II [47]. Two of the best known materials are $YBa_2Cu_3O_{7-\delta}$ and $Bi_2Sr_2Ca_1Cu_2O_{8+\delta}$. The electrical conductivity in the CuO_2 planes is very high, while in the direction normal to the CuO_2 planes it is very poor. As a result all physical properties are highly anisotropic. The large anisotropy of HTSC's and the fact that supercurrents are mainly carried in the Cu-O planes means that in certain regions of the phase diagram superconductivity is highly two dimensional.

2.9.1 The structure of $Bi_2Sr_2Ca_1Cu_2O_{8+\delta}$

For this project the focus is on the cuprate $Bi_2Sr_2Ca_1Cu_2O_{8+\delta}$, abbreviated as Bi-2212. Bi-2212 is one of the most important cuprate HTS materials and consists of Bismuth (Bi), Strontium (Sr), Calcium (Ca) ,Copper (Cu) and Oxygen (O). The critical temperatures (T_c) of the Bi family of compounds varies from 10K for $Bi_2Sr_2Cu_2O_{6+\delta}$, through 90K for $Bi_2Sr_2Ca_1Cu_2O_{8+\delta}$ to 110K for $Bi_2Sr_2Ca_2Cu_3O_{10+\delta}$. Table 2.1 shows the critical temperatures of various cuprate high temperature superconductors.

Superconductor	T_c (K)
$Hg_{0.8}Tl_{0.2}Ba_2Ca_2Cu_3O_{8.33}$	138
$HgBa_2Ca_{1-x}Sr_xCu_2O_{6+\delta}$	123
$HgBa_2CuO_{4+\delta}$	94
$Tl_{0.5}Pb_{0.5}Sr_2Ca_2Cu_3O_9$	120
$Tl_2Ba_2Ca_3Cu_4O_{12}$	112
$Bi_2Sr_2Ca_2Cu_3O_{10}$	110
$Bi_2Sr_2CaCu_2O_8$	90
$GdBa_2Cu_3O_7$	94
$YBa_2Cu_3O_{7+\delta}$	93
$YbBa_{1.6}Sr_{0.4}Cu_4O_8$	78

Table 2.1: Critical temperatures of various cuprate high temperature superconductors (HTS).

A unit cell of Bi-2212 is shown in figure 2.13 including the alternation between conducting CuO_2 layers and charge reservoir layers containing Bi and Sr. The charge reservoir layers play a crucial role in controlling the value of T_c as they donate mobile holes to the CuO_2 planes [48,49].

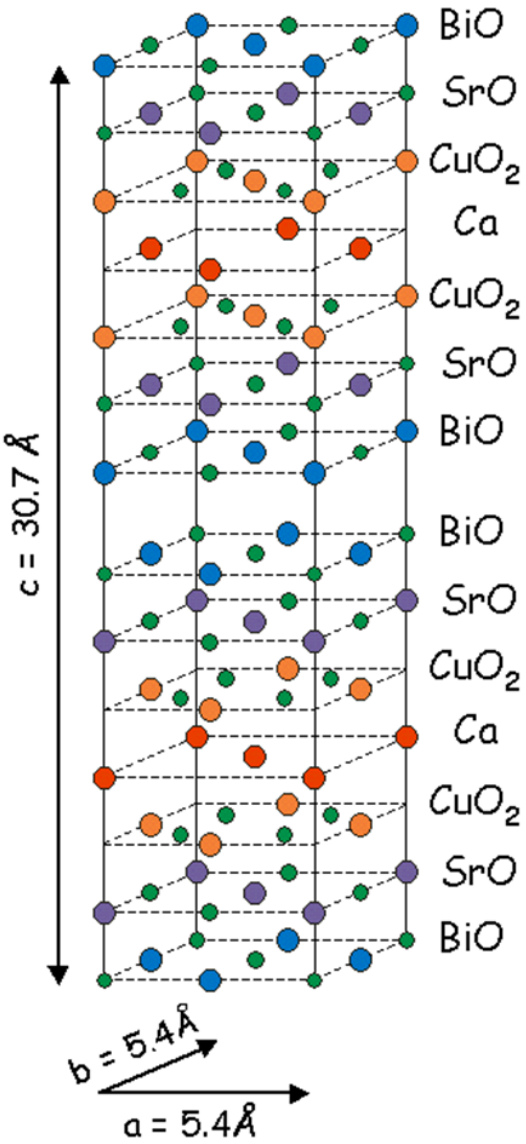

Figure 2.13: The tetragonal unit cell of $Bi_2Sr_2CaCu_2O_{8+\delta}$.

Bi-2212 is characterised by its relatively long penetration depth $\lambda_{ab} \sim 230$ nm and the short coherence length $\xi_{ab} \sim 1$ nm for transport in the a-b plane at T=0 [50]. The anisotropy parameter is therefore given by [51].

$$\gamma = \frac{\sqrt{m_c}}{\sqrt{m_{ab}}} = \frac{\lambda_c}{\lambda_{ab}} = \frac{\xi_{ab}}{\xi_c} \sim 500 \, . \qquad (2.37)$$

Here m_c and m_{ab} are the out-of-plane and in-plane effective masses.

2.10. Vortex matter in highly anisotropic $Bi_2Sr_2Ca_1Cu_2O_{8+\delta}$; Pancake Vortices (PVs) and Josephson Vortices (JVs)

In high temperature superconducting cuprates the coherence length is very short, leading in turn to a very small vortex core. However, the penetration depth is relatively large $\lambda \approx$100-200 nm, making them extreme type II materials. In addition their layered structure often results in very high anisotropy. Bi-2212 shows the largest crystalline anisotropy of all known cuprate HTS. This leads to pronounced anisotropy of the vortices. For a magnetic field applied perpendicular to the superconducting CuO_2 layers, H_z, stacks of 2D pancake vortices (PVs) are created in the CuO_2 planes which are only weakly coupled along the c-axis direction [26,52,53].

In contrast if the field is applied parallel to the CuO_2 planes, H_{ab}, Josephson vortices (JVs) are created. These are centered on the normal spaces between CuO_2 planes and have highly elongated elliptical current distributions. PVs and JVs are illustrated in figure 2.14 [26,54,55].

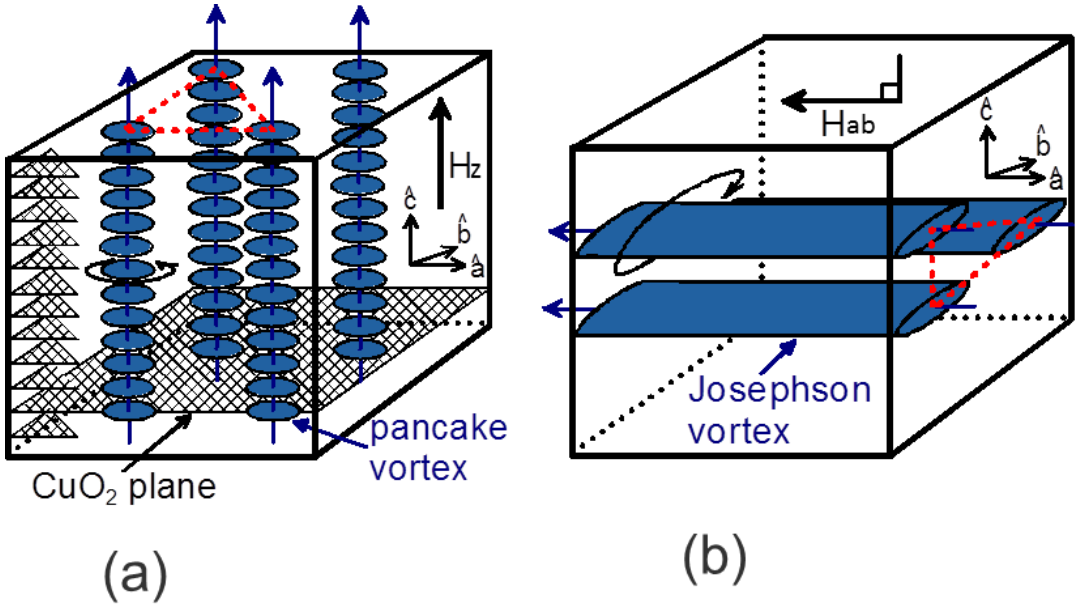

Figure 2.14: Sketches of vortex structures in Bi-2212 from reference [56].

(a) With the magnetic field applied along the high-symmetry c-axis, vortices formed of vertical stacks of 2D pancake vortices order into an Abrikosov lattice.

(b) With the magnetic field parallel to the a-b planes, Josephson vortices order into a highly elongated rhombic lattice.

Josephson vortices (JVs) differ from Abrikosov pancake vortices as they have no normal cores. Supercurrents circulate around their centres and are composed of supercurrents flowing within CuO_2 planes and “Josephson” currents flowing between the planes.

2.11. Crossing JV/PV vortex lattices in Bi-2212

The crossing lattices regime exists under tilted fields when the two orthogonal flux structures, pancake and Josephson vortices, coexist [57,58] as shown in figure 2.15. A weak attraction exists between these two sub-lattices leading to one dimensional pancake vortex chains that become trapped on JV stacks. PV/JV attraction under tilted fields arises from PV displacements driven by the underlying JV supercurrents leading to a kink structure around the intersection with the JV [59]. Mutual repulsion prevents PV stacks from passing one another along the length of the trapped chains. For small tilt angles tilted vortices composed of PVs linked by short JV segments can be stable [60].

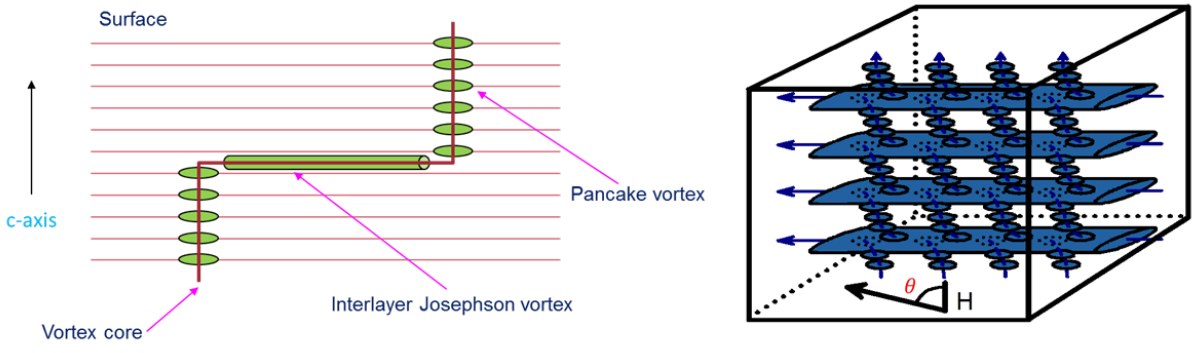

Figure 2.15: (a) A flux vortex in a tilted field in an anisotropic HTSC [58,61].

(b) PV stacks intersecting a JV stack with the applied field tilted at an angle θ with respect to the c-axis [56].

Chapter three

Introduction to Magnetic imaging & Scanning Hall Probe Microscopy

3.1. Introduction to magnetic imaging techniques

There is a wide range of complementary magnetic imaging techniques which all have their strengths and weaknesses. Key figures of merit include the spatial resolution and minimum detectable field. In addition techniques vary with respect to their degree of invasiveness and the ability to extract quantitative formation from images. Finally, some approaches lend themselves to measuring other parameters than the magnetic field, for example the magnetic susceptibility or other dynamic magnetic properties [62]. There are several forms of scanning probe microscopy for magnetic imaging including Magnetic Force Microscopy (MFM), Scanning Hall Porbe Microscopy (SHPM) and Scanning Superconducting Quanum Interferometer Device (SSQUID) microscopy. SSQUID microscopy has the lowest minimum detectable fields; however its spatial resolution is usually poor. MFM has higher spatial resolution, but the tip's stray magnetic field can be invasive. SHPM represents a good compromise with high spatial resolution combined with low minimum detectable fields. The highest spatial resolution is exhibited by Lorentz (electron) microscopy, while the highest field resolution is exhibited by scanning SQUID microscopy. Figure 3.1 shows, a comparison of minimum detectable field and spatial resolution for leading magnetic imaging techniques [26]. The equivalent flux sensitivity is shown in the figure by the diagonal lines.

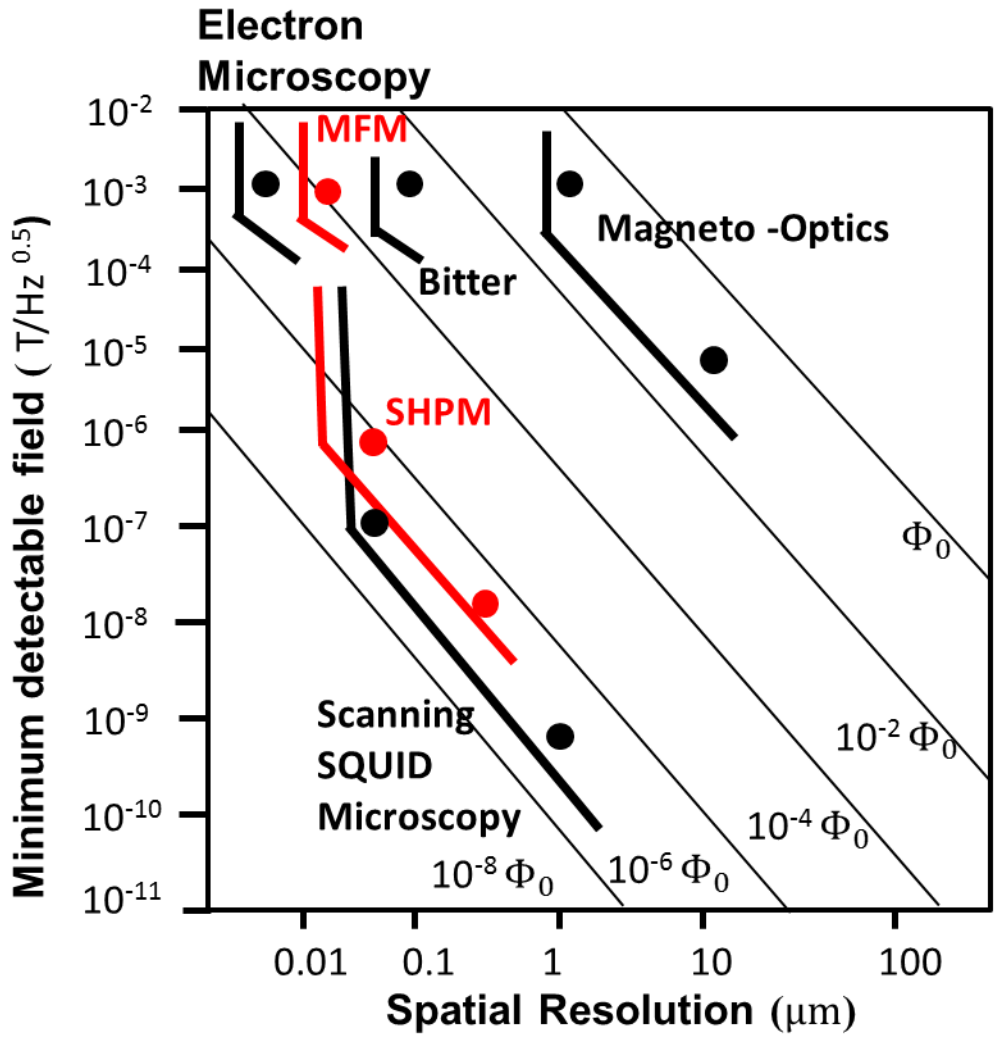

Figure 3.1: A comparison of the minimum detectable field and spatial resolution of the principal magnetic imaging techniques [Adapted from Simon J. Bending, Advances in Physics **48**, 449 (1999)].

3.2. Comparison of magnetic imaging techniques.

3.2.1 Lorentz microscopy

Lorentz microscopy depends on the deflection of the path of an electron beam by a magnetic field. Electrons passing through the sample are deflected in various directions depending on the local magnetic induction. In this case a scanned electron beam replaces the scanned probe techniques. This method only works if stray field components perpendicular to the beam are present, otherwise no net deflection can be achieved. In Lorentz microscopy, the electrons emitted from the filament are accelerated to high energies around ~200 KeV to 1MeV, allowing magnetic contrast to be achieved in a transmission electron microscope (TEM). While the ultimate spatial resolution for studying magnetic fields is lower than when imaging the physical structure of the sample, it allows correlation of the two, for example, linking defects in the sample with the behaviour of vortices. One of the major advantages of Lorentz microscopy is that it is possible to image vortices at video frame rates, collecting tens of images per second. However, the sample must first be thinned (≤400nm) to the extent that it is electron transparent [63,64].

3.2.2 Bitter decoration

The first technique developed to image ferromagnetic structures was Bitter decoration which was initially demonstrated in 1930 [65]. In 1967, Essman and Trauble used this method to make the first observation of the Abrikosov vortex lattice [66]. In this approach, fine magnetic particles are dispersed on the magnetic structure by various techniques, for example by evaporation or liquid suspension. These particles migrate to the regions of highest magnetic field, mirroring the underlying magnetic structure. The pattern is then imaged using optical microscopy or a scanning electron microscope (SEM) depending on the size of the features [65]. The Bitter decoration technique has proved valuable for observing the static magnetic flux-line lattice (FLL) in high critical temperature superconductors. In this case a ferromagnetic filament of iron, nickel or cobalt is mounted roughly 3 cm away from the sample. In a low pressure of helium gas a sufficiently large current is passed through the filament so that it vaporizes and the particles travel to the sample

and deposit on to it. During deposition the magnetic particles move along maximum field gradients and 'stick' at the vortex cores where the magnetic field is highest. Consequently, the deposited sample provides information about the FLL after warming up and imaging with an SEM [67]. The spatial resolution of the technique depends upon the size of the particles (typically ~ 10 nm) and hence yields little quantitative information about vortex structures. The Bitter decoration method is only appropriate for low magnetic fields below $\sim$ 10mT [68] and it has the disadvantage that the sample has to be cleaned before being reused because the magnetic particles remain van der Waals bonded on the surface [69]. In 1991, Bolle *et al*, captured an image of the vortex lattice in a $Bi_2Sr_2Ca_1Cu_2O_{8+\delta}$ single crystal which had been decorated in a tilted field of 3.5mT (c.f., figure 3.2). Vortex chains are clearly visible in this image reflecting new vortex structures present in Bi-2212 under tilted fields [70].

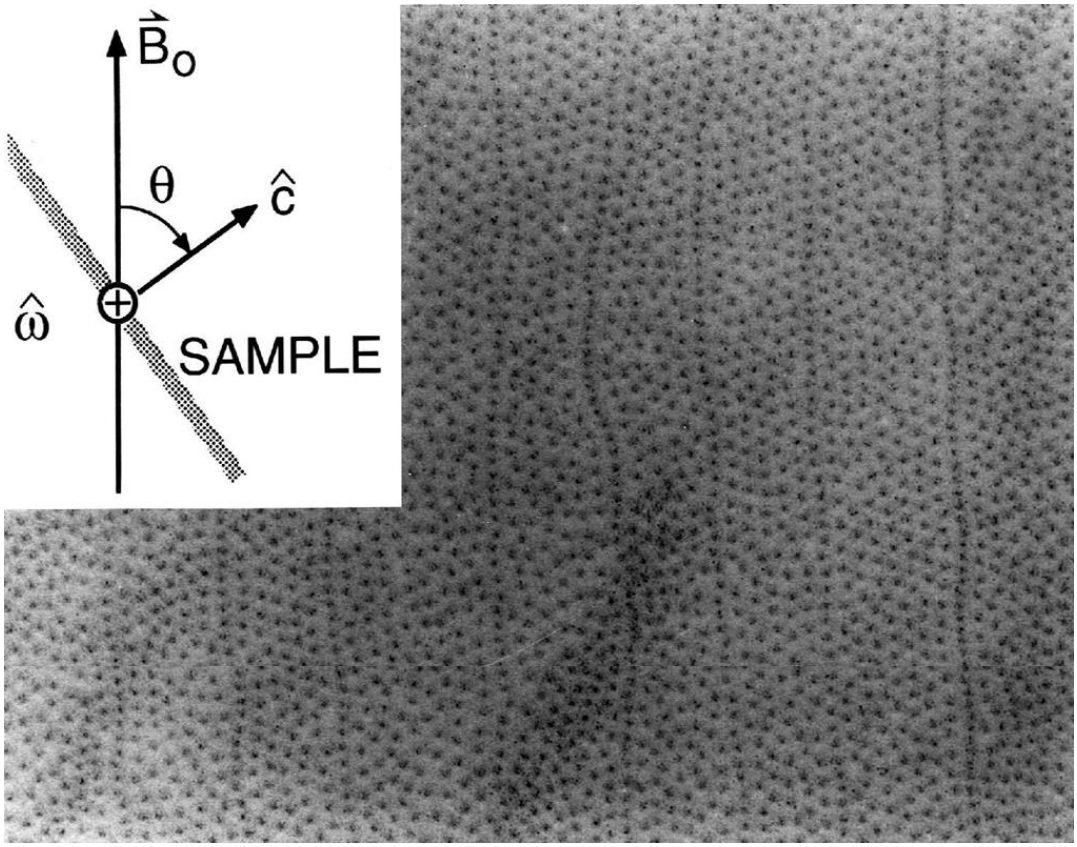

Figure 3.2: The vortex pattern in a Bi-2212 single crystal imaged by the Bitter decoration technique with a 3.5mT magnetic applied at 70° away from the crystalline c-axis. [Reproduced from Bolle *et al.*, 199, *Phys.Rev*.Lett.,**66,**112.)

3.2.3 Magneto-optical Kerr effect (MOKE)

The magneto-optical Kerr effect in magnetic materials arises as a consequence of the optical anisotropy of the materials under study. The source of this anisotropy is the magnetisation, M, within surface domains which can be influenced by external magnetic fields. The optical anisotropy alters the state of linearly polarised light which is reflected off the surface of the material. It is useful in the study of surface magnetism since it is highly sensitive to the magnetisation within one skin depth at the surface, typically 10-20nm in most metals [71]. MOKE has the ability to probe the magnetisation in very small regions of a material, such as nano-wires. The polarization change reveals the nature of the sample surface magnetization and its magnetic domain structure [72]. It is a non-invasive technique that utilizes the interaction between the magnetic field at the sample surface and the electro-magnetic field of the incident photon [73,74].

3.2.4 Magnetic force microscopy (MFM)

Magnetic Force Microscopy is form of scanning probe imaging with magnetic sensitivity. MFM uses a cantilever with a magnetic tip to measure the force between the tip and the sample. It was first demonstrated by Martin *et al*. [75] who imaged stray magnetic fields from a thin film recording head with 100nm resolution. MFM uses the same basic techniques as AFM with the exception that the cantilever tip is coated with a magnetic material and the magnetic force is measured. MFM images contain information about both the topography and the stray fields at the surface of the sample since both exert forces on the tip. The spatial resolution of MFM depends on the tip size and shape and its height above the surface of the sample. It typically has high spatial resolution in the range 25 – 50 nm. Low temperature imaging is not a standard capability but has recently become commercially available; MFM has relatively poor minimum detectable fields at around 10^{-3} T/$\sqrt{\text{Hz}}$ as shown in figure 3.1 though advances in electronic and optical design are reducing this.

3.2.5 Scanning superconducting quantum interference device microscopy (SSQUID)

Superconducting Quantum Interference Devices are magnetic sensors which consist of a superconducting ring containing two Josephson junctions. These measure the magnetic flux threading the loop which is a relatively non-invasive technique. In the most common scanning systems the spatial resolution falls in the range 1- 4 μm. The SSQUID is generally attached to a flexible cantilever and raster scanned in direct contact with the sample surface without any feedback mechanism. When the SQUID sensor is brought close to magnetic sample, the stray flux penetrates the SQUID loop. This is usually compensated by a field coil in a flux locked loop with the flux compensation current used to build an image [76,77]. This approach has the advantage of high sensitivity, but the disadvantages of relatively modest spatial resolution, and the requirement that the SQUID sensor be cooled. There is a broad range of reported minimum detectable fields for SQUIDS depending on the materials used, the size and the operation temperature etc. Scanning SQUID Microscopy techniques have been widely used to image vortex matter in superconductors at very low fields with typical minimum detectable fields down to $\sim$10 nT/$\sqrt{\text{Hz}}$ and spatial resolution around 1 μm, [77] (c.f., figure 3.1).

3.2.6 Scanning Hall Probe Microscopy (SHPM)

This section describes the operating principles of scanning Hall probe microscopy. SHPM is a magnetic imaging technique in which a sub-micrometer-sized Hall sensor locally probes the magnetic field at the surface of a sample. This approach is commonly used for studying various surface properties of materials, from the micrometer scale to the nanoscale. One common Hall probe is the GaAs/AlGaAs two – dimensional electron gas (2DEG) with very low charge carrier density and high mobility at low temperatures. Field detection relies on the Hall effect; when a current is passed through a conductor in a magnetic field a Hall voltage is induced perpendicular to the current direction (c.f., section 3.3.2.1). SHPM images are built from the change in Hall voltage when a nanoscale Hall probe is scanned over the "magnetic" sample surface. The Hall probe is usually mounted on the piezoelectric scanner tube of a variable temperature scanning tunnelling microscope with a stick-slip coarse approach mechanism. The Hall probe incorporates a secondary sensor (e.g., STM tip) which is used to control the distance between the Hall probe and the sample surface as it is raster scanned across the surface. In the probes used here the active Hall sensor is positioned close to the gold-coated corner of a deep mesa etch, which serves as primitive STM tip and allows simultaneous measurements of sample topography [78,79]. SHPM has excellent spatial resolution down to 50nm (FIB Bi Hall probes) with 2.5×10^{-6} T/$\sqrt{\text{Hz}}$ minimum detectable fields for Bismuth nano-Hall probes with dimensions $\sim 120 \times 120$ nm [80] (c.f., figure 3.1). Figure 3.3 shows a schematic diagram of a typical scanning Hall probe microscope [26].

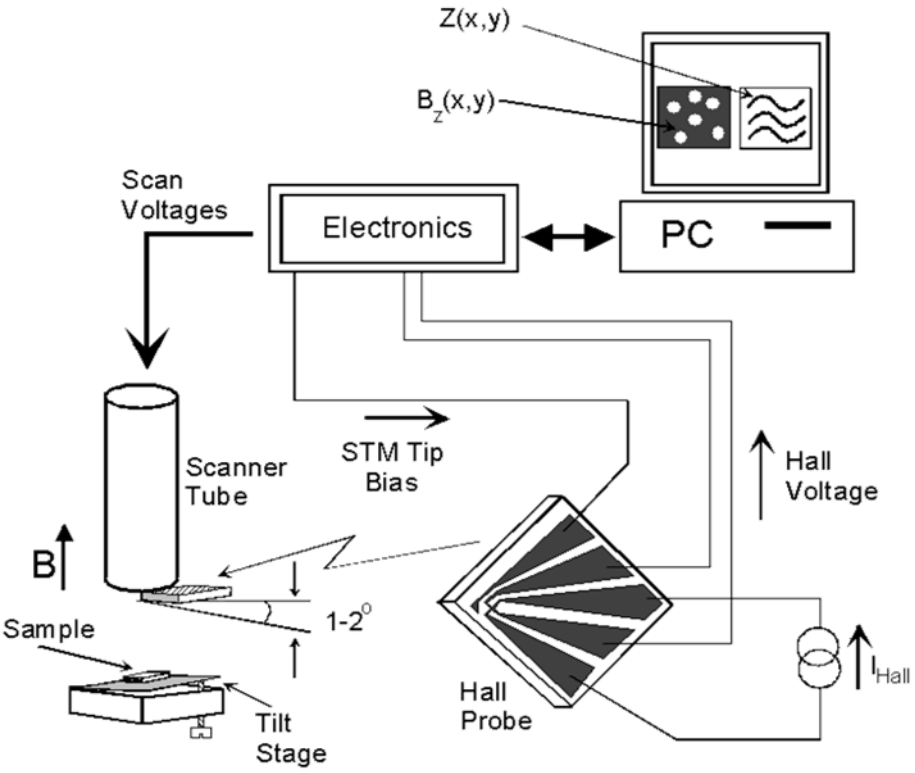

Figure 3.3: Schematic diagram of a Scanning Hall Probe Microscope. [Reproduced from Simon J. Bending, Adv. Phys. **48**, 449 (1999)].

3.3. A detailed description of SHPM:-

3.3.1 Introduction to the history of SHPM

Scanning Hall probe microscope is a member of the Scanned Probe Microscopies (SPMs). State-of-the-art-scanning Hall probe microscopy provides nanometer-scale mapping of the surface magnetic induction of the sample. In 1958, Kronick [81] designed and built the first SHPM, using a bismuth Hall sensor on a conical glass substrate. In these experiments, Hall sensor sizes were on the order of 100μm and the sensor-sample distance on the order of 50μm [82]. Since then the technique has become quite widespread in the science community and already commercialized. Today most state-of-the-art-systems employ GaAs/$Al_{0.3}Ga_{0.7}As$ heterostructure Hall probes which were first used by Geim (1989) [83] and Bending *et al*. (1990) [84,85]. A revolution in the field took place in 1992, when a GaAs/AlGaAs Hall probe chip with an integrated STM tip was first mounted onto a piezo tube scanner [86]. Using the STM tip together with the piezo scanner developed earlier for precise position control, the separation between the sub-micron sized Hall sensor and the sample could be reduced to a few nanometers [87]. Most SHPM setups nowadays still have the same design and the same set-up as used in this work [88,89].

3.3.2 Basic principles of scanning Hall probes

The Hall effect is used for detecting the local magnetic induction. It arise from the dynamics of carriers in electric and magnetic fields [90,91]**.** In SHPM, the properties of the Hall probe material determine the minimum detectable field, whereas the dimensions of the active area determine the spatial resolution. In this section, the basic principles of Hall sensors will be presented, including the Hall effect and the main characteristics of the Hall ‘magnetometer’.

3.3.2.1 The Hall effect

Hall probes are based on the principle of the Hall effect, discovered by Hall in 1879 [48]. It occurs when a current passes through a conductor in the presence of a perpendicular magnetic field. Physically, the magnetic field causes the charge carriers to deflect from their original path, in the description here the +y direction. While flowing through the conductor, the electrons are deflected towards one side of the conductor due to the Lorentz force ($\mathrm{F_L}$) arising from the magnetic field. When carriers build up on one side of the conductor it creates a charge imbalance with the other side becoming oppositely charged. This in turn generates an electric field and a steady state is established when the electric force ($\mathrm{F_E}$) due to this field balances the Lorentz force ($\mathrm{F_L}$), so that the net force is zero [48,79] .

In this situation the total force on the electron can be described by

$$\mathrm{F} = \mathrm{F_E} + \mathrm{F_L} = 0 \qquad (3.1)$$

$$\vec{\mathrm{F}} = \mathrm{q}\left(\overrightarrow{E_H} + \vec{\mathrm{v}} \times \vec{\mathrm{B}}\right) = 0 \qquad (3.2)$$

where q is the carrier charge, v is their drift velocity, $\overrightarrow{E_H}$ is the Hall electric field and $\vec{\mathrm{B}}$ is the magnetic induction. Hence

$$\mathrm{q}\overrightarrow{E_H} = -\,\mathrm{q}\vec{v} \times \vec{\mathrm{B}} \quad , \qquad (3.3)$$

and if $\overrightarrow{E_H}$, $\vec{v}$ and $\vec{\mathrm{B}}$ are mutually perpendicular

$$E_H = -\,v\mathrm{B} \qquad (3.4)$$

Figure 3.4 illustrates the Hall effect for a slab geometry with dimensions $l \times w \times d$ and figure 3.5 shows the simplest geometry for a Hall cross [92].

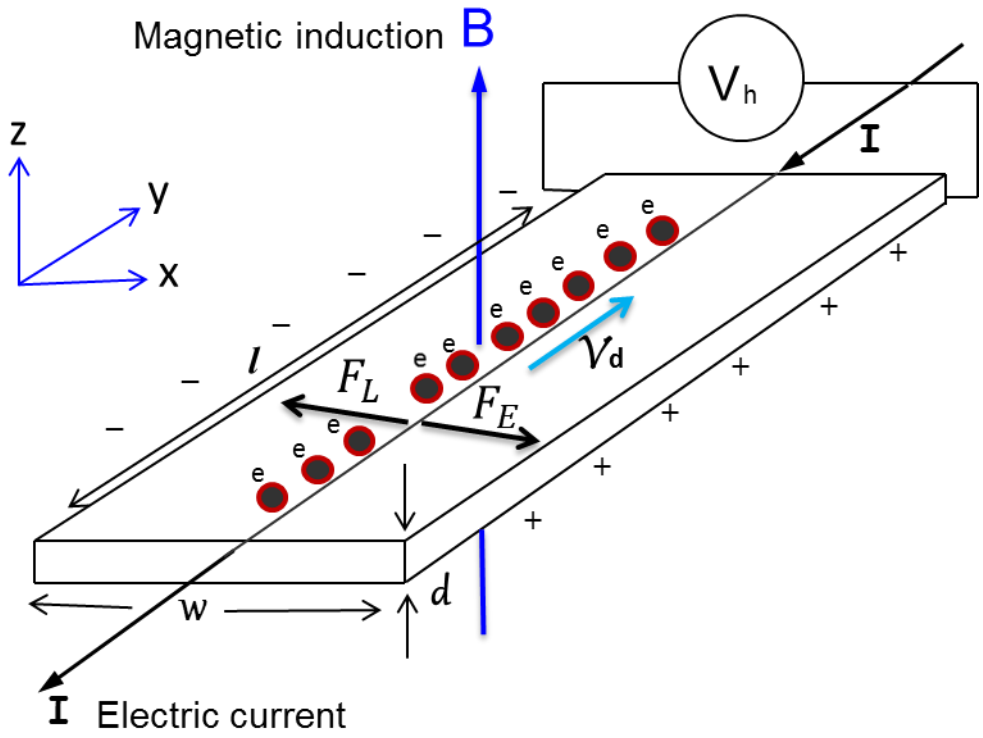

Figure 3.4: Sketch of the Hall effect for a slab geometry.

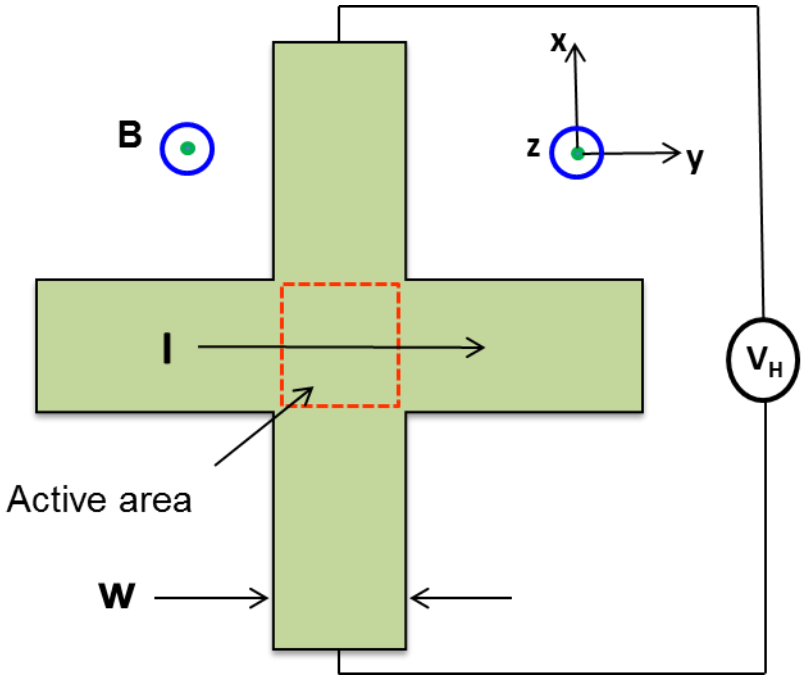

Figure 3.5: Schematic diagram of a simple Hall cross. The output of the Hall voltage, V_H, is proportional to the current, **I**, in the y- direction and the z component of the magnetic field, B_Z, within the active area.

It will be assumed here that, the carriers are electrons with a charge $-e$, all moving with the same drift velocity, v_d . Current flows in a cross-sectional area $w \times d$ along a conductor of length l.

Rearranging equation 3.4 we find

$$E_H = -\frac{IB}{dwnq} = \frac{V_H}{w} \quad (3.5)$$

$$\mathrm{V_H} = \frac{I\,B}{qn\,d} = \mathrm{R_H IB}, \quad (3.6)$$

where $\mathrm{R_H}$ is the Hall coefficient.

$\mathrm{R_H} = 1/n_{2D}e$, where $n_{2D} = n \times d$ for three-dimensional probes.

The Hall coefficient is inversely proportional to the carrier density,n, and if this is known, the Hall effect be used to infer the magnetic induction [93]. The Hall voltage is approximately proportional to the average magnetic induction across the active area when the Hall probe is placed above the sample. In this case, the minimum detectable field is dependent on many factors such as its material characteristics, the device geometry and the Hall current [94].

In this case, it is generally easy to calculate the Hall coefficient of a sensor by applying a known magnetic field when it is very far from a 'magnetic' sample.

For a high sensitivity Hall effect magnetic field sensor, materials with large Hall coefficient are required. Since q is constant, the only variable is the carrier density which should be minimised. A more important factor is the signal-to-noise ratio (SNR), which is defined as the ratio of the measured Hall voltage to the noise voltage [79]. Assuming the noise is solely characterised by the "white "Johnson noise voltage

$$\mathrm{SNR} = \frac{\mathrm{I_H\,R_H\,B}}{\sqrt{4\mathrm{R_J k_B T \Delta f}}} \quad . \quad (3.7)$$

Where $\mathrm{k_B}$ = Boltzmann constant (1.38×10^{-23} Joules/Kelvin),

T= Temperature in degrees Kelvin (K = +273 Celsius),

R_J= the device resistance in Ohms (Ω) and

Δf = the measurement bandwidth in Hz .

The minimum detectable magnetic field is defined as the magnetic induction, B_{min} , when the SNR=1 .

Hence, the minimum detectable field of the Hall probe sensor is defined by

$$B_{min}=\frac{\sqrt{4R_J k_B T \Delta f}}{I_H R_H} \quad (3.8)$$

There are typically three dominant noise sources, namely thermal or Johnson – Nyquist noise, flicker or 1/f noise and white noise. Johnson noise has a flat frequency spectrum and is hence a form of white noise [95]. The signal-to-noise ratio of our Hall sensors is limited by their frequency-dependent noise voltage, $V_n(f)$. At high frequencies, above the 1/f noise corner, this is governed by thermal Johnson noise, V_J [26]. At low frequencies the spectrum is dominated by 1/f noise that has a wide range of possible origins such as carrier fluctuations due to trapping/detrapping at defects or electron-hole generation-recombination processes. The amplitude of the 1/f noise and the location of the 1/f noise corner increase quite rapidly as the sensor current increases [96].

3.3.2.2 Key figures of merit for scanning Hall probes

In order to achieve high spatial resolution, SHPM sensors need to be fabricated with nanoscale dimensions and operated in very close proximity to the sample surface. Low minimum detectable fields require a large Hall coefficient (low carrier density) and low Johnson and 1/f noise. Low offset resistances are also a significant advantage in order to prevent the saturation of high gain low noise pre-amplifiers. These criteria are all well satisfied in GaAs/AlGaAs heterostructure two-dimensional electron gases (2DEGs) at low temperatures when they have very high carrier mobilities. Sensors with dimensions down to ~100 nm have been demonstrated and 2DEGs typically have low carrier concentration and are confined close to the surface of the chip [97]. However, the much lower carrier mobility at room temperature leads to much higher lead resistances and Johnson noise, and dramatically increases minimum detectable fields [98].

3.3.2.3 GaAs/AlGaAs 2DEG Sensors

Several different semiconductors or semi-metals can be used to fabricate Hall probes. However, in this work a GaAs/AlGaAs two dimensional electron gas was used for low temperature imaging as it has very high low temperature electron mobility, leading to very good signal-to-noise ratios, and can be patterned into Hall crosses with very small dimensions as required to resolve the stray magnetic fields of individual flux vortices. In order to obtain good Hall probe properties one needs a low electron density and high carrier mobility, as satisfied by the GaAs/AlGaAs two dimensional electron gas. The layers of two different lattice-matched semiconductors, GaAs and AlGaAs, are grown by Molecular Beam Epitaxy (MBE). Modulation doped semiconductors overcome the problems of high resistance and high Johnson noise at low temperature by physically separating electrons from ionised donors with an undpoed AlGaAs spacer layer. In this way ionised impurity scattering is dramatically reduced. (c.f., figure 3.6) [26].

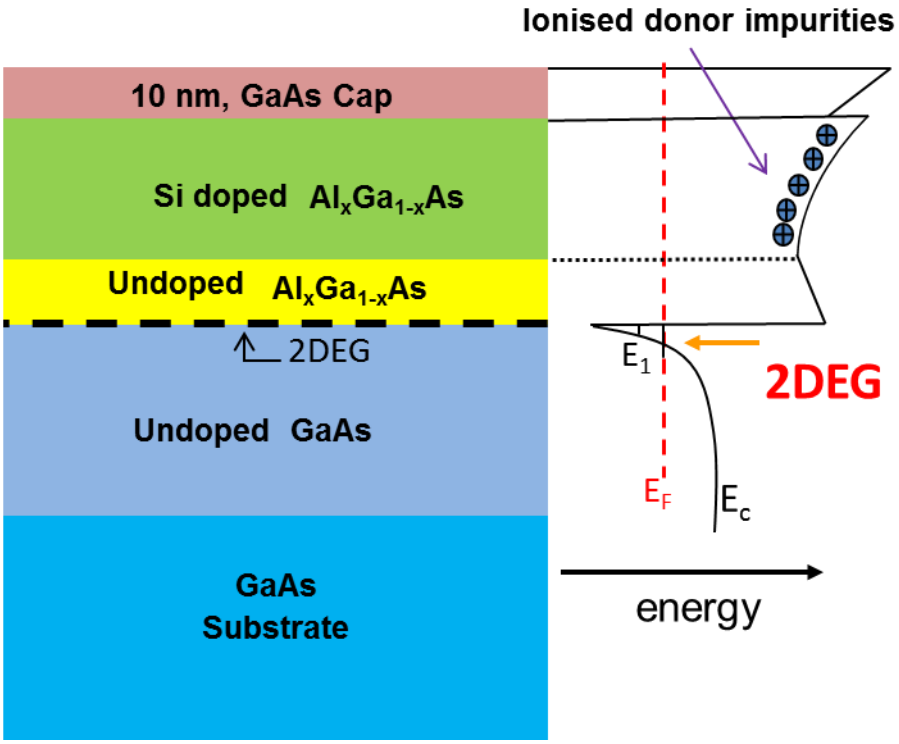

Figure 3.6: Layer structure of a modulation-doped GaAs/AlGaAs semiconductor heterostructure as well as a parallel sketch of the conduction band edge [Reproduced from Simon J Bending, Adv. Phys. **48**, 449 (1999)].

A Si-doped AlGaAs layer is incorporated below the GaAs cap of the heterostructure to provide electrons to the interfacial quantum well. At low temperatures electron scattering and mobility are dominated by scattering at impurities and defects in the lattice since phonon scattering is frozen out. An undoped AlGaAs spacer layer is placed between the main GaAs layer and the Si-doped AlGaAs layer to suppress scattering at ionised impurities. The 2DEG is formed by electrons from the Si-AlGaAs which become trapped in a V-shaped potential well at the interface between the undoped GaAs and the AlGaAs spacer, leaving behind positively ionised donors. Quantum mechanical bound states form at the V-shaped 2DEG potential and the lowest eigenstate generally fills up to the Fermi energy.

The characteristics of modulation doped heterostructures depend on the thickness, composition and doping levels of the individual layers. The two dimensional electron gas heterointerface quality is generally very high due to the almost perfect lattice match. The electron density is controlled by the spacer layer thickness and the doping concentration. Carriers are confined to a very narrow quantum well about 10 nm wide with a two dimension electron density of $n_{2d} \approx 10^{15}$ m^{-2}, and a Fermi wavelength of $\lambda_{F=} (2\pi/ n_{2d})^{1/2} \approx 80$ nm and a mobility of up to $\mu \approx 10^2$ m^2V^{-1} s^{-1} at low temperatures. The low 2D carrier concentration leads to a large Hall coefficient and a high field sensitivity. The spatial resolution of the Hall probe is governed by the physical size of the active area [99] and achieving active sizes $<$ 100 nm is greatly complicated by sidewall depletion.

3.3.3 Introduction to piezoelectric materials and scanner tubes

To enable the very small and precise movements necessary for SPM techniques, piezoelectric materials have been developed for use in scanners. Piezoelectric tube scanners are widely used in micro- and nanoscale positioning tasks. The piezoelectric effect relates the mechanical stress/strain and electric displacement /field when a voltage is applied between two electrodes of a piezoelectric material. The strain that is caused by the applied electric field depends on the dimensions of the material and the applied voltage. These properties of piezoelectric materials are used for both coarse motion (e.g. stick-slip coarse approach in the z direction) and fine x-y-z motion during scanning.

The piezo scanner tube is segmented and allows different voltage biases to be applied to four different quadrants, leading to various bending and elongation displacements. The motion is usually divided into two parts; the lateral raster scan in the XY plane and the topography tracking response in the Z direction. The resulting scanner range is typically between 1-100 μm in XY and 0.1-10 μm in the Z direction [100].

Piezoelectric component are also used to achieve a coarse approach in which the motion arises from a stick-slip motor driver by a sawtooth waveform generator. For safety each step of the motor should be smaller than the piezotube scanner range in the z direction; this prevents the sensor from crashing into the surface. On the bench the stick-slip motor can be driven quickly without feedback, but when the sample-sensor spacing is small an automatic approach is used, (c.f., figure 3.7(a)). The latter is performed very slowly leaving time to search for a tunnelling current between the sample and the Hall probe STM tip. Frequently the separation between probe and surface is kept constant during the scan process [101]. The maximum scan size that can be achieved with a particular piezoelectric scanner depends upon the length of the scanner tube, the diameter of the tube, its wall thickness, and the piezoelectric coefficients of the tube material. The latter is rather strongly temperature dependent. The microscope used here has scan areas of $\sim 55 \times 55\ \mu m^2$ at T= 300 K, $\sim 27 \times 27\ \mu m^2$ at T = 77 K and $\sim 11 \times 11\ \mu m^2$, at T = 4.5 K. The time taken to capture one image depends on the image size, scan speed and scan mode [49], (c.f., figure 3.7(b)), but is generally ~ 4 mins.

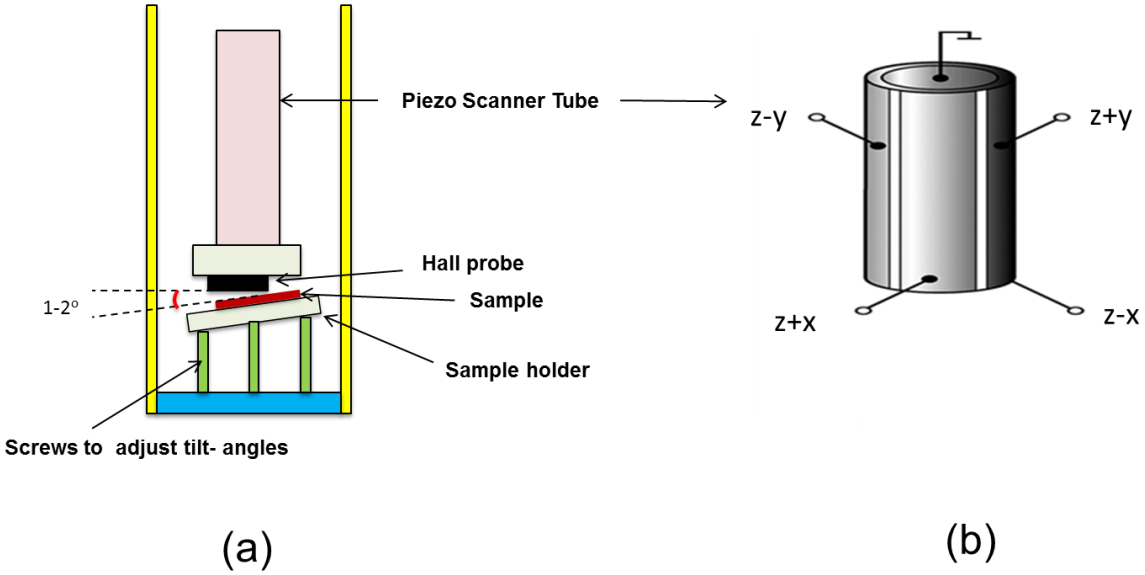

Figure 3.7: (a) A sketch of the SHPM after mounting the Hall probe and sample. (b) A schematic of the segmented piezoelectric scanner tube [Reproduced from M. Connolly, PhD thesis, University of Bath, 2008].

3.3.4 SHPM system design

The low temperature SHPM body is a structure housing all its mechanical and electrical parts including the scanner head, radiation baffles, flanges and a sample rod. The body of the microscope fits inside the cryostat with the sample at the centre of a solenoid to generate the magnetic field. The head of the scanner is composed of several parts, namely a sample puck, slider piezo, quartz tube, probe head and a scanner piezo, (c.f., Figure 3.8(a), (b)) which are used in conjunction to achieve coarse sample approach and fine scanning

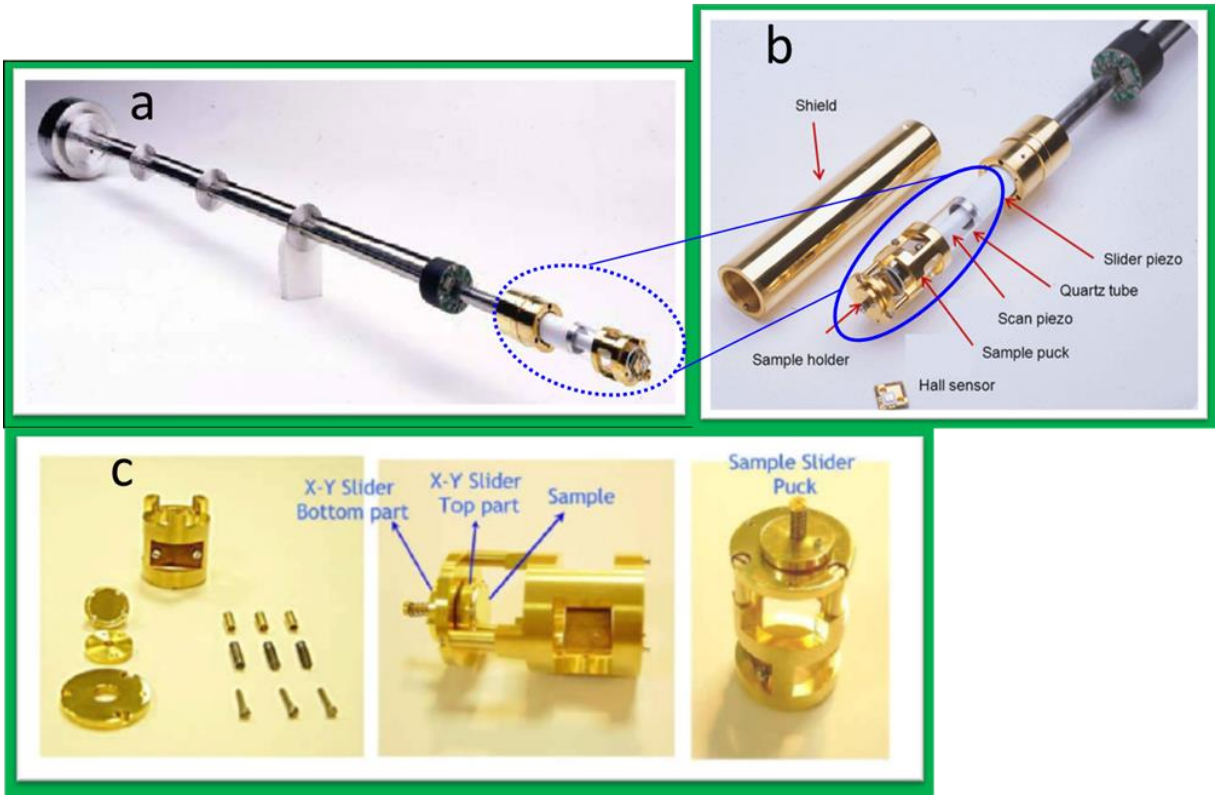

Figure 3.8: (a) Details of the LT-SHPM Nanomagnetic- Instruments Ltd head and sample rod. (b) Detailed view of the LT-head. (c) Details of the sample puck [Reproduced from L. T. S. H. P. Microscope, Oxford, UK, www. nanomagnetics-inst. com].

The Hall probe sensor is mounted onto a special chip carrier which sits opposite the sample and is screwed on top of a 5cm long piezoelectric scanner tube [102]. The sample is bonded to the sample plate using conducting silver paint in order to establish the sample voltage bias. The tilt angle between the Hall probe and the sample is set using spring tensioned alignment screws as shown in figure 3.8(c). This plays a key role in SHPM measurements since it sets the minimum Hall probe – sample separation. If the tilt angle is too large the STM tip will not come into contact with the sample. If it is too small one of the bond wires on the chip could touch the sample.

3.4. Operation of SHPM systems

The two main elements of the SHPM system are the microscope head and the SPM control electronics. Its operation is controlled by the SPM controller whereby a computer and SPM software are used as the interface for data input/output, as well as a limited amount of image processing. The electronic control unit has the ability to establish almost any kind of motion of the piezoelectric tubes. It consists of several electronic cards with different functions: The power supply, scan DAC, high voltage amplifier, slider, AD converter, Hall probe amplifier and tunnel current controller card. The power supply generates all voltages required by the system including the high voltages for the piezo scanner.

The Hall probe amplifier generates a regulated Hall current which is applied to the sensor and reads out the generated Hall voltage. The tunnel current controller card enforces tunnelling feedback and keeps the tunnel current constant by adjusting the sensor-sample separation. It also reads out the actual tunnelling current between the sample and tip, which can be viewed on an oscilloscope in real time.

3.4.1 Sample approach and SHPM imaging

The stick-slip coarse approach is started after the entire SHPM insert has been cooled down to a target temperature. During cooling the gap between the Hall sensor and sample is usually set at around 250 μm to prevent any damage occurring to the Hall probe due to thermal contraction. The automated approach routine is used to bring the sample and the Hall probe together until a tunnel current is detected at the tip at which point the z feedback loop is engaged. Once an approach has been successfully made the Hall probe is often retracted slightly out of tunnelling range and images scanned much more rapidly without z feedback control [103].

3.4.2 Magnetic and spatial resolution of SHPM systems

The spatial resolution is not only determined by the size of the Hall probe, w, but also the height, h, of the Hall probe above the sample surface. Both these parameters contribute to the absolute spatial resolution of the Hall probe which can be roughly approximated as $\sqrt{w^2 + h^2}$. In order to optimise spatial resolution, it is important to have a short active Hall bar and short distance to the sample [104]. The Hall probe height is determined by the height between the sample and the STM tip by the relation $h_{tot} = h + d \sin \alpha$ [105]. h is generally set at ~250 nm and the sample-probe angle α is usually around 1-2^0 degrees and d, the distance between the tunnelling tip and the active Hall probe, is usually about 5μm (c.f., figure 3.9). Hence h_{tot} is ~ 337 - 424 nm.

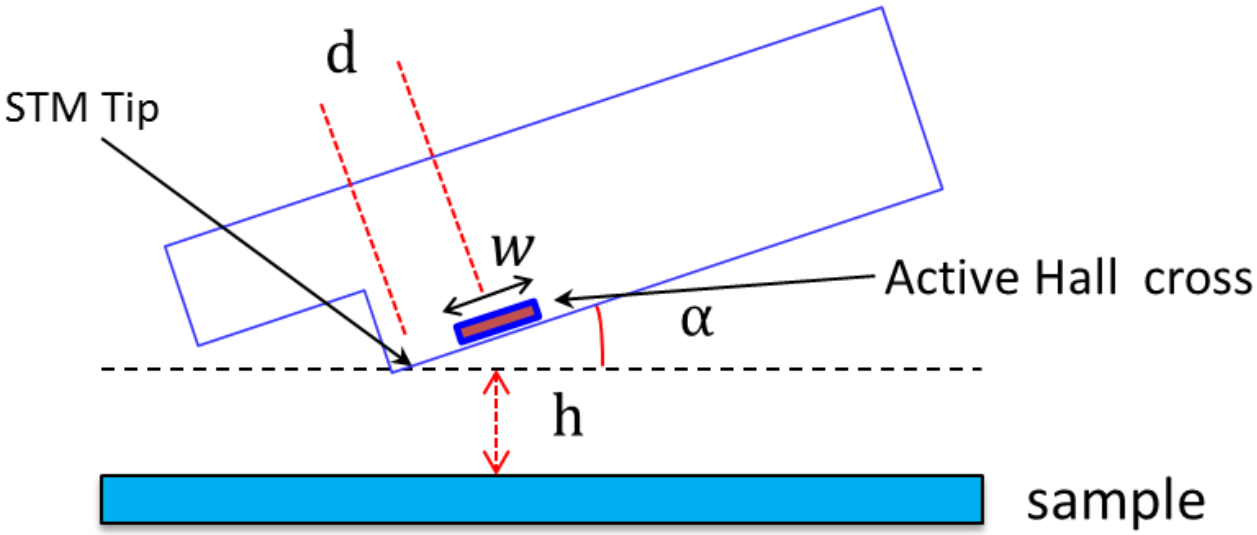

Figure 3.9: Sketch illustrating the parameters that determine the spatial resolution of the Hall sensor [Reproduced from S. Kweon, Study of a ferromagnetic semiconductor by the Scanning Hall Probe Microscope, (2008)].

3.5. Sensor/Sample mounting and scan modes

The Hall sensor is mounted on a custom made chip carrier using “Oxford Instruments” low temperature epoxy. An ultrasonic wire bonder was used to bond the Ohmic contact leads to the chip carrier with 25 µm diameter gold wire. Finally, the chip carrier was screwed onto the piezoelectric tube of the SHPM head (c.f., figure 3.10(b)). Electrical contacts are made to the Hall probe via spring loaded pins pushing onto the rear of the chip carrier.

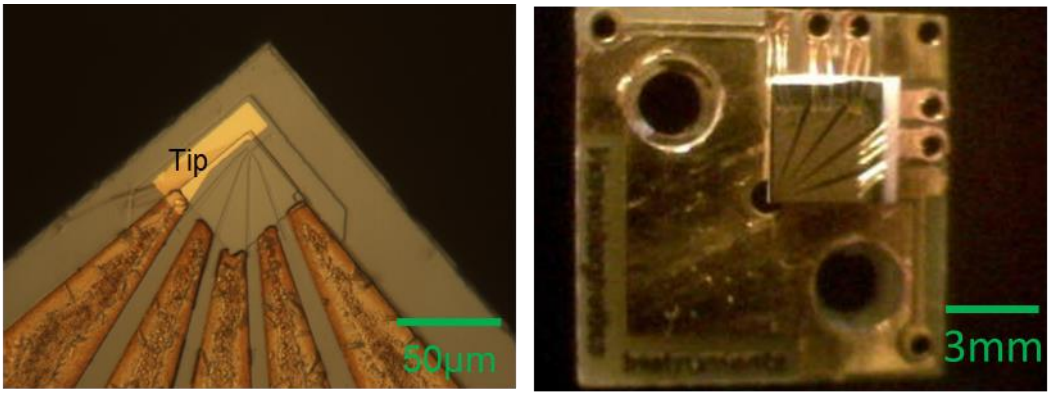

Figure 3.10: (a) Optical image of the active corner of the Hall-probe. (b) Diced Hall probe after packaging and wire bonding.

Before mounting the sample on a sampler holder, it is sometimes coated with a thin conductive film (e.g., Au) so that a tunnel current can be readily passed between the tip of the Hall probe and the conducting surface of the sample. The sample is glued onto the bronze sample puck with silver conductive paint and left to dry for one hour. The puck is then mounted on the SHPM head and the tilt angle adjusted using three screws on the slider. Finally, a safe gap of ~250 μm is set between the Hall probe and the sample prior to cooling and automatic approach.

The SHPM can operate in two modes: STM tracking and the flying modes. In the STM tracking mode the sample is approached until a tunnelling current is established between the tip on the Hall sensor chip and the sample. This is then maintained in a feedback loop as the sensor maps the surface magnetic field. This mode has the disadvantages that it is slow and there is a risk of crashing the Hall probe into the sample. In the flying mode, a tunnelling current is established during automated approach and the tip retracted a fraction of a micron out of tunnelling range. The Hall probe can then be scanned much more rapidly with a slightly lower spatial resolution with little risk of a head crash [26] (c.f., figure 3.11).

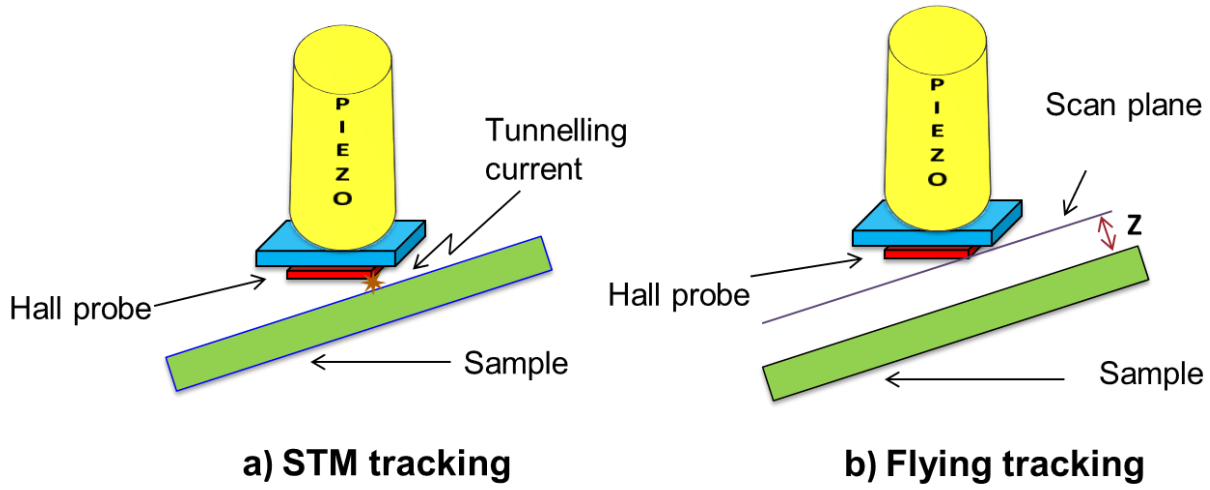

Figure 3.11: Diagram showing (a) the STM tracking and (b) the 'flying' modes of SHPM [Reproduced from Simon J. Bending, Advances in Physics **48**, 449 (1999)].

3.5.1. Cryogenic magnetic field and cooling systems

The variable temperature cryostat system houses the scanning Hall probe insert. It consists of an isolated sample space filled with Helium exchange gas, coupled to a cryogenic bath (N_2 or He) via a heat exchanger. A single super-insulated vacuum space provides thermal insulation [106]. In order to prevent the measurements being disturbed by vibrations coming from the building the cryostat was suspended on a single stage vibration isolation system on four pneumatic pads (c.f., figure 3.12).

The neck of the cryostat sits within the pole places of a rotatable electromagnet capable of providing in plane fields~∓ 700 Oe. A copper solenoid wound directly onto the cryostat neck provides out-of- plane fields ~∓ 20 Oe.

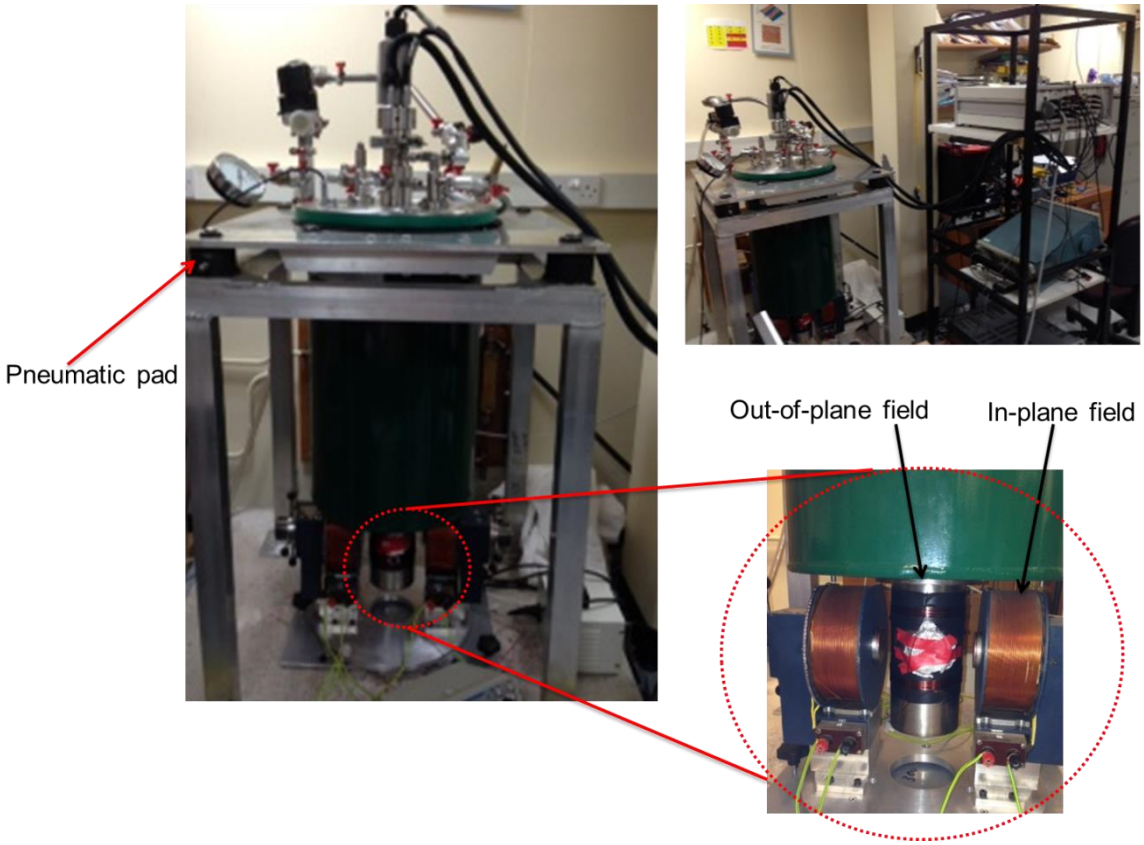

Figure 3.12: Images of the Cryogenics Ltd cryostat suspended from the anti-vibration mount. It has two separate sets of orthogonal coils which were used to generate an in-plane fields and a perpendicular “out-of-plane” field.

The procedure for cooling down the insert is as follows. With the system initially at room temperature the sample space is pumped with a turbo pump to remove the air inside, and then back-filled with high purity helium gas. This process is generally repeated several times to ensure that no air remains in the vicinity of the sample. A needle valve allows a controlled amount of liquid nitrogen or liquid Helium to flow through a heat exchanger and control the temperature of the sample space. Although the cryostat was designed for use with liquid Helium, the studies of Bi-2212 could be performed with much cheaper liquid nitrogen in the cryogen bath.

3.5.2 Advantages and limitations of current system

SHPM has several advantages over other magnetic imaging systems; the temperature and magnetic field can be easily varied. It exhibits good minimum detectable fields (7×10^{-6} T/$\sqrt{\text{Hz}}$ at 300K and 6×10^{-9} T/$\sqrt{\text{Hz}}$ at 4K) and is an almost completely non-invasive method of studying ferromagnetic and superconducting materials with high spatial resolution. In addition one gets quantitative information about one component of the magnetic field vector. Furthermore excellent magnetic resolution can be achieved in the presence of large applied magnetic fields in the wide operating temperature range 0.3K to 300K [107]. The self magnetic field due to the sensor is around $\sim$ 0.04G which is usually negligible. Furthermore it is possible to reduce scan times to $\sim$1 sec, making dynamic magnetic imaging possible. Reducing the size of the Hall probe active area yields higher spatial resolution but at the cost of worse minimum detectable fields [108]. The technique does have several disadvantages, namely limited field of view that is temperature dependent. Moreover many systems cannot operate below 4.2K because the cooling exchange gas condenses out, and one needs to re-approach the sensor each time the temperature is changed. Finally the limited spatial resolution means that vortex resolution is limited to quite low fields, typically < 30 Oe.

Chapter four

Experimental Methods:

Bi Hall probe Fabrication and Characterisation

4.1. Introduction of nanofabrication processes

This chapter focuses on sub-micron thin film Bi Hall effect sensors that have been fabricated by optical and electron-beam lithography using lift-off techniques on semi-insulating GaAs substrates. Their room temperature properties will be described in detail in this section. Bismuth was selected for the active Hall element of our room temperature devices because it has a low carrier density and relatively high carrier mobility. Two different Bi film thicknesses (50 nm and 70 nm) have been compared with the goal of optimising the sensor signal-to-noise ratio by exploiting the well-known dependence of the carrier density on thickness [109]. Their properties will be described in detail in chapter five. This chapter describes the fabrication sequence for Bi Hall probes using lift-off techniques as well as the apparatus used for characterisation.

The nanofabrication process involves many steps which are summarised in figure 4.1.

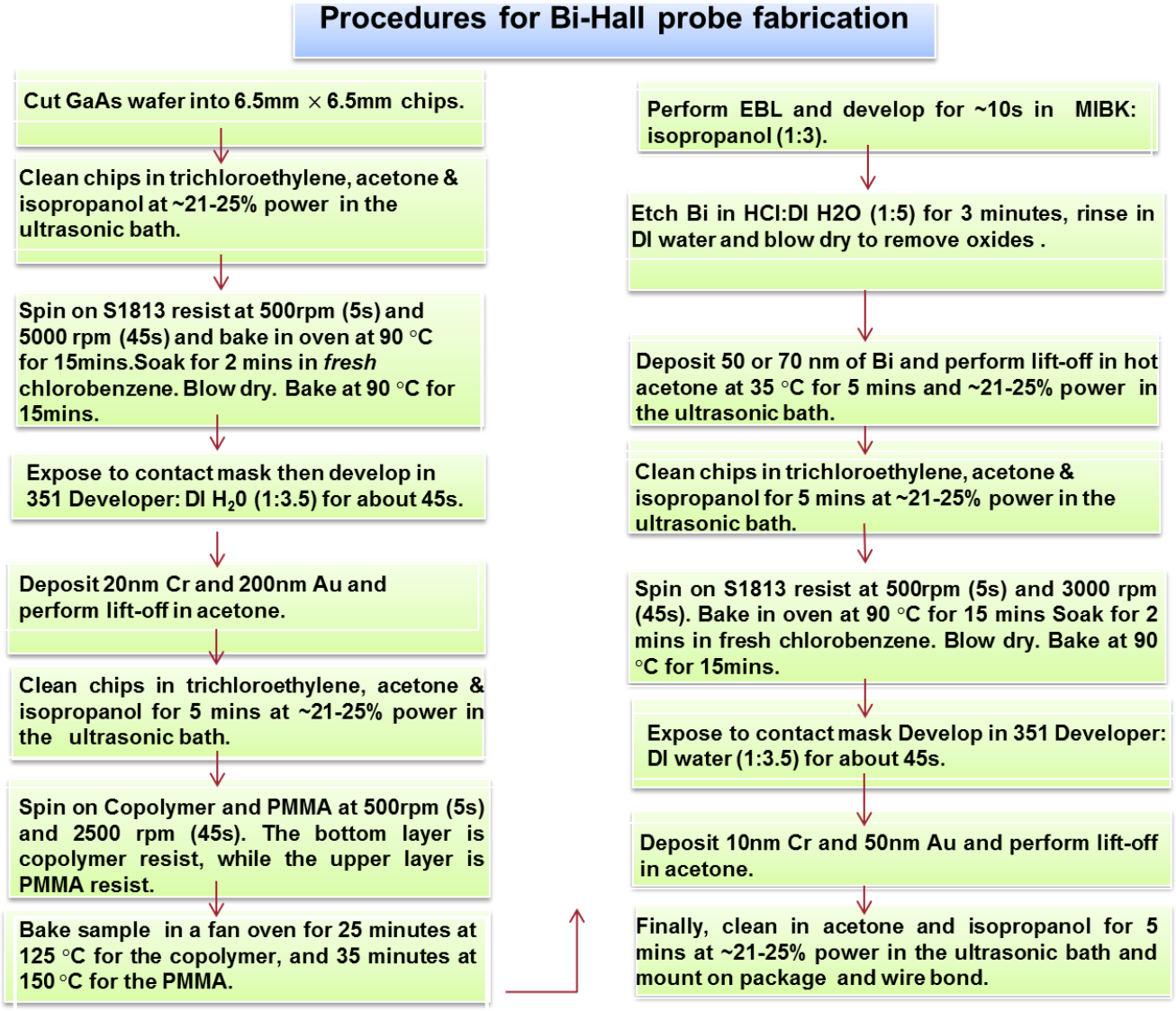

Figure 4.1: Schematic diagram of the Bi-Hall probe fabrication steps.

4.2. Substrate dicing and cleaning

This fabrication of Bi-Hall Probe sensors was performed in the University of Bath Nanofabrication facility. A semi-insulating GaAs wafer was scribed using a diamond scribe and cleaved into 6.5 mm x 6.5 mm square chips and four Hall sensors prepared on each chip, one in each quadrant. The size was chosen to match an existing optical mask set. The fabrication process is schematically shown in figure 4.2 and discussed in detail below:

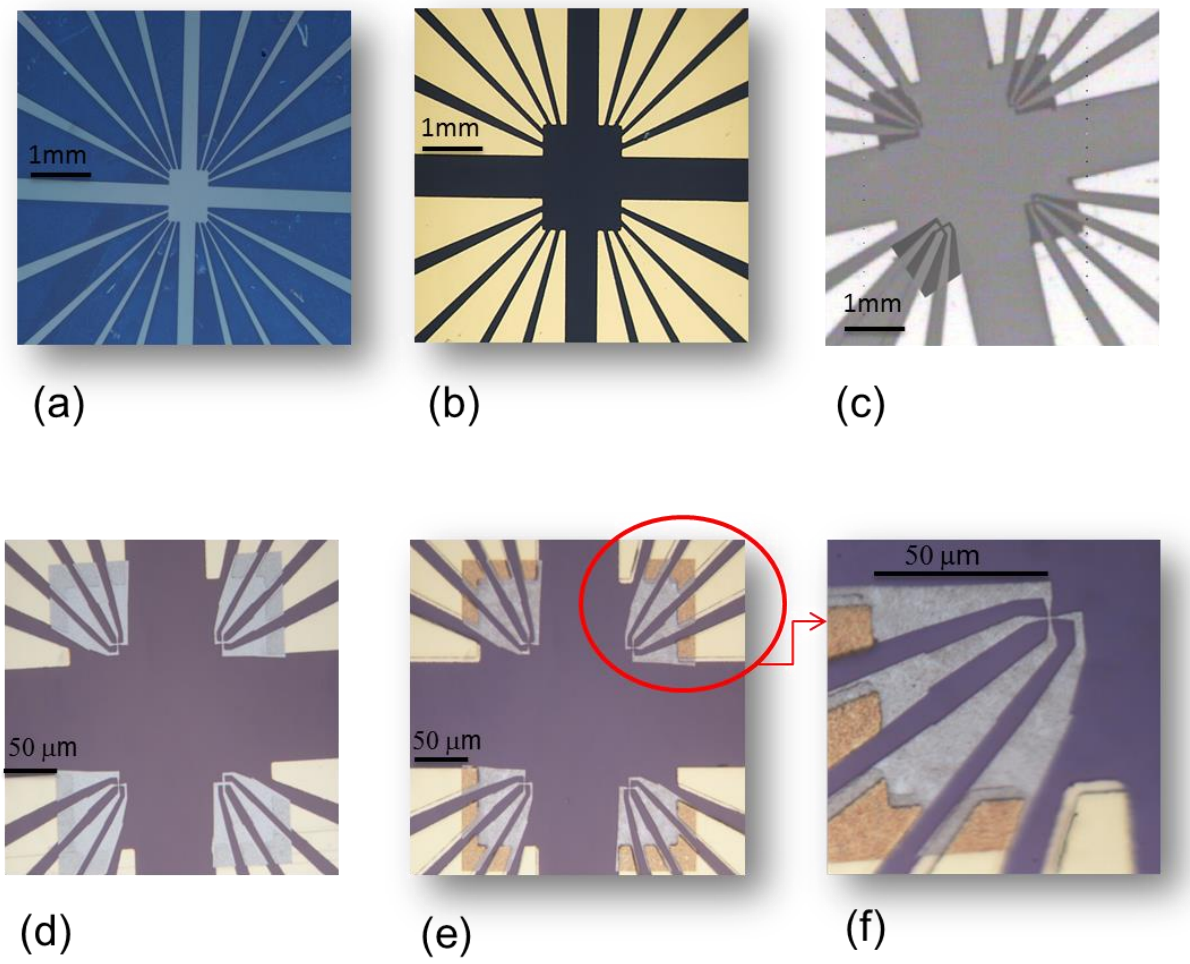

Figure 4.2: The stages of Bi-HP fabrication: (a) GaAs wafer is covered with S1813 photoresist and exposed to UV light. (b) First Ohmic contact metallisation after Cr/Au deposition. (c) After EBL Bi-HP design aligned to Ohmic contact pads. (d) Bismuth Hall probes with 4 different sizes. (e) Second Ohmic contact metallisation after Cr/Au deposition and (f) a magnified image of one Bi-HP on the sample with wire width=100 nm.

The chips were cleaned in an ultrasonic bath at ~ 25 % power for 15 minutes in solutions of trichloroethylene, acetone and isopropanol respectively. They were then dried using high pressure nitrogen gas. The clean chips were stuck on glass cover slips (rotated at a 45° angle to spread the resist to the corner of the chip during spinning) using photoresist (Shipley Microposit S1813) and baked at 90 ^{0}C for 30 minutes. This makes it easier to manipulate chips without scratching them with tweezers. The Shipley 1813 photoresist was dropped onto the GaAs chip which was then spun at 500 rpm for 5 seconds and 5000 rpm for 45 seconds to spread the resist into a thin film, and then baked in a fan oven at 90 ^{0}C for 15 minutes. After the first baking step, the samples were soaked in fresh chlorobenzene for 2 minutes so as to harden the top layer of resist by removing solvent from it. This leads to the formation of an overhang profile when developed. Chips were then returned to the oven and backed for a further 15 minutes at 90^{0}C before using a mask aligner to pattern the Ohmic contacts.

4.3. Device design

Photolithography is the basis for nearly all microfabrication technology as the means of transferring patterns to a substrate. Optical lithography is basically a photographic process that uses a light sensitive polymer, called a photoresist, and an ultraviolet (UV) light source projected through a chrome mask containing the desired pattern onto the sample surface coated with the polymer. The photoresist is spun onto the substrate with a controlled thickness using a spinner. Different spin speeds result in different resist thicknesses. After spinning using a specific recipe, the sample is prebaked to remove solvents and exposure is then carried out. There are three common types of mask aligner, contact, proximity and projection [110]. A contact mask aligner was used here whereby a direct contact between the optical mask and the sample occurs causing the effects of diffraction at the periphery of the mask features to be minimised. The sample is then exposed to UV light through the mask for a specific time that depends on the age of the UV bulb. The resist is then developed and rinsed in water. The lift-off technique can be used to realise multi-level metal structures using any materials that can be evaporated. In this way Cr/Au was deposited using thermal evaporation and removal of the unwanted deposited gold by a lift-off process. The deposition techniques as well as the lift-off process will be discussed in detail in sections (4.4) and (4.5).

ELPHY Plus software was used to produce designs for the Bi-Hall Probes with minimum dimensions of 0.1, 0.2, 0.3, 0.4, 0.6, 0.8, 1, 1.5 and 2 μm. These were then written by electron beam lithography (EBL) and this process will be discussed in detail in section (4.5).

4.4. UV lithography, evaporation and lift-off of Cr/Au contact leads

The purpose of Ohmic contact formation is to realise low resistance electrical connections to the device which are necessary for allowing current to flow into it. The first Ohmic contacts for Bi Hall probe sensors require two different layers to be evaporated: 20nm of chromium and 200 nm of gold. The chromium was used to improve the adhesion of the gold. To define the Ohmic contact metallisation, the photoresist was exposed to UV light through the appropriate chrome contact lithography mask.

To pattern Ohmic contacts, the resist is exposed for about ~12-22 seconds (depending upon the age of the UV lamp in the mask aligner) through a chrome-on-glass photolithographic mask using a Karl Suss MJB3 mask aligner. This mask is brought into close contact with the coated substrate and illuminated with UV light, which passes through the transparent areas and breaks bonds in the resist [111]. The exposed samples are developed using Microposit 351 developer mixed in the ratio 3.5:1 DI H_2O:developer for 30-50 seconds depending on the exposure time. In addition, the chips are rinsed in DI water for a period of around 10-15 seconds, to terminate the development process and dried using a Nitrogen gun. (cf. figure 4.2(a))

The metal deposition sources (Cr /Au) and tungsten evaporation boats are cleaned with a very high ultrasonic power (>75%) in each of the 3 solvents. Ohmic contacts were then deposition by thermal evaporation in a vacuum better than 3×10^{-6} mbar at a rate in the range 0.25 – 0.5 nm/s. The coated chips are placed into acetone and left overnight to remove the unwanted metal regions by lift-off, leaving the contact pads intact as shown in figure 4.2(b). These layers make an Ohmic contact to the Bi Hall probes and enable wire bonding using an ultrasonic bonder that will be discussed in detail in section (4.5). The entire process is sketched in figure 4.3.

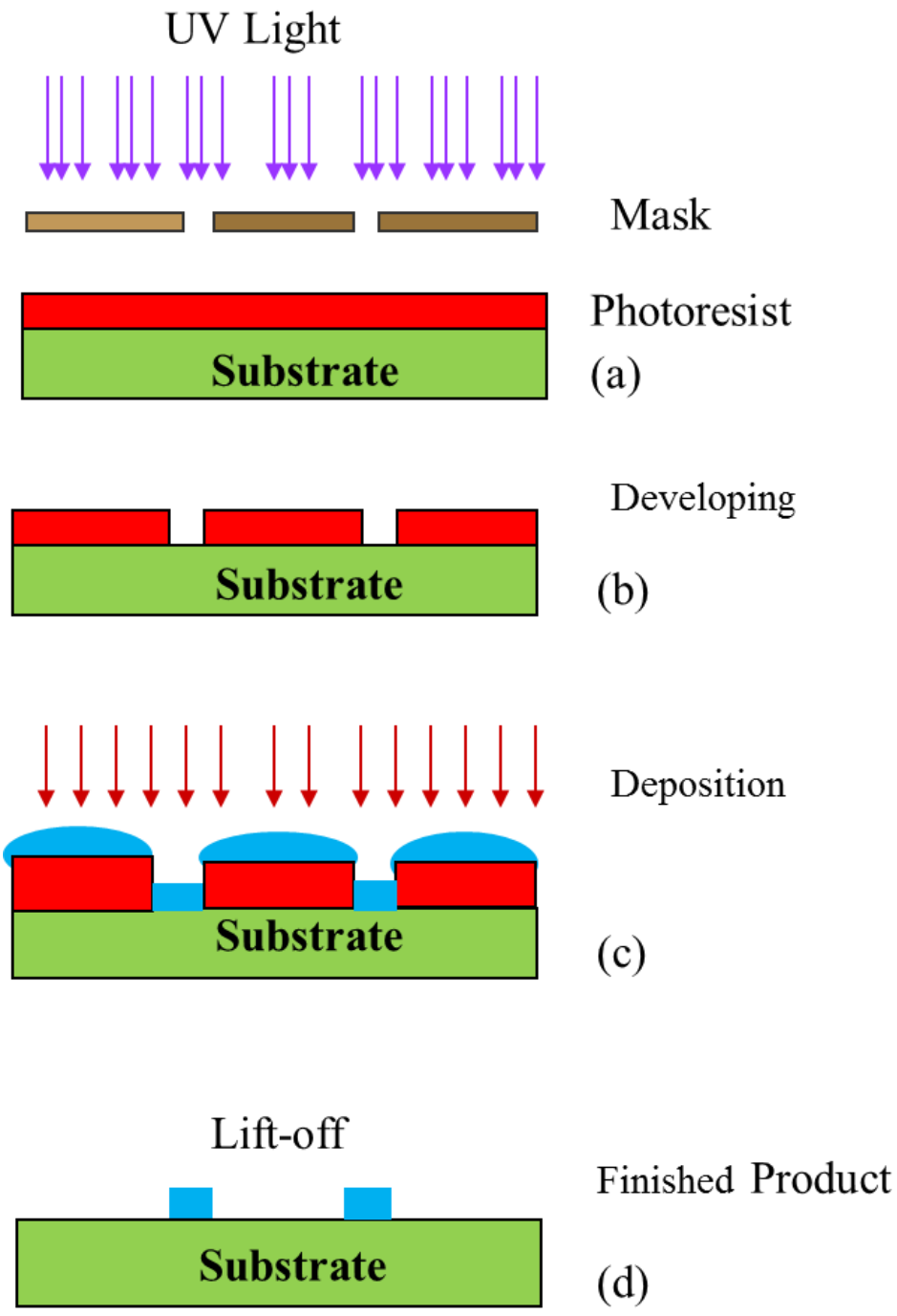

Figure 4.3: Key steps in Bi-Hall probe fabrication (a) UV exposure through a mask; (b) resist profile after development, (c) deposition of Cr/Au by thermal evaporation and (d) finished wafer after lift-off.

4.5. EBL lithography, evaporation and lift-off of Bi Hall bars

Electron Beam Lithography (EBL) is a specialized technique for creating the extremely fine patterns required in modern nanoscale electric devices. It is a direct, maskless method that exploits the very short wavelength of the electrons in an SEM. In contrast the resolution of optical lithography is limited by the wavelength of the UV light used for exposure. The electron beam has a wavelength that is so small that diffraction no longer defines the lithographic resolution giving it the ability to define much smaller structures. Electron beam resists are especially developed to respond to electron beam doses and the electron beam dose used at this stage was $300\ \mu C/cm^2$ [112]. There are two main groups of photoresists: positive and negative depending on whether electron exposure breaks or makes polymer chains. Poly methyl methacrylate (PMMA) is a positive resist that is frequently used in fabrication processes because it has high resolution with low sensitivity [113].

ELPHY Plus software was used to create the EBL designs for Bi-Hall probes. In the electron beam system, an acceleration voltage is applied to the electron gun to accelerate the electron beam to a specified kinetic energy, $\sim 30\ keV$. In this case sub-micron Hall sensors based on crosses defined by the intersection of two nanoscale wires, were then patterned in the PMMA by electron beam lithography, using the corners of the Cr/Au Ohmic contacts as alignment marks. To develop the pattern, a standard developer was used composed of a mixture of methyl isobutyl ketone (MIBK) and isopropanol (IPA) with a volume ratio of 1: 3 respectively and a development time about 10 seconds. Finally, samples were rinsed in IPA to terminate the development process [114] as shown in figure 4.2(c).

Lumps of 99.999% purity Bi were etched in concentrated HCl:H_2O (1:5) for a few minutes to strip surface oxides, and loaded into a Tungsten boat in a thermal evaporator. After pumping down, the samples were cleaned for 5 minutes in an Ar plasma and coated with 50 nm or 70nm of Bi at a deposition rate of 0.25 – 0.5 nm/s, monitored with a quartz crystal thickness monitor. Bi Hall bars based on wire widths in the range 0.1 - 2 μm were then realised by lift-off in hot acetone in an ultrasonic bath under ~25% ultrasonic power (c.f., figure 4.2(d)). Figure 4.4 shows both the undercut resist profile used and the metal lift-off process. Contact resistances measured at this stage of fabrication were found to be unacceptably high (>750kΩ).

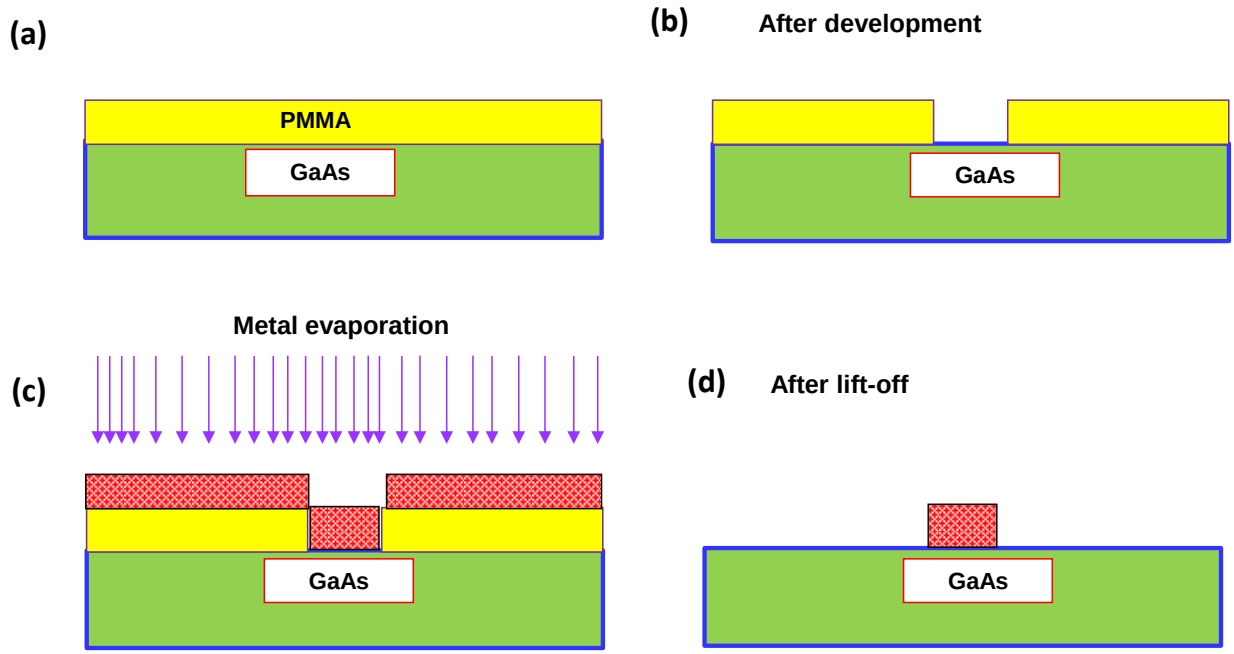

Figure 4.4**:** Sketch of patterning, deposition and lift-off processes for Bi-Hall probe fabrication using single layer PMMA EBL resist.

To rectify this a second Cr(10nm)/Au(50nm) metallisation was evaporated on top of the Bi leads. After this the contact resistances were found to be very low (<10Ω). In addition, the requirement for this metallisation is that it form a conducting bridge between the first Cr/Au layer and the Bi Hall probe and improves electrical contact between the Bi probe and the original Cr/Au leads. Typically, two terminal resistances of completed sensors lie in the range 1-4 kΩ at room temperature. Scanning electron microscope (SEM) images of a 0.1µm wire width sensor fabricated in a 50 nm thick Bi film are shown in figure 4.5.

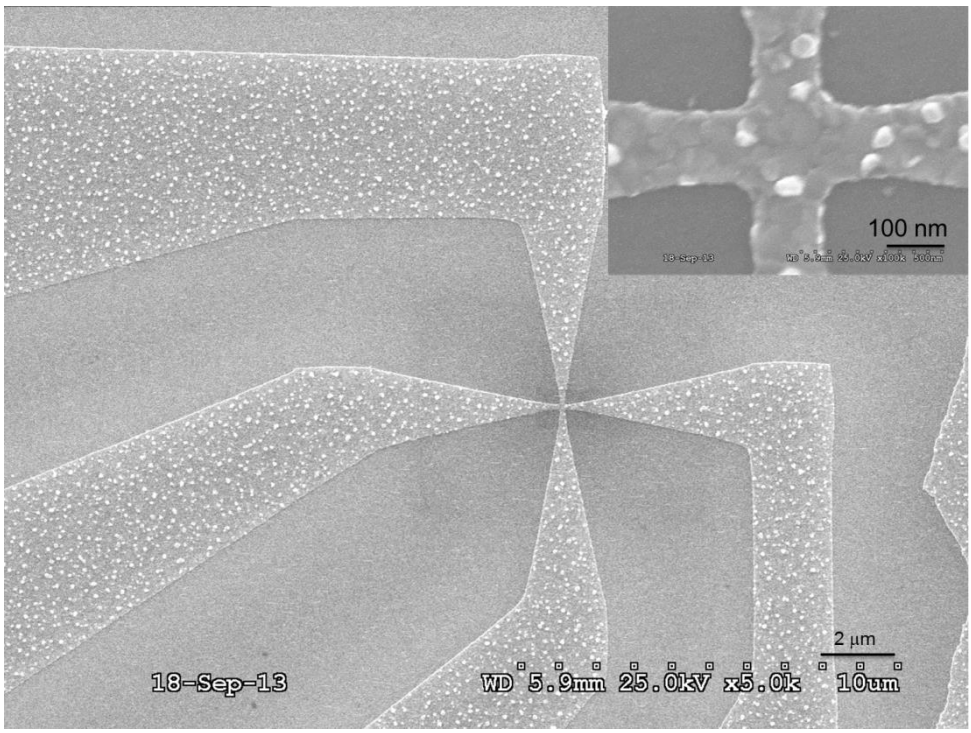

Figure 4.5: SEM images at two different magnifications of a 50 nm thick Bi Hall probe based on the intersection of two 0.1μm width wires.

4.6. Packaging & wire bonding

10 mm × 10 mm × 0.5 mm alumina substrates were cleaned in solvents and coated with photoresist at a spin speed of 3500 rpm and then patterned in the way described earlier for Cr/Au contacts. Thermal evaporation was used to deposit 20 nm Cr and 200 nm Au (c.f., figure 4.6(a)).

The completed Bi-Hall probe chips were glued with epoxy onto these alumina packages and wire bonded with 25 μm diameter Au wire. Long Cu wires were then Indium soldered to the pads on the package, for connection to terminals on the sample holder (c.f., figures 4.6 (b) and (c)).

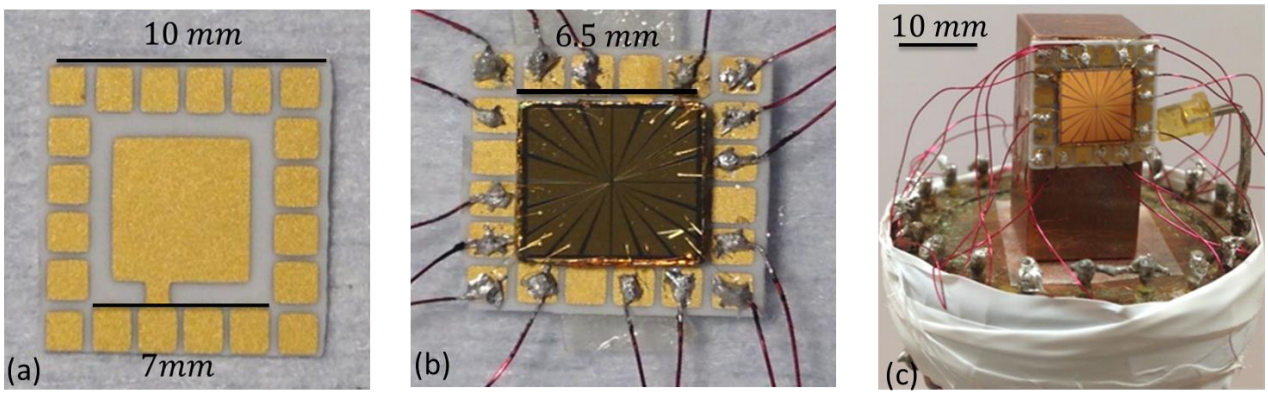

Figure 4.6: (a) Alumina package with Au contacts. (b) Sample mounted on substrate after wire bonding and soldering of Cu connection wires. (c) Head of sampler holder with connected Bi-Hall probe.

4.7. Sample holder and cryostat

The sample was mounted on the head of a home-made sample holder. This was inserted into a variable temperature cryostat that had 16 terminals on the sample plate connected by twisted pairs of Cu wires to BNC connectors in a connection box on top as shown in figure 4.7. The sample rod was inserted into the static sample space of the cryostat, evacuated and back-filled with Helium gas to prevent oxidation or other degradation of the Bi probes during characterisation. The tail of the cryostat, containing the sample, sits in the middle of a commercial electromagnet capable of generating a maximum field of ~100 mT perpendicular to the plane of the sample. The electromagnet was driven by a bipolar power supply, allowing the magnetic field at the Hall sensor to be smoothly varied and reversed.

Figure 4.7: (a) Connection box on top of the sample holder. (b) Zoomed out view of the sample mounted on the end of the sample holder.

4.8. Measurement set-up for the Hall effect and noise spectra

The Hall effect measurements were carried out on a range of Bi-Hall probes with different dimensions at room temperature. The Hall probe sizes ranged from 0.1 - 2 µm with two different Bi film thicknesses, 50 nm and 70 nm, with the goal of optimising performance.

In order to characterise the Hall coefficient, sensors were driven with a 1-10 µA 32Hz ac current from a commercial function generator in series with a 1MΩ resistor. The two terminal resistances, Hall voltage and offset voltage were measured with a Stanford Research Systems SR830 digital lock-in amplifier. As shown in figures 4.8 and 4.9.

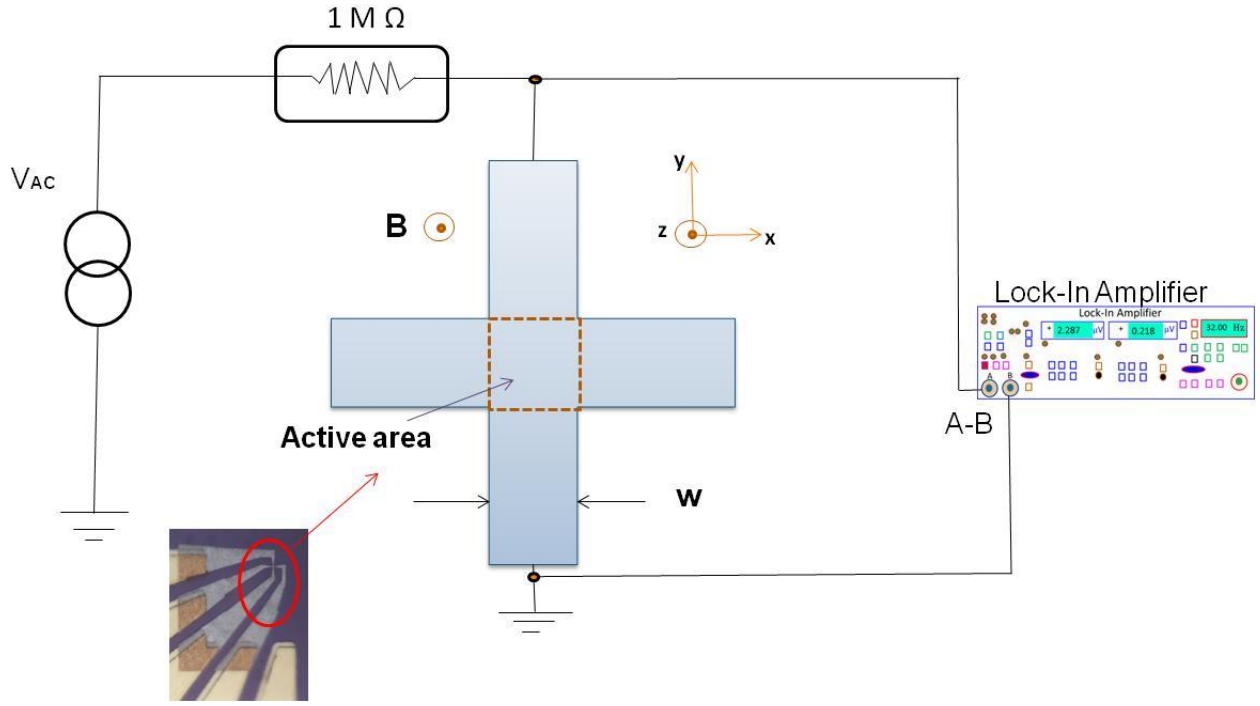

Figure 4.8: Schematic of the two-point room temperature measurement circuit used to characterise two terminal resistances.

The sensor noise was characterised using a home-made battery-driven dc current source and ultra-low noise preamplifier with 10^4 gain.

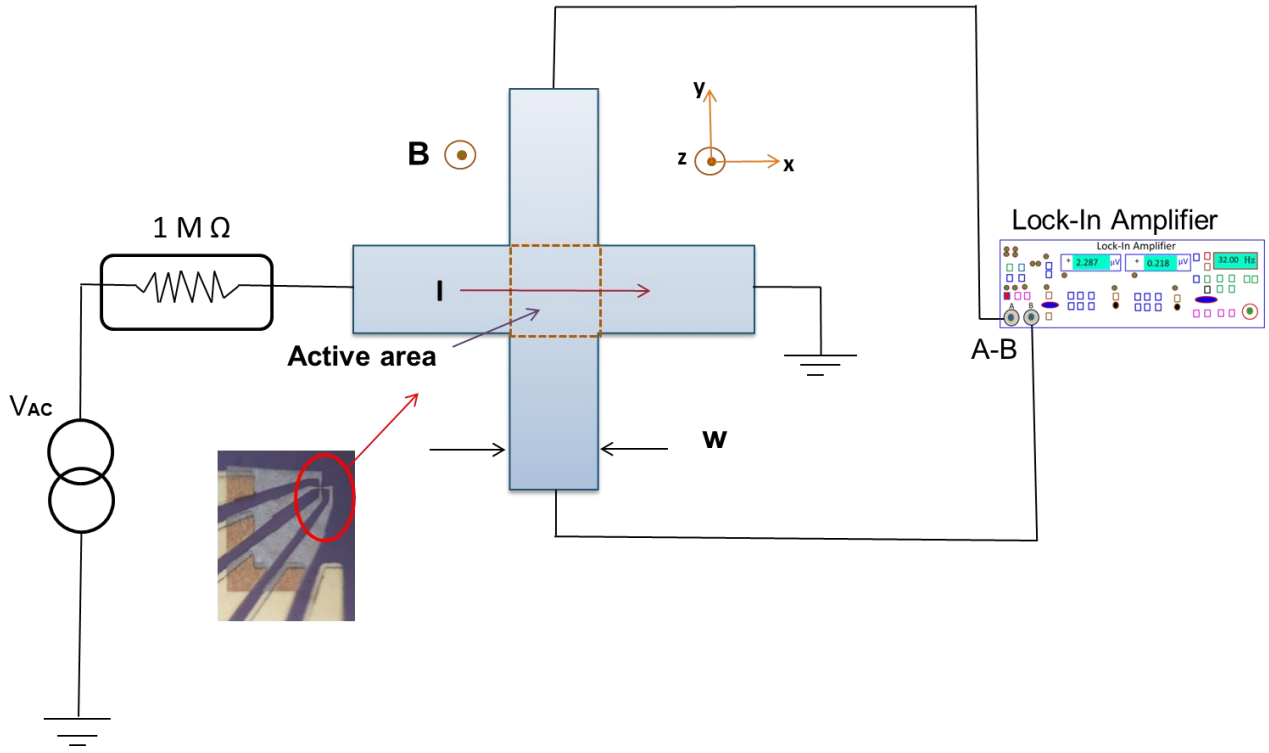

Figure 4.9: Schematic of the four-point room temperature measurement circuit used to measure the Hall and offset voltages.

Noise spectra were then measured in the range 0-100Hz at fixed Hall currents with a Hewlett-Packard HP3561A dynamic signal analyzer. One hundred individual noise spectra were automatically averaged in the DSA to build the final datasets. This is shown in figure 4.10.

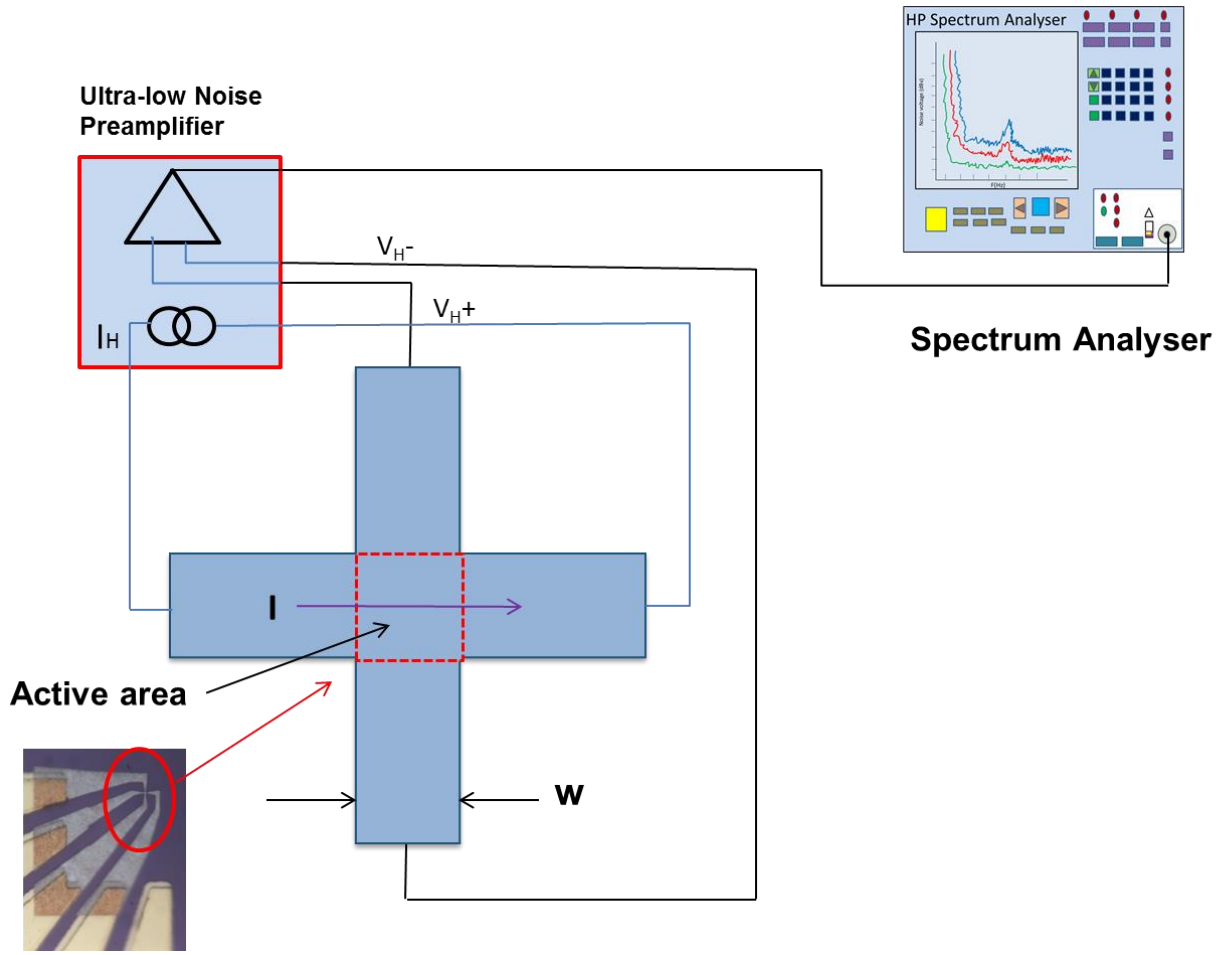

Figure 4.10: Sketch of noise measurement apparatus.

Chapter five

Characterisation of Nanoscale Bi Hall probes

5.1. Motivation for the work

Over the past two decades, research into understanding the magnetic properties of materials has advanced enormously. One of the major factors driving such research in magnetic imaging is the multi-billion dollar magnetic recording industry [115]. Recently, various kinds of thin films and magnetic materials have been investigated by a range of magnetic imaging techniques [26]. In order to get a better understanding of magnetic materials, considerable effort is being devoted to improve the resolution and ease of use of a variety of complementary techniques [116].

The ability to understand, predict and control the properties of matter in reduced dimensions is crucial for the design and development of future technologies. The challenge is therefore to find and exploit novel phenomena. In SHPM, the properties of the Hall probe material determine the magnet field resolution and the size of the active area determines the spatial resolution. This chapter describes the development of techniques for high resolution *room temperature* scanning Hall probe microscopy of ferromagnetic media.

The highly anisotropic Fermi surface of Bismuth has played a prominent role in the discovery of quantum effects in the solid state [117]. Due to its very low carrier concentration and large Hall response, it has been a natural choice for sub-micron Hall effect sensors [116]. While its performance at low temperatures is far inferior to other materials (e.g., GaAs/AlGaAs), it has been shown to be competitive at room temperature where high device resistances and high noise levels tend to be a problem. The goal of this project is to investigate the use of electron beam lithography and lift-off to fabricate scanning sub-micron Bi Hall sensors. Bi sensors have been systematically studied as a function of Bi film thickness and active dimensions in the range 100nm – 2μm, and here we report on the key figures of merit for our devices. Two different Bi film thicknesses (50 nm and 70 nm) have been compared with the goal of optimising the sensor signal-to-noise ratio by exploiting the well-known dependence of the carrier density on thickness [109].

The main motivation for this part of the thesis has been to develop and improve the performance of nanoscale Bi sensors using lift-off techniques. Previous work on Bi Hall sensors has utilised focussed ion beam (FIB) milling to fabricate such devices. However, the performance of these is generally compromised due to Ga^+ ion damage during patterning.

5.2. Introduction - prior state-of-the-art

Magnetic Force Microscopy (MFM) [75,118] is the technique of choice in the data storage industry for characterising magnetisation states in ferromagnetic media on the nanoscale. It is a scanning probe technique that measures the force between the sample and an oscillating, magnetically-coated tip. There are two main disadvantages with MFM: The sharp magnetic tip is invasive and imaging results are qualitative rather than quantitative in most cases. As a consequence, there is a need for a quantitative and non-invasive imaging technique to complement MFM. One promising candidate technique is scanning Hall probe microscopy (SHPM). SHPM is a non-invasive scanning probe imaging technique whereby a nanoscale Hall effect sensor is used to map the local magnetic induction close to the surface of a magnetic sample. This provides quantitative data on at least one component of the magnetic induction vector. It is a relatively new technique that can operate effectively at room temperature, since it is generally undesirable to cool ferromagnetic samples cryogenically for characterisation [26]. It has been widely used for investigating flux structures in superconductors at low temperatures, however has not been extensively used at 300K, due to the typically poor minimum detectable fields at room temperature. As a result, current developments in SHPM are focused on designing and fabricating novel nanoscale Hall sensors with lower noise figures for use at 300K.

High spatial resolution requires SHPM sensors to be fabricated with nanoscale dimensions and operated in close proximity to the sample surface. However, high magnetic field resolution needs a large Hall coefficient (low carrier density), and low Johnson and 1/f noise. In addition low offset resistances are highly desirable, preventing saturation in high gain, low noise preamplifiers. These criteria are all well satisfied in GaAs/AlGaAs heterostructure two-dimensional electron gases (2DEGs)

at low temperatures, when they have very high carrier mobilities. Sensors with dimensions down to ~100nm have been demonstrated and 2DEGs typically have low carrier concentration and are confined close to the surface of the chip [97]. Nevertheless, at room temperature the much lower carrier mobility leads to much higher lead resistances and Johnson noise, and dramatically increased minimum detectable fields [98]. In addition, low frequency 1/f noise increases rapidly at low Hall currents, further degrading minimum detectable fields. Many III-V semiconductor materials have been investigated with a view to achieving superior 300K performance, including InSb thin films [119,120], InAs/GaSb [121-123] and InGaAs/AlGaAs [124] quantum wells. Although slightly improved figures of merit have been demonstrated at room temperature in these alternative semiconductor systems, they all have associated limitations.

In practice, at room temperature semimetal Bi Hall sensors prove to be superior to low carrier density semiconductor systems, due to their higher Hall probe currents and lower lead resistances which outweigh the disadvantage of a considerably lower Hall coefficient. Thin Bi films have the disadvantage that the carrier concentration depends quite strongly on a number of factors, e.g., substrate material, deposition technique and film thickness. Scanning Bi Hall probe sensors have been widely investigated [81,125] and nanoscale devices with active sizes down to ~50nm have been realised by focussed ion beam (FIB) milling of larger thin film structures [126-128]. Nevertheless, it was found that devices smaller than 50nm were not operational, presumably due to damage and Ga^+ ion incorporation during FIB milling [127]. These effects lead to increased device resistances and noise levels, and suggest that alternative fabrication methods could lead to improved figures of merit. Lift-off techniques have recently been used to fabricate low noise static nanoscale Bi Hall sensors for monitoring domain wall motion [129]. This work was extended here to investigate the use of electron beam lithography and lift-off to fabricate scanning sub-micron Bi Hall sensors. Sensors have been systematically studied as a function of Bi film thickness and active dimensions in the range 100nm - 2μm, and the key figures-of-merit for our devices are reported below.

5.3. Hall coefficient & offset resistance

Hall coefficients were measured at room temperature for a large number (~65) of Hall probes, with wire widths in the range 0.1 - 2 μm and a 10 μA Hall current (c.f., fig 5.1). Data are shown for sensors fabricated in both 50nm (circles) and 70nm (triangles) thick Bi Films, and are consistent with the expectation that the Hall coefficient is constant for a given Bi thickness. Rather large fluctuations around the mean indicated in each case by a horizontal dashed line are observed and this is smaller for the 70nm probes (R_H(70 nm) ≅ 0.85 Ω/T) than the 50 nm probes (R_H(50 nm) ≅ 1.8 Ω/T). Figure 4.5 in chapter four suggests that the large fluctuations from probe to probe are almost certainly linked to the rather random granularity of the Bi films. The largest fluctuations are probably seen in the 70nm thick sensors because the grain structure in these films seems to be slightly coarser than in the 50nm ones.

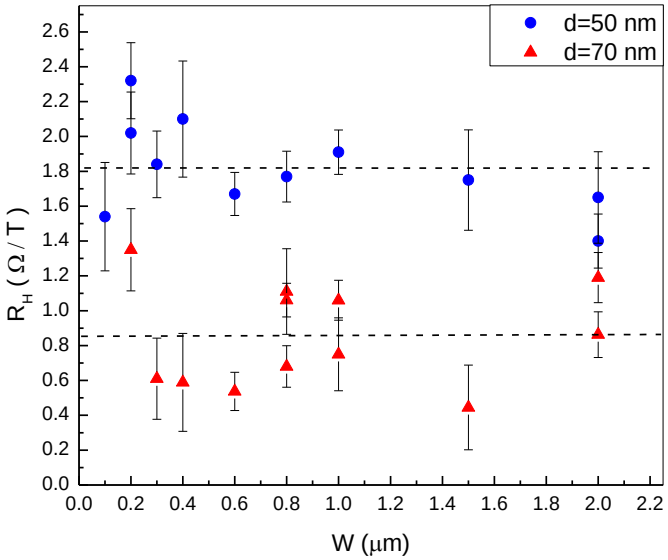

Fig 5.1: Hall coefficient measured at room temperature as a function of cross wire width for probes fabricated in 50nm (circles) and 70nm (triangles) thick Bi films.

Theoretically, when the external magnetic field is zero a Hall sensor should give a zero voltage. However, the performance of Hall effect sensors is frequently limited by offset resistances arising from misalignment of Hall voltage contacts or spatially inhomogeneous current flow in the Hall probe itself (c.f., fig.5.2). It is necessary to keep resulting offset voltages to a minimum, as they limit the gain and fidelity of the preamplification stage used in the detection scheme. The offset resistance is defined as $R_{off} = V_H(H=0)/I_H$, where V_H(H=0) is the Hall voltage at zero magnetic field and

I_H is the Hall probe current. Figure 5.2 shows offset resistance at 300K for the same probes shown in figure 5.1. A very large spread in the distribution of offset resistances is found, with those for the 70nm thick samples generally being larger than for the 50nm samples. It is presumed that this is related to the rather random granular structure of the films. In the smallest sensors the width of the active area is comparable to the grain size, and inhomogeneous current flow through grains and grain boundaries is to be expected. Nevertheless the offset resistance of ideal structures can be as low as ~0.1Ω, corresponding to an effective field of about 50-100mT.

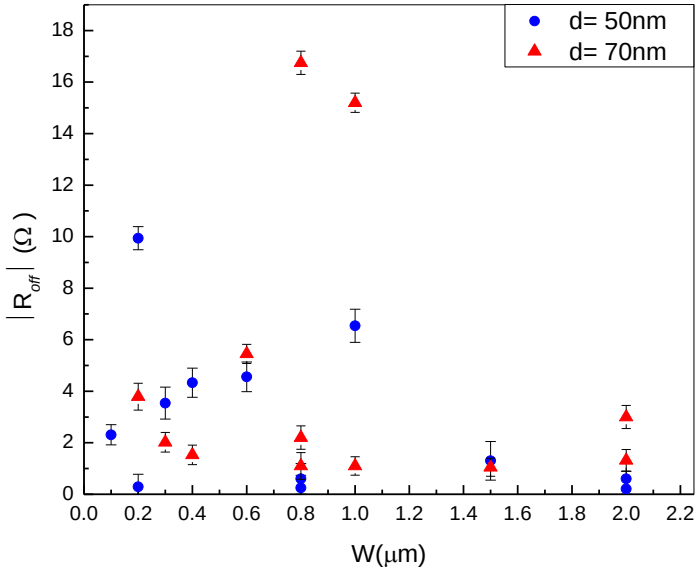

Fig 5.2: Offset resistances measured at room temperature as a function of cross wire width for probes fabricated in 50nm (circles) and 70nm (triangles) thick Bi films.

5.4. Noise spectra & minimum detectable fields

Noise is a feature of any kind of conductor and depends on size, frequency, resistance, temperature and drive current. The high frequency noise of our Bi sensors is dominated by (white) Johnson noise. This is generated by thermal agitation of electrons in a conductor and is independent of the applied voltage. The Johnson noise level is dependent only upon the temperature, the measurement bandwidth, and the value of the resistance. Therefore, the only way to reduce the thermal noise content is to reduce the temperature of operation, the bandwidth or the resistance in the circuit [130]. However, low frequency “1/f “ noise always dominates below a characteristic corner frequency. Here the noise power typically varies inversely with frequency, and 1/f noise is a feature of a very wide variety of physical systems. 1/f noise has a broad range of possible origins, such as carrier fluctuations due to trapping/detrapping at defects or electron-hole generation-recombination processes [96,131]. It is also a key factor when trying to measure low magnetic fields with micro-Hall devices [132].

The signal-to-noise ratio (SNR) of our Bi Hall probes is limited by their frequency-dependent noise voltage, $V_n(f)$. At high frequencies, above the 1/f noise corner, the SNR is governed by thermal Johnson noise, V_J [26].

$$V_J = \sqrt{4R_V k_B T \Delta f}\ , \qquad (5.1)$$

where R_V is the resistance between the voltage leads, k_B is the Boltzmann constant, T is the temperature and Δf the measurement bandwidth. At low frequencies the spectrum is dominated by 1/f noise [96]. The amplitude of the 1/f noise and the location of the 1/f noise corner increase quite rapidly as the sensor current increases.

The noise spectra at three different Hall currents for a 0.3 μm wire width sensor fabricated in a 70nm Bi film is shown in figure 5.3. These data have been captured with a preamplifier gain of $G=10^4$ and the horizontal dashed line indicates the high frequency Johnson noise floor, corresponding to a voltage lead pair resistance of 2.9kΩ, close to the value of 3.5kΩ measured independently. Obviously, the low frequency noise grows rapidly with Hall current and the 1/f shoulder simultaneously shifts to higher frequency, rising above our measurement frequency range at I_H=73 μA.

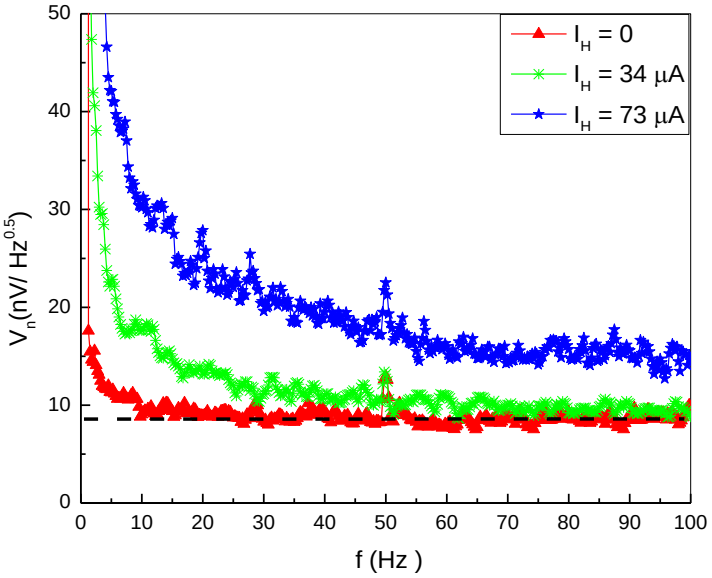

Fig 5.3: Noise spectral density, V_n, as a function of measurement frequency for a 0.3μm wire width Hall sensor patterned in a 70nm Bi film at three Hall probe currents at 300K. The horizontal dashed line indicates the high frequency Johnson noise floor.

The minimum detectable field, $B_{min,}$ is one of the most useful figures of merit for a Hall sensor, defined as the magnetic field at which the Hall voltage equals the noise voltage. At frequencies above the 1/f noise corner this can be approximated by:

$$B_{\min} = \frac{\sqrt{4R_V k_B T \Delta f}}{I_H R_H}. \qquad (5.2)$$

Figure 5.4 shows the minimum detectable field plotted as function of Hall cross wire width for various measurement currents. Patterning smaller Hall probes leads to a rapid increase in the minimum detectable field, due to their higher current densities for comparable Hall currents, and hence larger 1/f noise. Optimal Hall probes with wire widths ≥1 μm are found to have minimum detectable fields ~0.1mT/Hz$^{0.5}$ for Hall currents >70μA, while deep sub-micron probes have values in the range (0.1-1) mT/Hz$^{0.5}$ for Hall currents in the range 5-20μA.

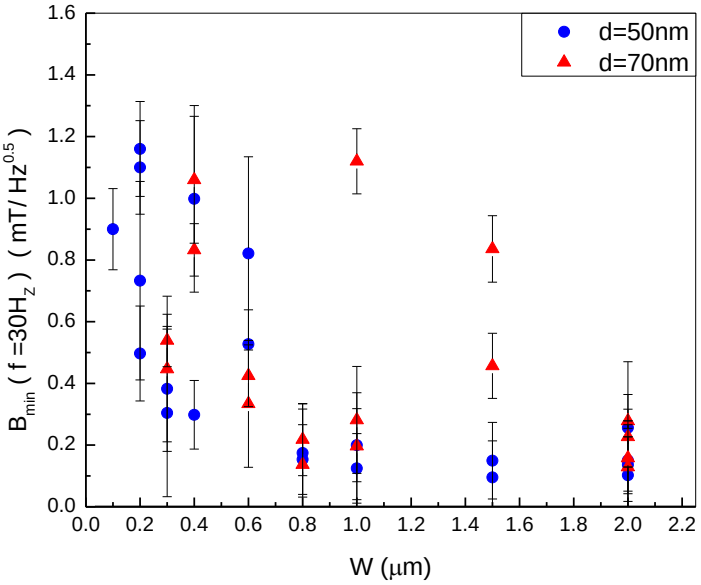

Fig 5.4: Minimum detectable fields at *f*=30Hz as a function of cross wire width for probes fabricated in 50nm (circles) and 70nm (triangles) thick Bi films.

5.5. Discussion - comparison with competing sensors

The Hall coefficient of Bi thin films is a strong function of the substrate material, film thickness and deposition method/conditions [133]. The average Hall coefficients measured in sensors of approximately 1.81Ω/T (0.85Ω/T), for devices fabricated from 50nm (70nm) thick Bi films, compares reasonably well with similar samples reported in the literature. In this context Sandhu *et al*. [126] found R_H=4.0 Ω/T in a 50nm probe FIB milled in a 60nm Bi film deposited on semi-insulating GaAs. This somewhat larger value for R_H could have arisen as a consequence of the much more rapid evaporation rate (~10 x faster) used to grow their Bi films, leading to a finer grain size and the loss of more free carriers to surface traps. Petit *et al*. [127] found R_H=1.73 Ω/T in a 750nm probe FIB-milled in a 78nm thick Bi film grown on an oxidised Si substrate. This Hall coefficient is much closer to typical values measured in our sensors and any difference can probably be attributed to the different choice of substrate. Previous investigations of Bi sensors have shown a reduction of Hall coefficient with increasing current [127] something attributed to an increase in the sensor temperature combined with a negative temperature coefficient for R_H(T). Only a few publications report values for typical offset resistances. Petit *et al*. [128] report a value of 26.6 Ω in 40nm wide probes FIB milled into a 50nm thick Bi film. This is substantially larger than is typically measured in our smallest sensors, suggesting that FIB milling might significantly increase current inhomogeneity in such small devices.

The minimum detectable fields at room temperature of our smallest Hall probe sensors will now be compared with similar sized devices reported in the literature. This is complicated by the fact that many authors frequently present estimates based only on Johnson noise, corresponding to the limit when the measurement frequency is well above the 1/f noise corner. This significantly underestimates the true noise level at lower frequencies. Adopting this approach initially, the high frequency minimum detectable fields for our 100nm sensors are ~10-80μT/Hz$^{0.5}$ for Hall currents in the range 5-40μA. This is reasonably consistent with 70 μT/Hz$^{0.5}$ in the 50nm Bi probes of Sandhu *et al*. [126] and 5.1μT/Hz$^{0.5}$ for the larger 750nm Bi probes of Petit *et al*. [127]. Making a wider comparison with other materials systems which report B_{min}~10 μT/Hz$^{0.5}$ for the 0.8μm GaAs/AlGaAs sensors of Vervaeke *et al*. [98], 0.72 μT/Hz$^{0.5}$ for the 500nm InSb sensors of Gregory *et al.* and Sandhu *et al*.

[119,120], 0.5 $\mu T/Hz^{0.5}$ in the 5μm GaSb/InSb probes of Grigorenko *et al*. [121] and Kazakova *et al*. [123] and 0.4 $\mu T/Hz^{0.5}$ in the 2μm $In_{0.15}Ga_{0.85}As$ quantum well sensors of Pross *et al*. [124]. Most of these Hall probe sensors are considerably larger than the smallest Bi probes measured here and hence the lower noise levels are not surprising. The noise figures reported by Sandhu *et al*. [120] for their 500nm structures are impressive, however the growth of epitaxial InSb thin films remains a major challenge, and it is not clear that it would be possible to make these devices much smaller.

A more realistic estimate of the minimum detectable field is obtained by directly measuring the spectral noise density at typical operation frequencies. Our data focus on the noise at 30 Hz, since this is the typical detection frequency used to operate our sensors, and assume that the noise spectrum with such a low frequency ac current approximates to that with a dc drive of the same mean density. For our 100nm sensors fabricated from a 50nm Bi film this yields an upper bound of B_{min}=0.9mT/$Hz^{0.5}$ with a 5μA Hall current. However, in order to avoid sensor damage the current density has been kept low and the optimal drive current is probably up to ten times larger. Using larger currents in 200nm and 300nm sensors the measured minimum detectable field dropped to 0.5mT/$Hz^{0.5}$ and 0.3mT/$Hz^{0.5}$ respectively. Petit *et al*. [127] report the measured noise spectra as a function of size for probes FIB-milled from 78nm Bi films. For a 100 nm probe, a value of B_{min}(30Hz)~2 mT/$Hz^{0.5}$ can be interpolated. This is significantly higher than in our somewhat thinner EBL sensors, possibly due to FIB induced damage and/or Ga^+ ion incorporation. All comparisons with equivalent sized Bi Hall probes reveal that our best probes exhibit similar or better minimum detectable fields in all cases. Turning again to other materials systems, Vervaeke *et al.* [98] report optimum values of B_{min}(30Hz)~0.1mT/$Hz^{0.5}$ in 0.8μm GaAs/AlGaAs sensors. At the same measurement frequency Kazakova *et al*. [123] report 0.056 mT/$Hz^{0.5}$ in 5μm GaSb/InSb probes and Pross *et al.* [124] report 0.4 mT/$Hz^{0.5}$ in 2μm $In_{0.15}Ga_{0.85}As$ quantum well devices.

The ideal minimum detectable fields for these alternative materials systems are all slightly lower than that measured in our Bi sensors. Nevertheless these data are for devices that are typically more than an order of magnitude larger than those studied here. Therefore, it is not possible to compare directly with these semiconductor devices and it is not at all clear that they can be fabricated with deep sub-micron

dimensions. The devices shown in this chapter have exhibited noise levels which are lower than those made by FIB milling, suggesting that the elimination of FIB damage and Ga^+ incorporation through the use of lift-off fabrication techniques does indeed lead to superior figures of merit in these Bi sensors.

There is a still much more research which could be done to optimise the figures of merit of Bi Hall effect sensors. Recently Kubota *et al.* [129] used advanced electron beam lithography and lift-off techniques to fabricate static 50 nm Hall probes in a 100 nm Bi film . When the Bi film is much thicker the sensor has lower lead resistances and much higher Hall currents can be used. They report values of B_{min}~0.012 $mT/Hz^{0.5}$ measured at a frequency of 1000Hz. The same approach could be used to optimise scanning sensors, although there is a price to pay in spatial resolution because the local magnetic induction can no longer be assumed to be uniform throughout the depth of the film. The noise spectra of our Bi probes require much more comprehensive investigation as a function of Hall current, to optimise sensor performance. Higher drive currents lead to an increase in 1/f noise but this is partially balanced by the higher effective sensitivity of the sensor, and a customised optimisation of each individual sensor is often required.

Finally, the thin films from which these Hall devices are fabricated can still be improved to achieve better figures of merit. Sandhu *et al*. [126] find higher Hall coefficients in films which used very high evaporative deposition rates. High growth rates would also be expected to yield a finer-grained microstructure, leading to lower current inhomogeneity and lower offset resistances. It has recently been demonstrated that nanoscale mechanical polishing of Bi films deposited on oxidised Si substrates leads to much smoother films, without degrading the crystal structure or resistivity [134]. This approach could be used to improve the figures of merit of Hall devices, as well as enable the fabrication of even smaller sensors using advanced etching techniques.

Chapter six

Crossing vortex lattices in very high in-plane magnetic fields

6.1. Introduction

A single crystal sample of $Bi_2Sr_2CaCu_2O_{8+\delta}$ (Bi-2212) with a critical temperature T_c= 88.8K $\pm$ 0.6K has been investigated by scanning Hall probe microscopy. Vortex structures in anisotropic layered superconductors such as Bi-2212 have been extensively investigated in recent years, and are known to display a rich vortex phase diagram, dependent on the direction and strength of the magnetic field. When the external applied magnetic field is inclined away from the c-axis (so that it has a component along the CuO_2 planes), the different components of magnetic flux generate two different types of magnetic vortices: pancake vortices (PVs) whose supercurrents are confined to the superconducting planes that are responsible for the perpendicular field component, and Josephson vortices (JVs) located between the superconducting planes with currents flowing in and between CuO_2 planes that are responsible for the in-plane field [57,135]. In 1999, Alex Koshelev predicted the crossing vortex lattices ground state and calculated a reduction of the PV lattice melting field with an applied in-plane field [57]. The “combined lattice” or "crossing lattices" regime of Abrikosov pancake vortices (PVs) and Josephson vortices (JVs) only exists in highly anisotropic layered superconductors in a tilted magnetic field [136] due to their mutual attractive interaction arising from the displacement of PVs by JV supercurrents. As a consequence the normally straight PV lines assume 'attractive' S-shaped distortions around JVs. This results in a mutual attraction and an accumulation of PVs on JV stacks leading to chains of enhanced PV density. The presence of vortex chains in tilted fields due to an attractive component of the interaction at long distances was also later predicted by Buzdin and Baladie [58].

Many recent studies on Bi-2212 samples using various imaging techniques have focused on the investigation of interacting Josephson and pancake vortices. The first imaging of crossing lattices was achieved with Bitter decoration at the University of Bristol by Grigorieva *et al* [137]. Using SHPM Grigorenko *et al.* [56] observed for the first time that isolated chains could be realised composed of JV stacks decorated with PVs. These authors systematically studied the vortex phase diagram as a function of PV density and discovered several new vortex regimes. The first M-O

images of crossing lattices in Bi-2212 were captured by Vlasko-Vlasov *et al.* at Argonne National Labs who reported the behaviour of Josephson vortices that have been decorated by pancake vortices in single crystals of Bi-2212 at 85K [138]. Later Grigorenko *et al.* [139] used SHPM to image interacting crossing pancake vortex (PV) and Josephson vortex (JV) lattices in highly anisotropic $Bi_2Sr_2CaCu_2O_{8+\delta}$ single crystals in the presence of quenched disorder, and confirmed that the PV/JV attraction arises from small PV displacements in the presence of JV supercurrents In 2011 Segev *et al.* [140] used differential magneto-optics (DMO) to image PV-decorated JVs in a Bi-2212 single crystal with anisotropy $\gamma = \frac{\lambda_c}{\lambda_{ab}} \approx 500$, where λ_c and λ_{ab} are the out-of-plane and in-plane penetration depths. They showed that the JV lattice has a pronounced effect on the melting process of the vortex lattice in Bi-2212 under tilted magnetic fields, reducing the melting field of the PV lattice according to the relationship $H_m=12.4 – (4x10^{-3}$ x $H_{//}(Oe))$ at $T_c=87K$. Butsch *et al.* [141] reported that melting of crossing flux line lattices sets in along the planes containing JV stacks where the local melting temperature can be very substantially lower than in the bulk, resulting in a periodic solid-liquid structure.

One of the big challenges of working with vortex matter in type II superconductors is achieving an equilibrium configuration - indeed observed vortex structures frequently correspond to metastable states. In this work nearly equilibrium vortex configurations have been prepared by oscillating $H_{//}$ around a mean value (i.e., vortex dithering) for a few seconds, which is an established way of equilibrating vortex distributions in cuprate superconductors [142]. Figure 6.1 shows example images for $H_{//}$ = 200 Oe and H_z= 6 Oe with and without dithering. Clearly a more homogenous vortex distribution is achieved after dithering the in-plane field.

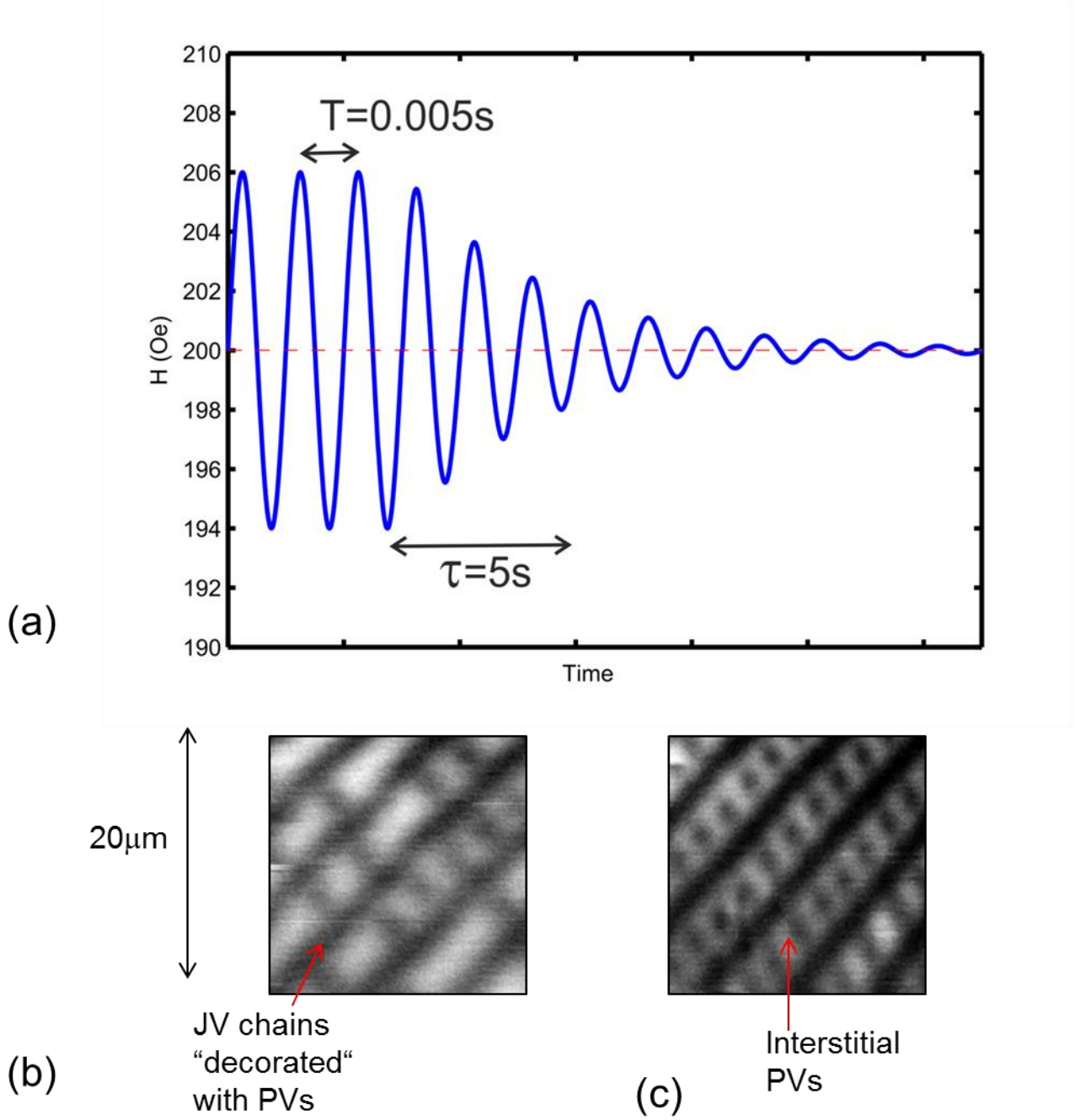

Figure 6.1: More uniform and reproducible vortex distributions are achieved when dithering is used by Labview program. (a) Plot of the time-dependent in-plane field during dithering at a frequency of 200Hz at an in-plane dither field amplitude of 6 Oe. The out-of-plane field dither was 3 Oe at 10Hz with the same exponential decay and was performed immediately before the in-plane dither. Vortex distributions at T= 85K and fields of $H_{//}$ = 200 Oe and H_z = 6 Oe without (b) and with (c) dithering.

6.1.1 Motivation for these new experiments

In the present work, high resolution scanning Hall probe microscopy has been used to study interacting crossing lattices in order to search for novel phases of vortex matter in single crystals of the high temperature superconductor $Bi_2Sr_2CaCu_2O_{8+\delta}$ at very high in-plane magnetic fields. The evolution of coupled Josephson and pancake vortices in highly anisotropic Bi-2212 has been investigated as a function of temperature and applied in-plane and out-of-plane magnetic fields. JV stacks can clearly be identified in the SHPM images via the PVs that 'decorate' them when small out-of-plane fields (H_z~0.5-10.0 Oe) are combined with very high in-plane fields ($H_{//}$~50-650 Oe). The JV spacing has been carefully studied as a function of $H_{//}$ at fixed out-of-plane field, and as a function of H_z at fixed in-plane field.

The specific aims of this project are to search for novel phases of vortex matter and new properties of crossing vortex lattices in highly anisotropic cuprate single crystal superconductors at very high in-plane fields when the PVs on adjacent chains start to interact strongly. The spacing of JV chains, C_y, has been systematically quantified as a function of in-plane and out-of-plane fields. Unexpectedly, it is found that the effective anisotropy of the JV lattice, γ_{eff}, depends strongly on the PV density, and the JV chain spacing varies discontinuously as a function of both H_z and $H_{//}$ as interstitial rows of free PVs are created or destroyed. Currently, a theory to quantitatively describe these phenomena is being developed by Alex Koshelev at Argonne National Laboratories, USA.

6.2. Decorated JV stack spacing as a function of in–plane field at fixed PV density.

The relationship between the applied in-plane magnetic field, $H_{//}$, and the separation of vortex chains,C_y, in single crystals of the highly anisotropic cuprate superconductor Bi-2212 has been studied using SHPM. The fields parallel and perpendicular to the sample plane were produced by two separate sets of coils which allowed one to vary the field components independently. It was observed that the distance between JV chains normally decreases with increasing $H_{//}$ and the density of chains increases until they start to interact strongly when the separation becomes of order λ_{ab}. Figure 6.2 presents a set of SHPM images for a Bi-2212 single crystal as a function of increasing in-plane field with constant out-plane fields (H_z=5 and 10 Oe). The greyscales (shown below in green) peak when JV chains are 'full', just before the first interstitial PV appears. The images show chains of JV stacks, 'decorated' by (white) PVs, whose spacing decreases with in-plane magnetic field. Clear consequences of the discrete number of rows of interstitial PVs in-between the JV chains are observed. In small in-plane fields, the decorated Josephson vortices are not completely regularly spaced due to disorder in the crystal as well as mesoscopic effects due to the small and finite number of interacting PVs which can only form full PV rows at discrete values of $H_{//}$. The equilibrium separation between PVs on a JV stack is controlled primarily by the in-plane field, $H_{//}$. The images exhibit JV chains with free PVs between them. The distance between adjacent JV chains is not constant and discrete jumps are seen as the free PV rows between chains disappear at high $H_{//}$.

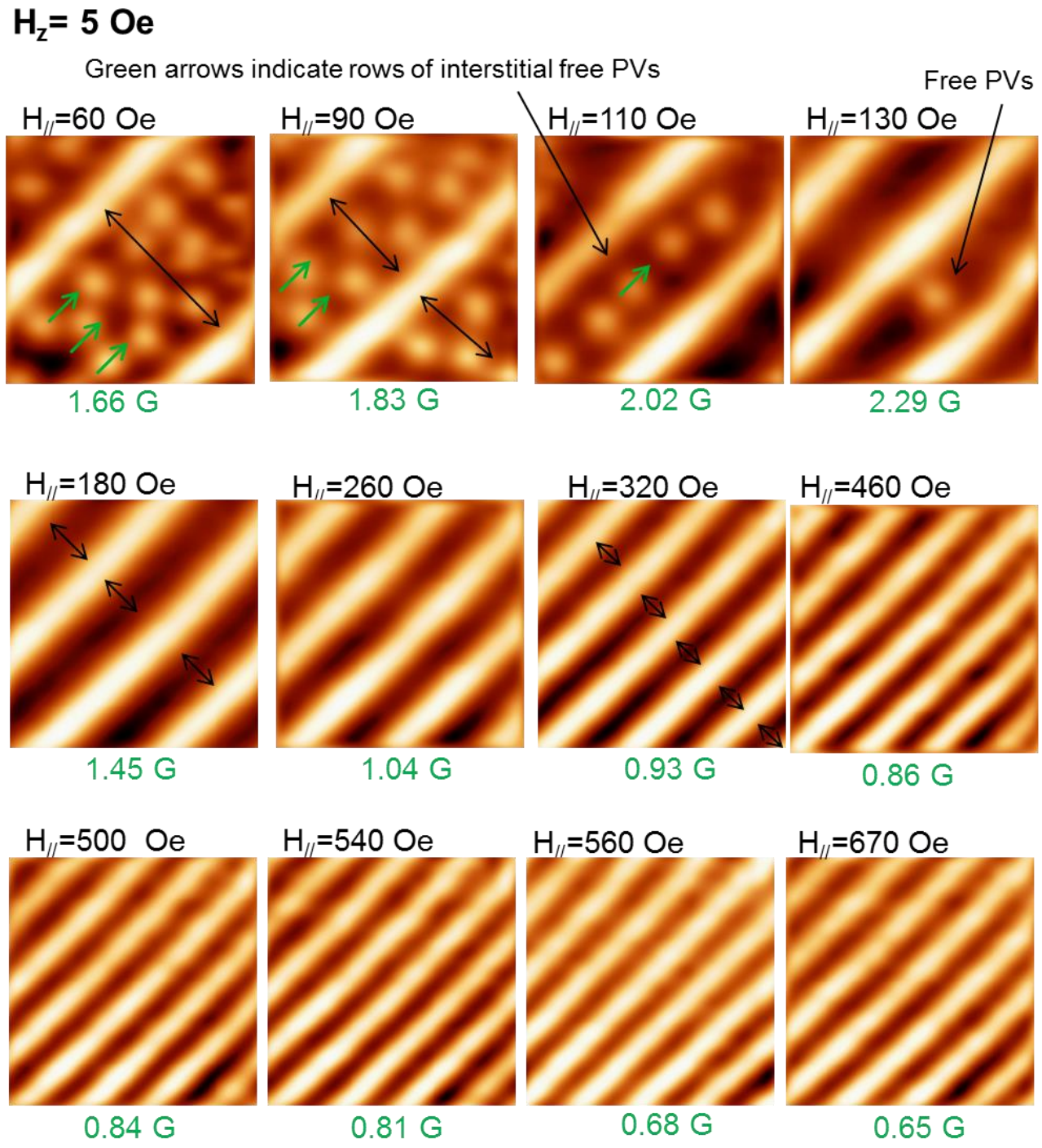

Figure 6.2: (a) SHPM images showing that the distance between chains decreases with increasing in-plane field for fixed out-plane-field = 5 Oe at T= 85K. Fluctuations in the JV chain spacing as a function of $(H_{//})^{-0.5}$ are observed. The image size is ~20x20 μm^2. Image greyscales are recorded below in green.

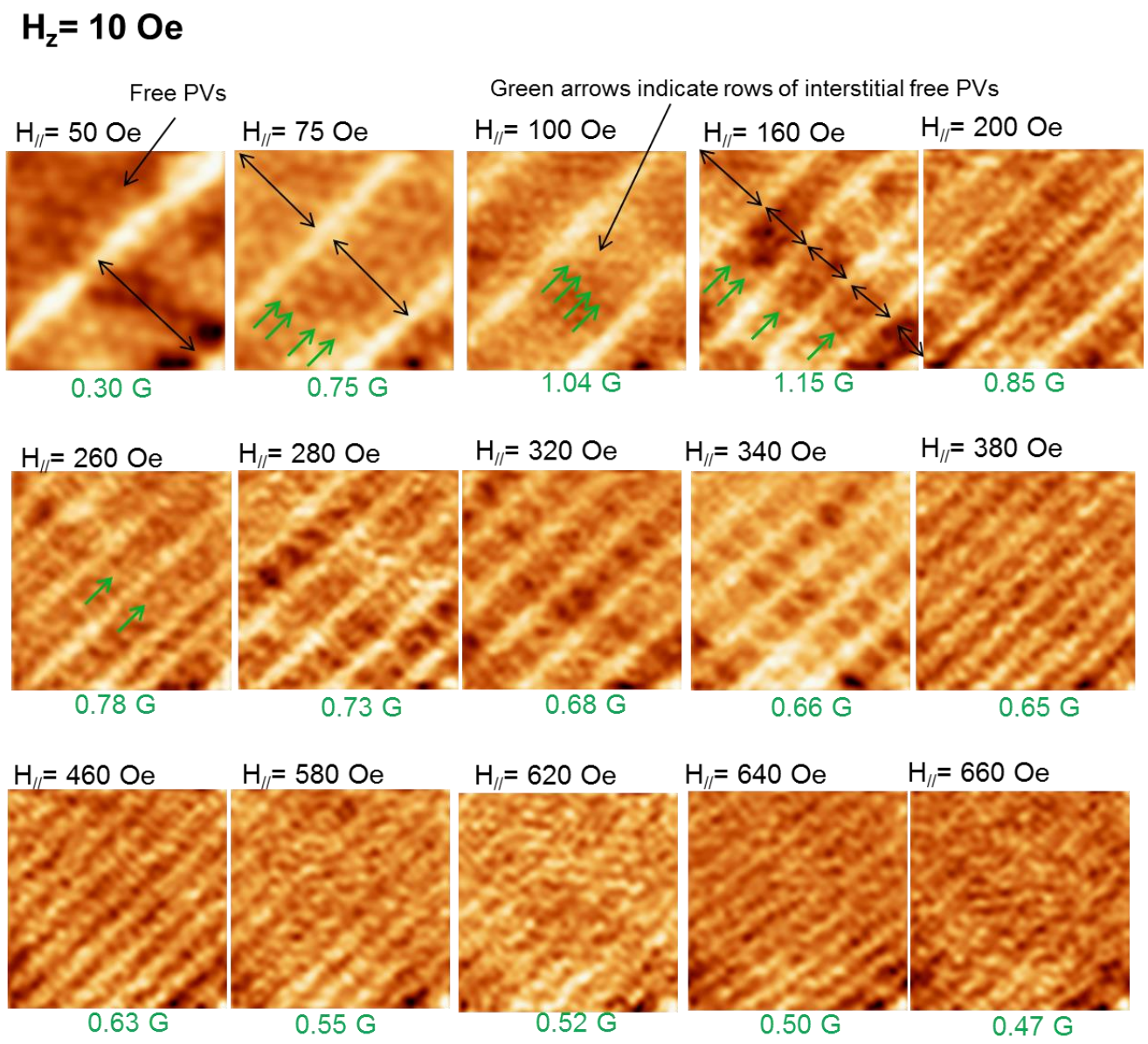

Figure 6.2: (b) SHPM images showing that the distance between chains decreases with increasing in-plane field for fixed out-plane-field = 10 Oe at T= 85K. Fluctuations in the JV chain spacing as a function of $(H_{//})^{-0.5}$ are observed. The image size is ~20x20 μm^2. Image greyscales are recorded below in green.

The image grayscale at fixed PV density is plotted in figure 6.3 as a function of in-plane field. The greyscale is the difference between the maximum and minimum magnetic field values across the whole image. [$\Delta B\ (G) = B_{max} - B_{min}$] and it is seen to start low and then jump to a peak (as indicated by arrows) before gradually decreasing to a relatively stable 'saturation' value for $H_{//} > 400$ Oe. Note that the greyscale is appreciable larger at the smallest H_z because PVs have the largest average separation at this field.

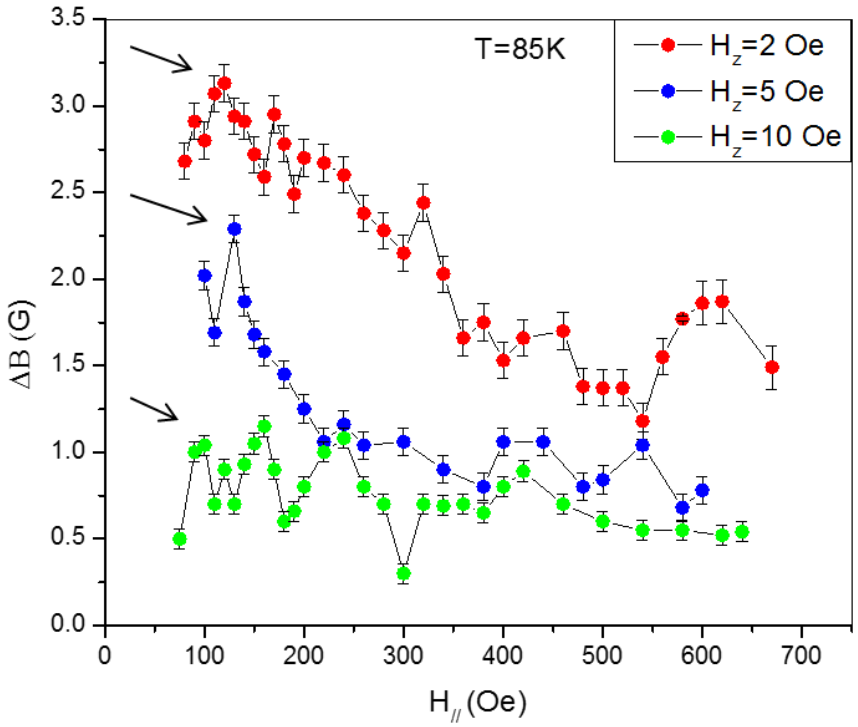

Figure 6.3: Grayscale of images plotted as a function of in-plane field for three different values of H_z.

The average JV chain spacing is plotted in figure 6.4, where error bars have been estimated from the variation of different JV chains in the image. Upon increasing the in-plane magnetic field, the distance between JV chains decreases and the number of chains increases. For a non-interacting JV lattice C_y is expected to depend linearly on $(H_{//})^{-0.5}$ [57].

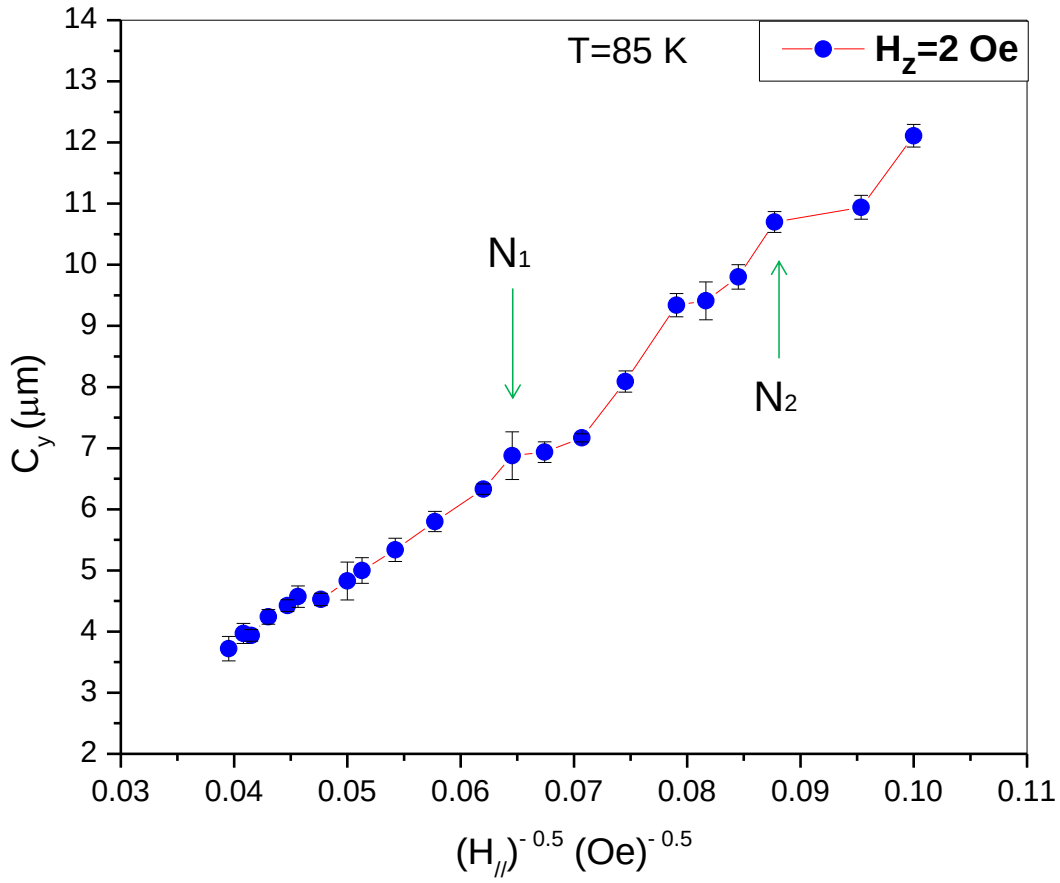

Figure 6.4: Plot of JV chain spacing as a function of $(H_{//})^{-0.5}$ at fixed H_z=2Oe.

Oscillations in the JV chain spacing are observed as a function of the square root of the inverse in-plane field. The maximum of these appear to be correlated with fields where there is exactly an integer number of rows of free PVs between 'decorated' JV stacks. Here N_1 indicates the observed location of the structure with exactly one chain of free PVs at $H_{//}$ =200 Oe for H_z= 2 Oe which is close to the onset of the first peak in figure 6.4. N_2 corresponds to a structure with two rows of free PVs observed at $H_{//}$ =130 Oe and lies close to the onset of the second peak. These structures are sketched in figure 6.5. In principle there can be an infinite number of free PV rows (i.e., $0 \leq N \leq \infty$).

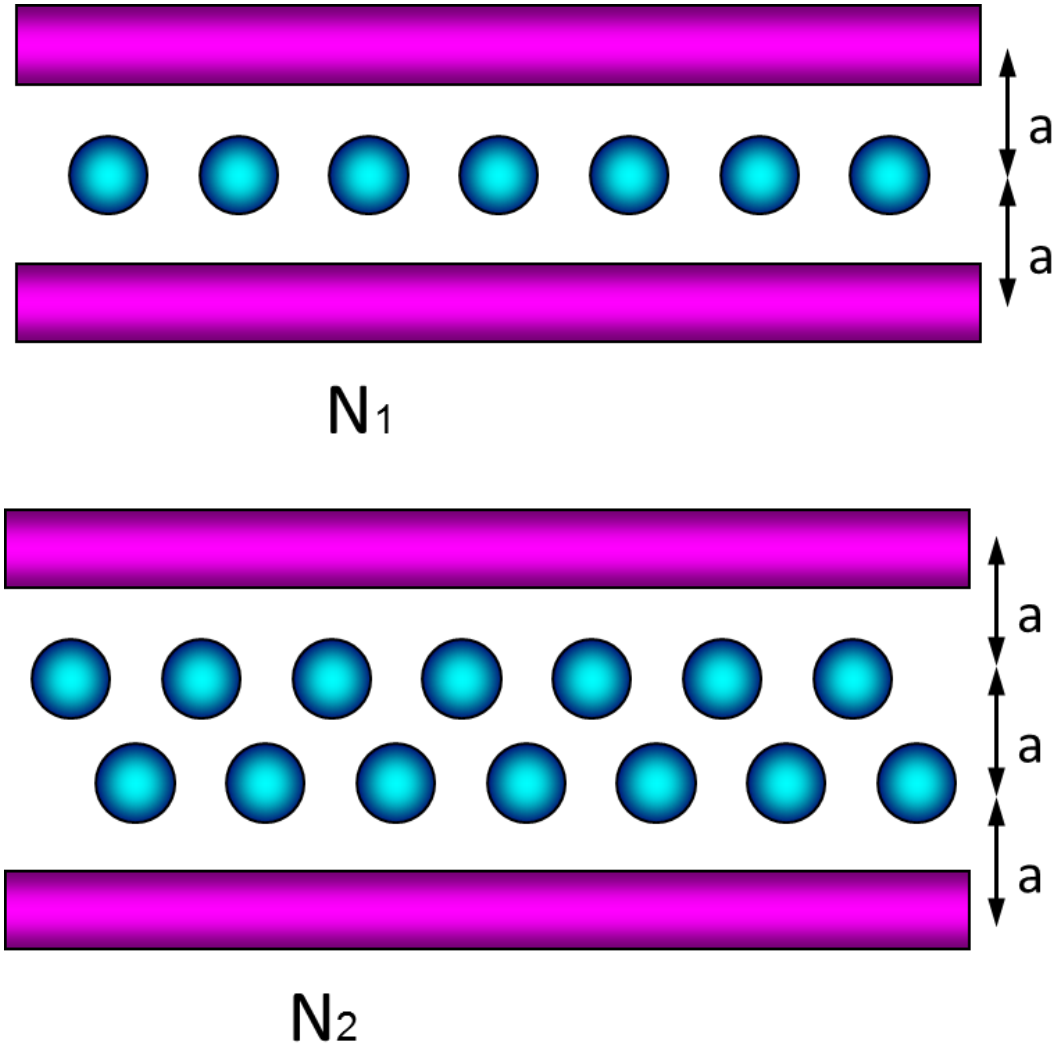

Figure 6.5: Sketch of the vortex structures indicated by N_1 and N_2 in figure 6.4. Here a represents the perpendicular separation between PVs and is assumed to be the same for decorating and free PVs.

The JV stack spacing as a function of $(H_{//})^{-0.5}$ is shown for a large number of values of H_z in figure 6.6. It is expected that the chain spacing is proportional to $\sim(H_{//})^{-0.5}$ when the slope of figure 6.6 would be proportional to $\gamma^{0.5}$ and the plots should ideally be straight [139,143]. Experimentally it was found however that the chain spacing (≡ effective anisotropy) actually decreases with increasing out-of-plane field. γ_{eff} has been calculated from the slope of C_y versus $(H_{//})^{-0.5}$ assuming the following equation holds [56].

$$C_y = \left(\frac{\sqrt{3}\ \gamma_{eff}\ \Phi_\circ}{2H_{//}}\right)^{0.5} \quad , \qquad (6.1)$$

where, C_y is the mean separation of JV chains.

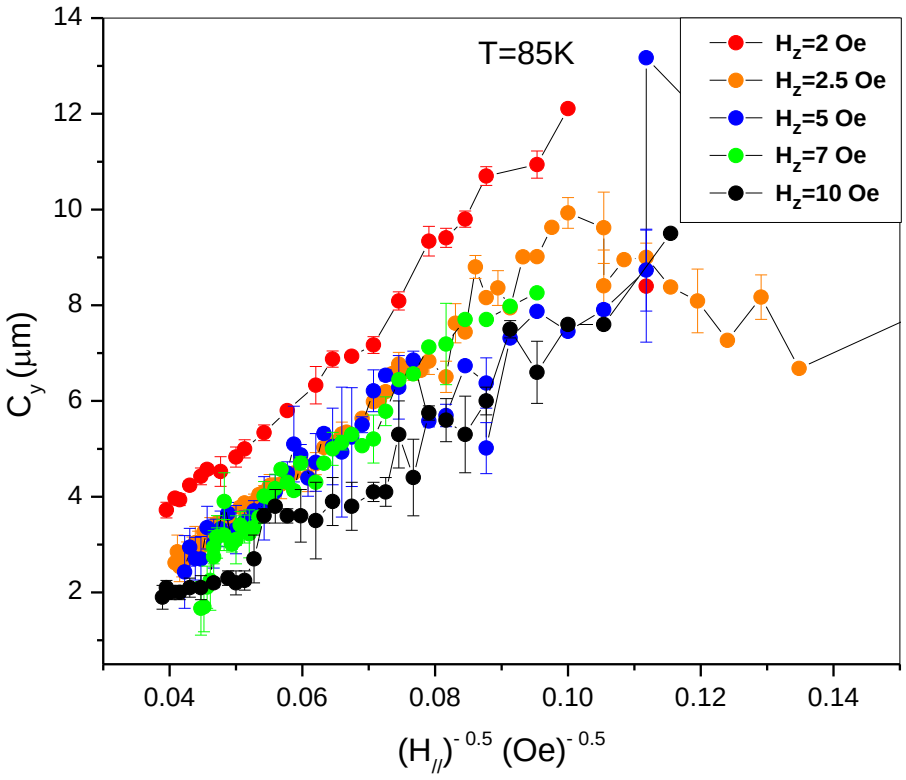

Figure 6.6: Graph of mean JV chain spacing as a function of $(H_{//})^{-0.5}$ at various fixed values of H_z.

The estimated values of effective anisotropy, γ_{eff}, are plotted in figure 6.7 as a function of H_z. A fairly smooth reduction in γ_{eff} with H_z is observed, which does not seem to be very sensitive to dithering conditions. The solid curve represents theoretical predictions of effective gamma from the theory of Koshelev [57] and is given by

$$\gamma_{eff} = \gamma \left(\frac{B_\lambda}{B_Z\, c}\right)^{0.5} \quad , \qquad (6.2)$$

where $B_\lambda = \frac{\Phi^\circ}{4\pi\lambda^2} \ln \frac{\lambda}{r_w}$, ($r_w \sim$ 270 nm) , c = 3.1 and B_Z (H_z) is the out-of-plane magnetic induction.

Equation (6.2) is the result of a calculation that takes into account the effect of PVs on the JV lattice. Effectively the presence of PVs reduces C_y. Here gamma is an intrinsic value of the anisotropy of the JV lattice without interactions with PVs.

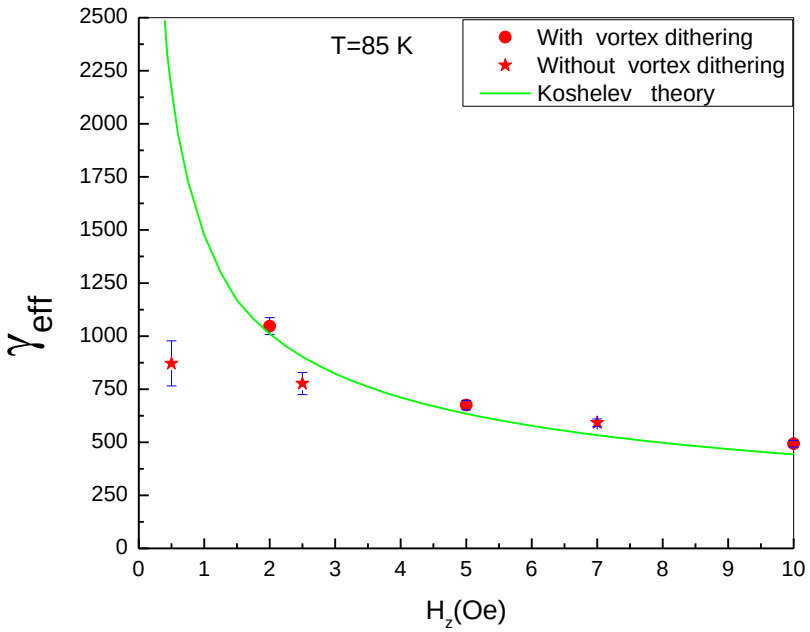

Figure 6.7: Estimated effective anisotropy as a function of out-plane field. Solid circles represent date captured with dithering, while stars were taken without dithering. The solid line is the effective gamma calculated using the expression due to Koshelev with γ =1755 [57].

6.3. Decorated JV stack spacing as a function of PV density at fixed in-plane field.

High-resolution SHPM has been used to study vortex matter in Bi-2212 as a function of H_z at large fixed values of $H_{//}$. In this case the chain spacing is normally expected to be independent of out-of-plane field. However, this is not what is observed. Figure 6.8 shows families of images at low (50 Oe) and high (600 Oe) in-plane fields. The nucleation of rows of free PVs in between the JV chains is indicated by green arrows. We clearly observe that the chain spacing is decreasing with increasing out-of-plane field, which is quite unexpected. Discontinuous changes in the chain spacing are observed when the number of rows of free PVs increases. At high in-plane fields (e.g., 600 Oe), the maximum field of the out-of-plane coil (~28.3 Oe), we were unable to exceed the saturation PV density of the JV chains and no rows of free interstitial PVs are formed. The JV spacing as a function of out-of-plane field at constant in-plane field is plotted in figure 6.9. The spacing of JV stacks clearly ***decreases*** at higher values of H_z. Figure 6.9 also shows a very sharp upward jump in C_y at some value of H_z which depends on $H_{//}$. A careful study of individual images reveals that this is the point at which the first row of free PVs is nucleated.

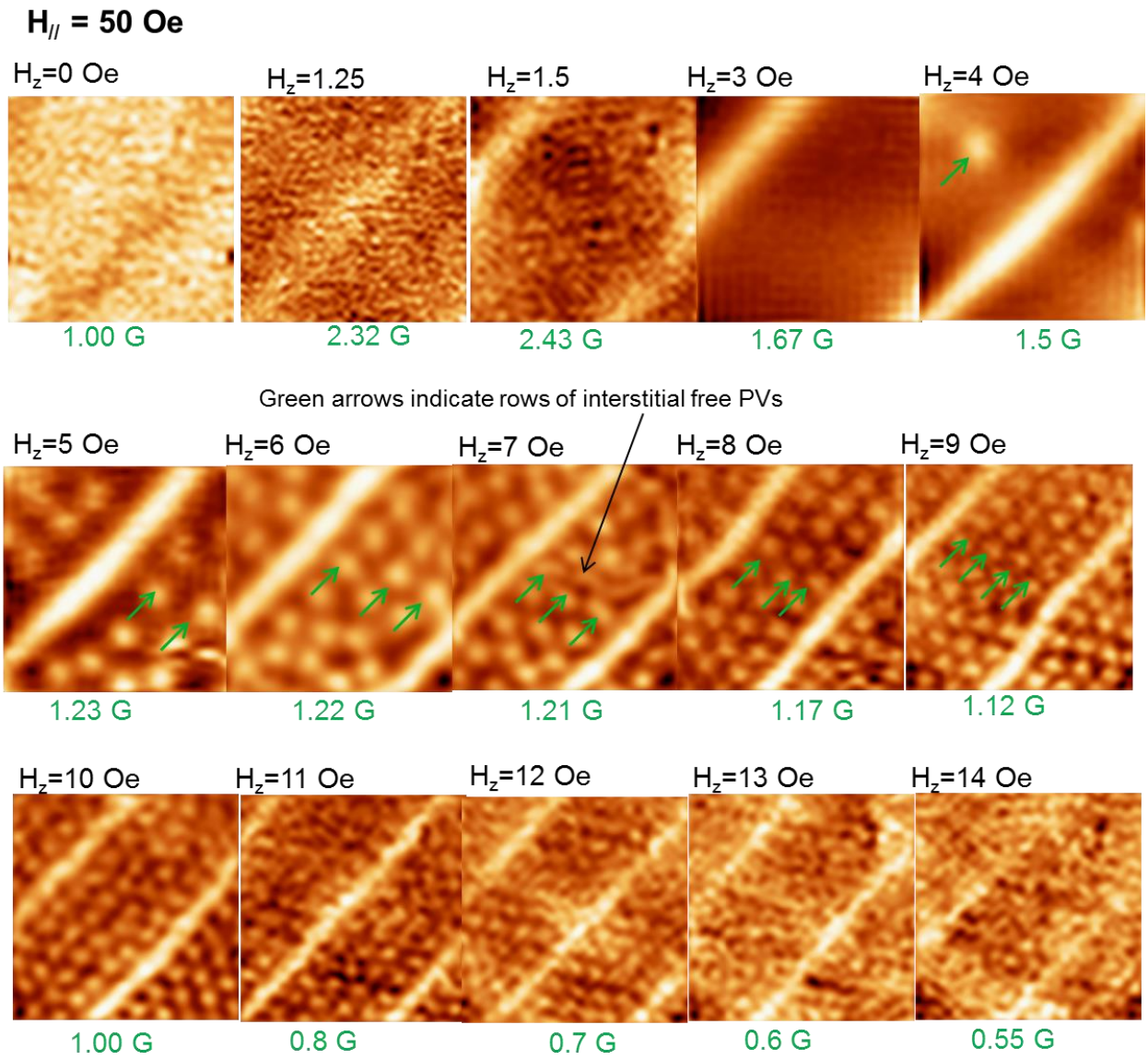

Figure 6.8: (a) SHPM images in a BSCCO single crystal as a function of H_z at two fixed values of $H_{//}$ =50 Oe at T= 85K. The image size is ~20x20 μm^2. Image greyscales are recorded below in green.

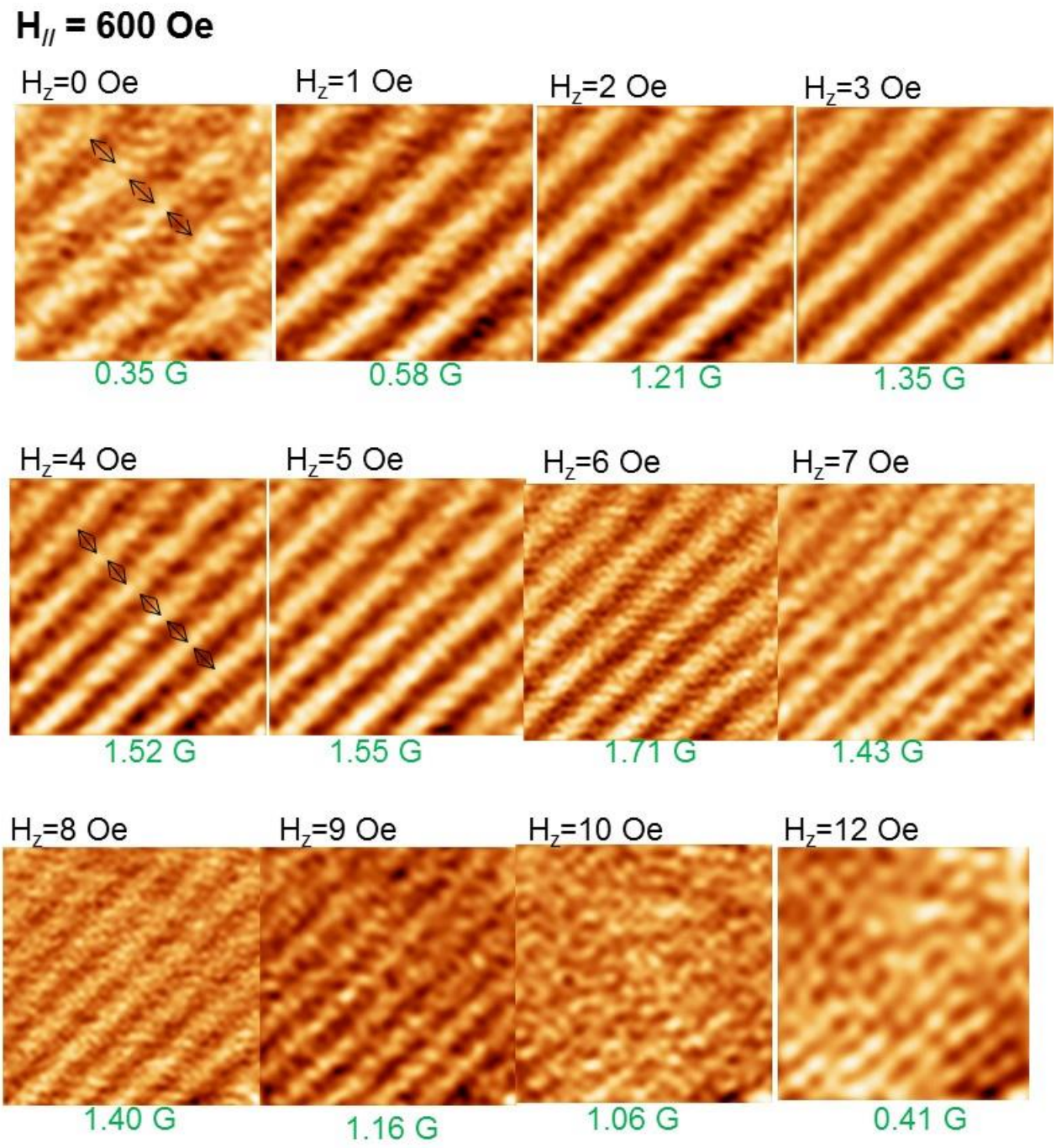

Figure 6.8: (b) SHPM images in a BSCCO single crystal as a function of H_z at two fixed values of $H_{//}$ =600 Oe at T= 85K. The image size is ~20x20 μm^2. Image greyscales are recorded below in green.

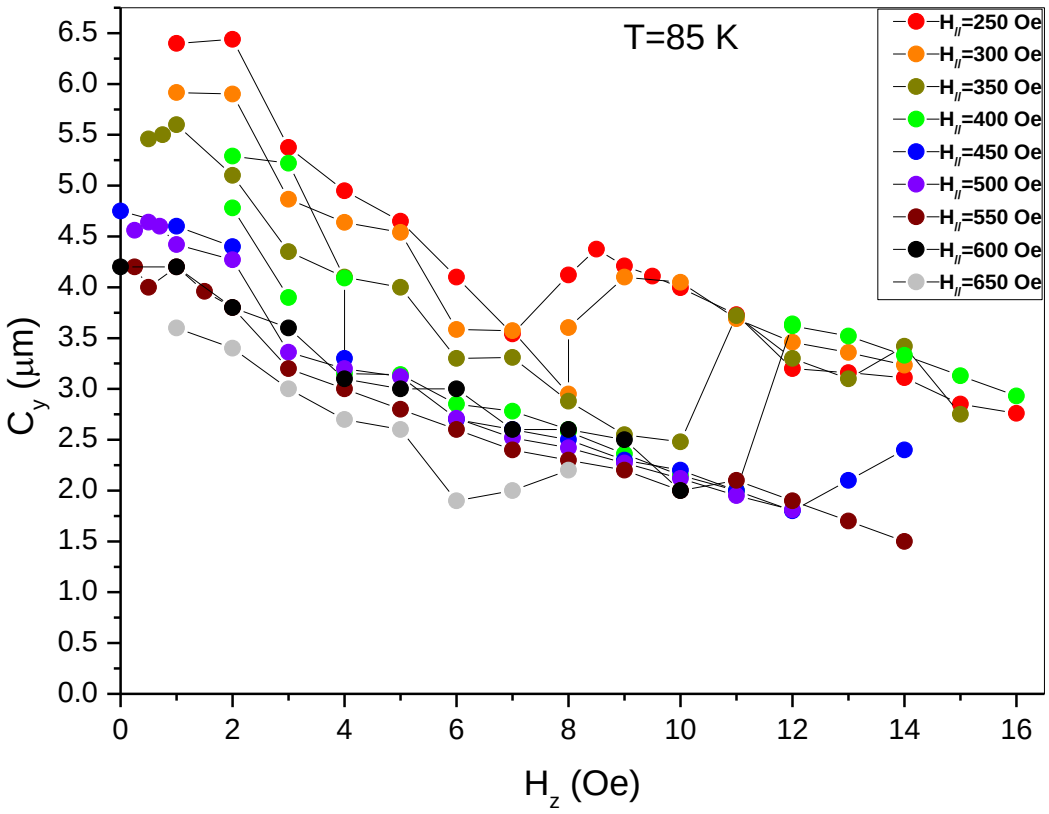

Figure 6.9: JV chain spacing plotted as a function of H_z at constant $H_{//}$.

The grayscales of images of the type shown in figure 6.8 are plotted in figure 6.10 as a function for out-of-plane field. The greyscale is seen to start low and rise quite rapidly to a peak (as indicated by arrows) before gradually decreasing to a relatively stable ‘saturation‘ value for $H_z > 10$ Oe.

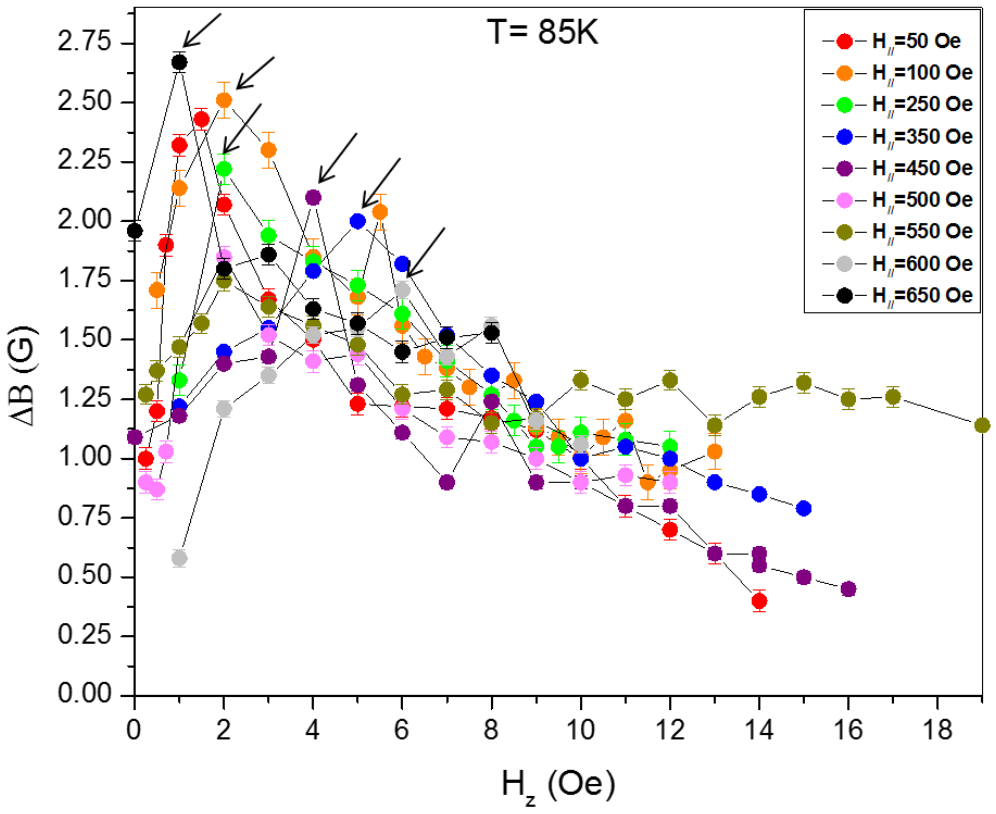

Figure 6.10: Plot of the grayscale of images of the type shown in figure 6.8 as a function of out-of-plane field.

6.4. Structure of ‘decorated’ JV stacks at very high in-plane fields - evidence for new phases.

The structure of JV stacks ‘decorated’ with PVs was studied at very high in-plane fields while the out-of-plane field was gradually increased. Figure 6.11 (a) shows that the JVs actually have roughly triangular profiles at low H_z and seem to show a tendency for a more rounded profile at very high H_z - though some of the rounding could be due to the high background noise level at the highest out-of-plane fields. However, the reduction in amplitude of the chains could partially be attributed to broadening due to the kinking of PV chains (in combination with the fact that the chain spacing gets a bit smaller at higher H_z as well). Figures 6.11 (b), (c) sketch possible PV structures at low (b) and high (c) out-of-plane magnetic fields.

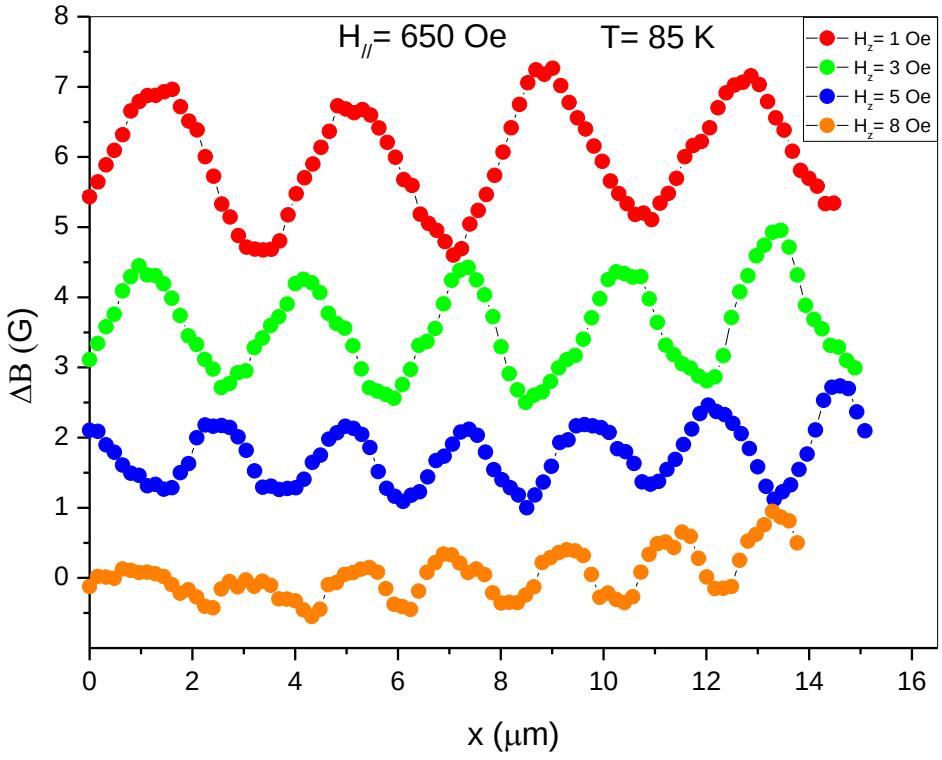

(a)

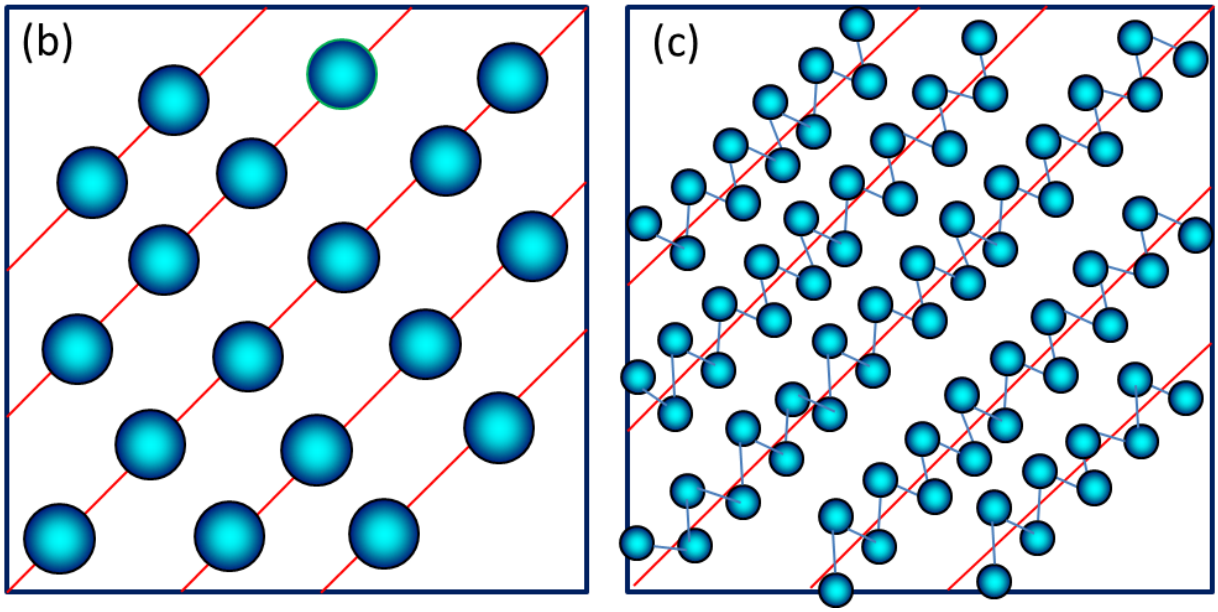

Figure 6.11: (a) Plot of the average JV chain profiles at $H_{//}$=650 Oe and various values of H_z (vertically offset for clarity). (b), (c) sketches of possible PV structures at low (b) and high (c) out-of-plane magnetic fields.

.

6.5. Melting of PVs trapped on JV stacks

One very striking effect of thermal fluctuations in Bi-2212 is the melting of the vortex lattice at temperatures well below the critical temperature, T_c [144]. A first-order melting transition of the Abrikosov vortex lattice due to thermal fluctuations was predicted in 1985 by Brezin *et al*. It was suggested that the mean field formation of the vortex lattice at H_{c2}, that normally occurs via a thermodynamic second-order transition, can be driven into a first order transition by superconducting fluctuations [145].

In recent years the phase diagram of vortex matter in HTSC has been revisited due to the discovery of novel vortex phases and phase transitions [54]. Among them, the most surprising phenomenon is the first-order vortex-lattice melting transition (VLMT) [146]. However, a second-order phase transition in highly anisotropic Bi-2212 is predicted to occur when the magnetic field is tilted away from the *c* axis, especially when it is applied close to the *ab* plane [147,148]. The mean c-axis melting field component H_z^{melt} is known to depend approximately linearly on the in-plane magnetic field $H_{//}$ in Bi-2212, which was shown to be a consequence of the formation of a crossing lattice of Josephson vortices (JVs) and pancake vortex stacks by

Koshelev [149]. Mirkovic *et al.* [150] later presented a study of the melting transition based on in-plane resistivity measurements in oblique magnetic up to very high field amplitudes.

Single crystals of the very strongly anisotropic high temperature superconductor $Bi_2Sr_2Ca_1Cu_2O_{8+\delta}$ have been extensively studied as they exhibit a very rich H-T phase diagram. Recently significant progress has been made in understanding the vortex states and melting transition in layered superconductors such as Bi-2212 with very weak Josephson coupling. The vortices at low temperatures are bound to natural pinning centres and form a regular Abrikosov lattice. However, when the temperature reaches a certain value, T_m, that can be substantially below T_c in strong magnetic fields, thermal fluctuations are strong enough to shake the vortices out of their equilibrium positions. This results in the melting of the lattice when the thermal fluctuations of the vortices reach a certain fraction (~20%) of the mean distance between vortices in the lattice. In this case, the vortices become able to move freely through the crystal, unbound from any pinning centres [25]. Vortex melting is a striking example of a first order phase transition of the vortex lattice in type II superconductors and has been extensively studied [140].

Pancake vortices form in an applied magnetic field perpendicular to the copper oxide layers and the coupling of PVs in different layers arises from rather weak Josephson and magnetic interactions, leading to aligned stacks at low fields and temperatures. As a result of the weak magnetic nature of coupling between PVs, both 'crystalline' order and vertical alignment of PVs are lost at the melting point. Crossing lattices of Abrikosov and Josephson vortices (or tilted vortex chains) exist when the magnetic field is tilted with respect to the *c*-axis. Consequently, the melting transition is determined by the nature of the ground state at tilted fields. However, both PV and JV lattices are thought to melt at the same point since mobile PVs will destroy the JV supercurrents. The direction of the applied magnetic field plays a critical role in defining the resultant vortex lattice structure. In a tilted magnetic field, melting has been shown to occur first in the planes containing the Josephson vortices creating an intermediate periodic lamellar solid-liquid state [141].

Koshelev [57] has shown that the free energy of the crossing lattices state depends linearly on the in-plane field for $B_{//} < \Phi_\circ / (\gamma_{eff}\, s^2)$. The JV cores start to overlap at higher in-plane fields and hence produce only weak zigzag deformations in the PV lattice which have little influence on the JV phase distribution and can be treated as perturbations.

Our SHPM measurements indicate that decorated JV chains are not 'melted' at H_z=28.3 Oe in an in-plane field of 200 Oe at T=85K as shown in figure 6.12. This is surprising and in apparent conflict with data from Zeldov *et al* [146] suggesting H_m (85K)=27 Oe in a very similar Bi-2212 crystal for $H_{//}$=0. Accounting for the reduction in melting field due to the in-plane field using the equation by Segev *et al* [140] ($H_m = H_m(0) - 4\times 10^{-3} H_{//}$ Oe) one would expect the melting field at $H_{//}$ = 200 Oe to be further suppressed to $H_m \sim$ 26.2 Oe. Hence there appears to be a significant discrepancy here which demands further detailed investigation.

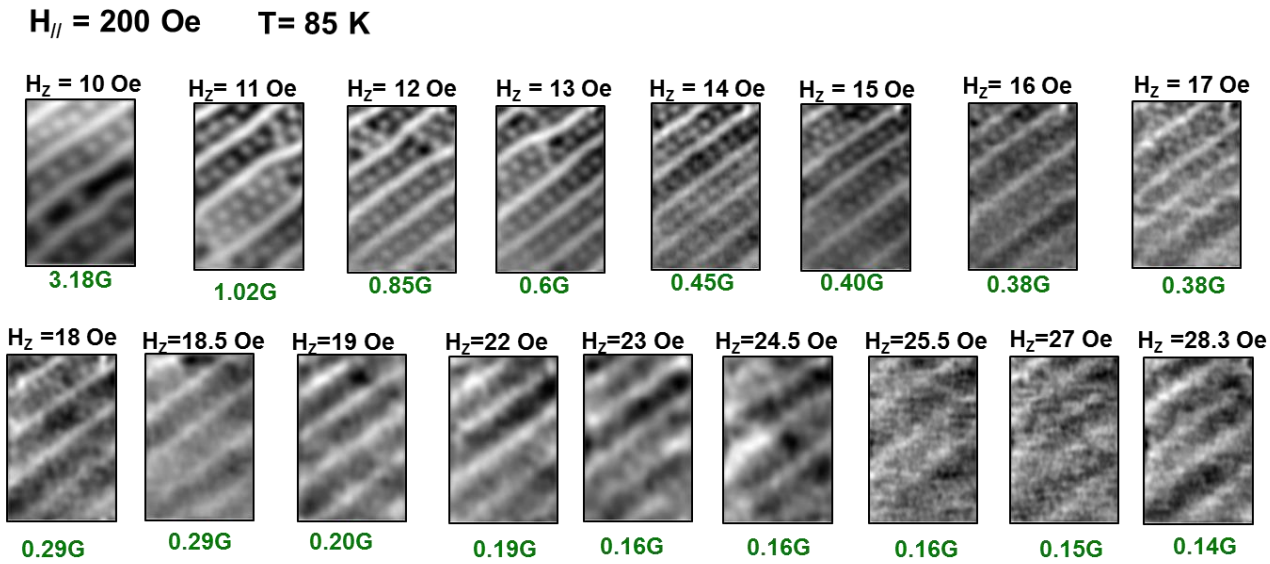

(a)

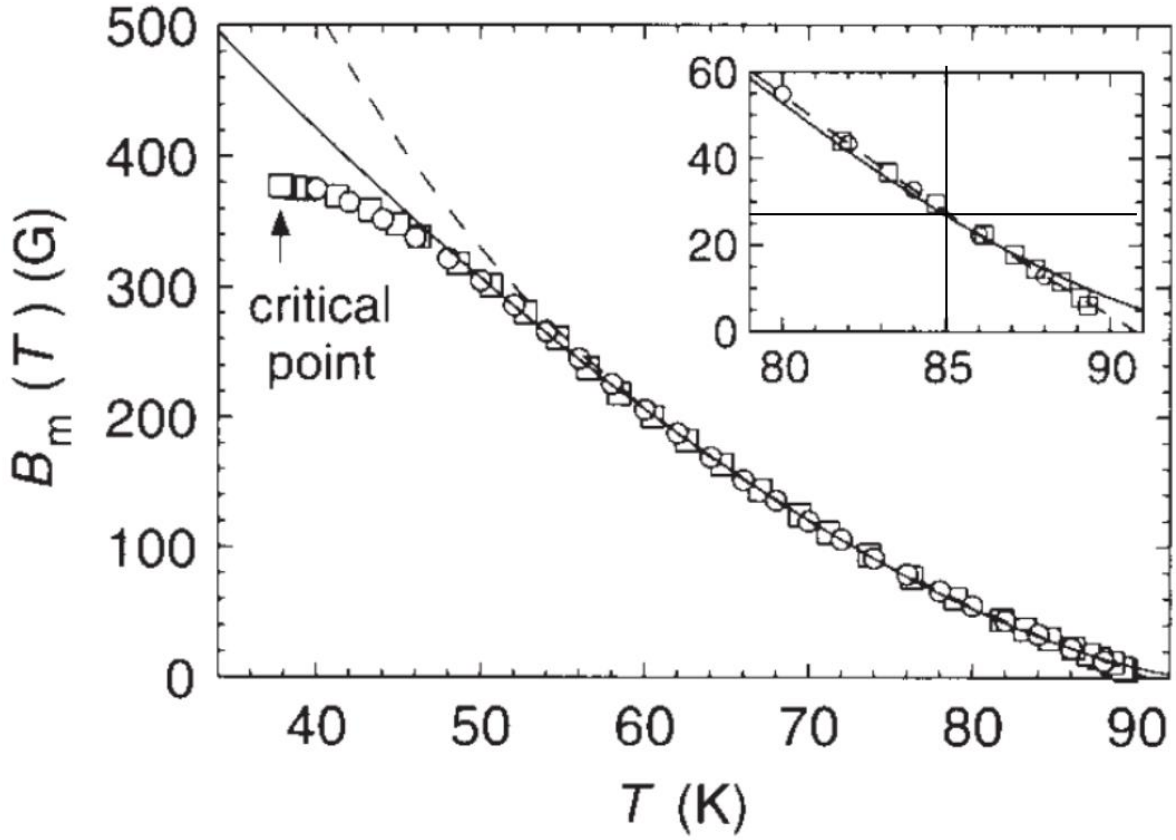

(b)

Figure 6.12: (a) SHPM images at different values of H_z indicate that JV chains survive up to at least 28.3 Oe at $H_{//}$=200 Oe and T=85K. Image grayscales are recorded below in green. (b) B_m versus T for an optimally doped Bi-2212 crystal with no in-plane field. At 85K B_m~ 27G, and should decrease with applied in-plane field (Data reproduced from Zeldov *et al* .[146]).

6.6. Discussion

In layered superconductors in tilted magnetic fields, there always exists an interaction between PVs in adjacent layers, through the magnetic field associated with the vortices. Therefore the tilt of a vortex line can be realized only as a set of kinks connecting the PVs in different layers. The kink is nothing else than a short piece of Josephson vortex in the a-b plane [151]. At low *c*-axis fields and high anisotropy, pancake vortices do not affect the structure of JV's very much. Nevertheless, the interaction energy between a pancake stack and a JV (the crossing energy) is finite, causing striking observable effects, including the formation of the mixed chain-lattice state. Hence applied *c*-axis fields in the range H_z~ 0.5–10 G have been combined with in-plane fields up to 700 G to investigate a previously little studied regime. Moreover very few studies have exploited SHPM to study crossing lattices in Bi-2212 with single vortex resolution.

The lattice structure of a single chain is mainly determined by the ratio of the London ($\lambda \equiv \lambda_{ab}$) and Josephson ($\lambda_J$=$\gamma s$) lengths, α= λ/λ_J which depends on γ, where γ is the anisotropy parameter and *s* the CuO_2 bilayer spacing. The internal structure of an isolated interacting chain depends on the ratio α and is relatively simple in two limiting cases. At small α the chain consists of a 'crossing' array of Josephson vortex and pancake vortex stacks. At large α it is composed of 'tilted' pancake vortex stacks [152].

Koshelev [57] calculated that γ_{eff} depended on the out-of-plane field H_z (or B_z=$\mu_0 H_z$) as shown in equation 6.2. Here B_λ is given by

$B_\lambda = \frac{\Phi^\circ}{4\pi\lambda^2} \ln \frac{r_{cut}}{r_w}$; where r_{cut} = min(a, λ)= λ and a=PV lattice spacing.

This predicts that γ_{eff} for the JV lattice depends on $(B_z)^{-0.5}$ (or $(H_z)^{-0.5}$). This cannot agree exactly with what we see. γ_{eff} can be found from equation 6.1 in the following manner:

$\frac{dC_y}{d(\sqrt{(H_{//})})} = (\frac{\sqrt{3}\ \gamma_{eff}\ \Phi_\circ}{2})^{0.5}$ and the $(\text{slope})^2 = (\frac{\sqrt{3}\ \gamma_{eff}\ \Phi_\circ}{2})$, where the slope is the gradient of each curve at a given H_z in figure 6.6.

As a result, the range of measured values of γ_{eff} spans from 490 -1050 and only weakly depends on vortex dithering. Koshelev's theory predicts that the effective gamma as shown in figure 6.7, exhibits a smooth behaviour qualitatively similar to what is found here. γ is an intrinsic value of the anisotropy of the JV lattice without interactions with PVs.

Koshelev [152] calculated JV/PV structures as a function of $\alpha = \lambda/\lambda_J$. These are shown in figure 6.13 for small α on the left and, large α on the right. In the range $0.5 \leq \alpha \leq 0.65$ he found that at very small PV densities the chains are magnetically homogeneous and separate pancake stacks are not resolved. When the external field exceeds a certain critical value, crystallites of pancake stacks are suddenly formed along the chains and the flux density in these crystallites is approximately ten times higher than the flux density in the homogeneous chains. In our experiments we estimate that $\alpha \sim 0.5$ and hence nominally falls in the regime $0.5 \leq \alpha \leq 0.65$. Certainly the systematic dependence of our PV/JV system on H_z agrees quite well with the predictions in this limit.

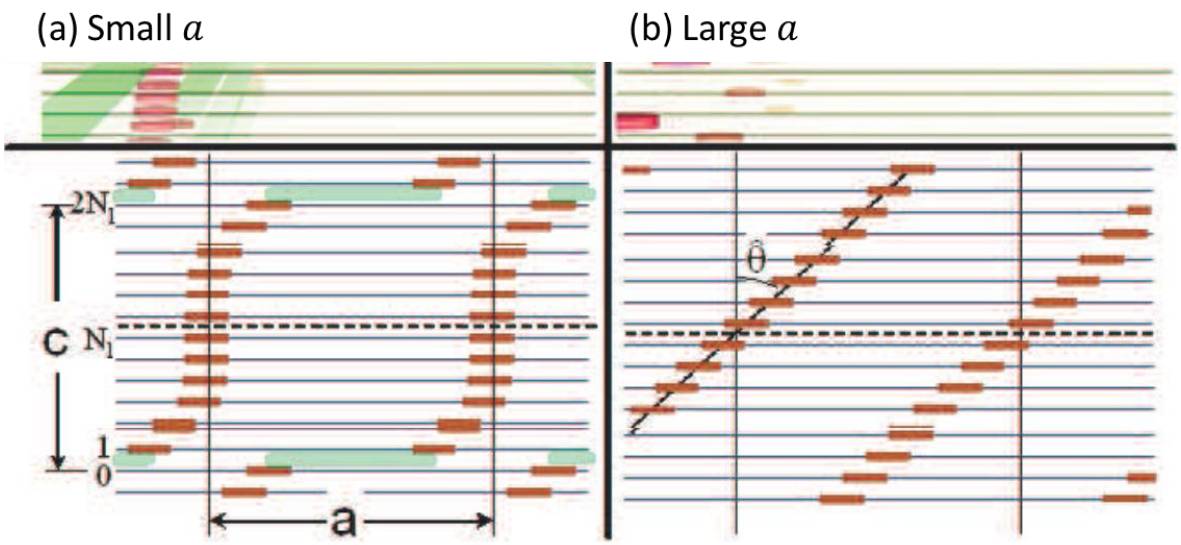

Figure 6.13: sketches of (a) crossing and (b), tilted vortex chains at two limiting values of α [152].

Previous theoretical investigations have derived the different phases in figure 6.14. The kinked lines have lower energy at very large a, a/λ_J > 14.81 and as a is decreased crossing chains smoothly transform back into tilted chains.

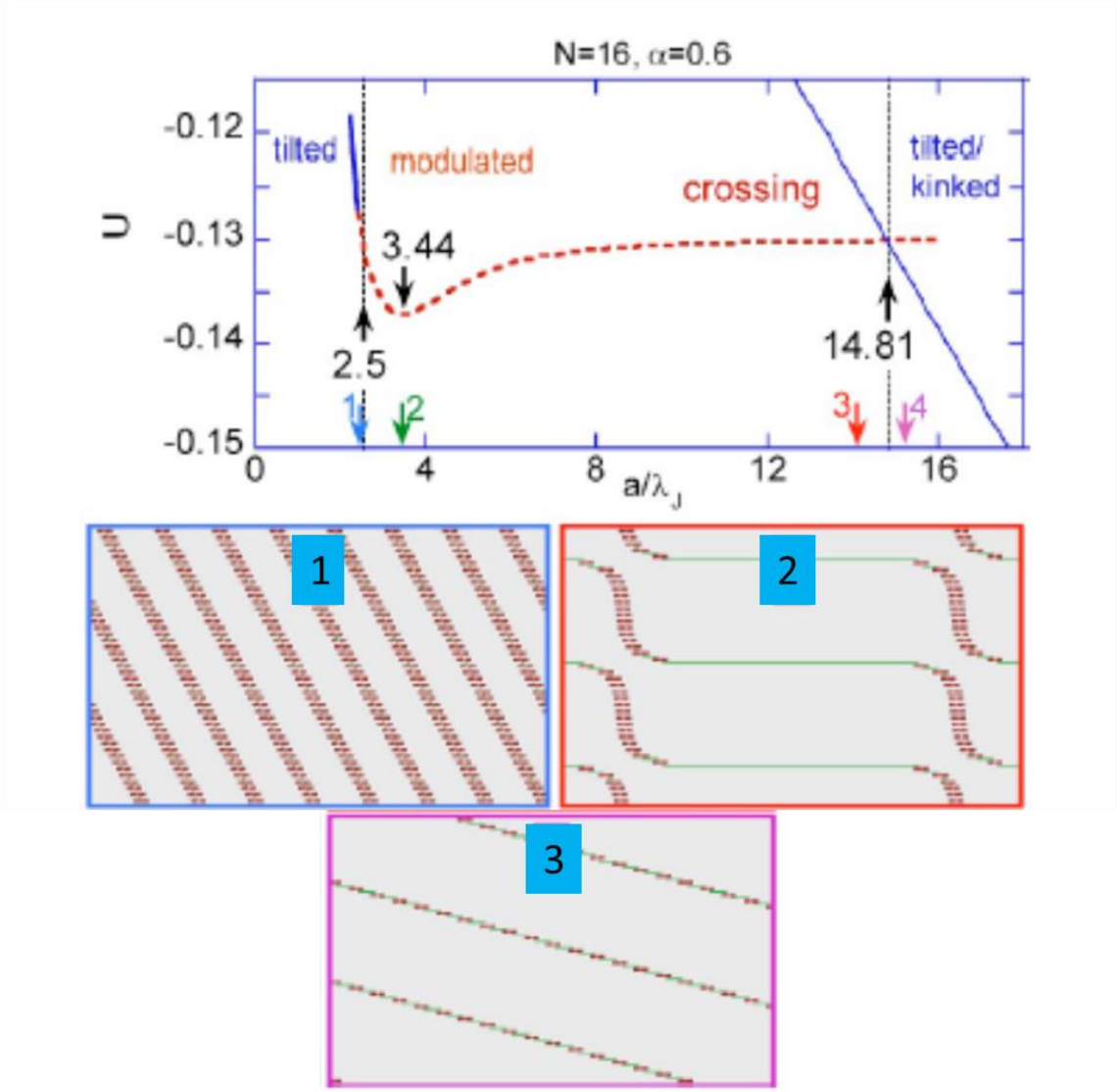

Figure 6.14: Energy profile and sketches showing different phases at small and large pancake separations a, (1) Tilted chains, (2) Crossing chains (3) Tilted chains (reproduced from Koshelev , reference [152])

The three characteristic regions in Koshelev's phase diagram are also observed in our experiments as illustrated in figure 6.15.

1) Very low amplitude streaks indicate the positions of the JV chains at very low H_z. This corresponds to tilted chains.

2) As H_z is increased to ~0.5-1Oe very intense, well-resolved crossing PVs are observed along the JV chains. This corresponds to crossing PVs with S-shaped kinks where the PV stack intersects each JV.

3) For H_z >2Oe individual vortex resolution is lost along the JV chains when the system has reverted to tilted chains.

A sequence of images illustrating these three regions in our experiment is shown in figure 6.15.

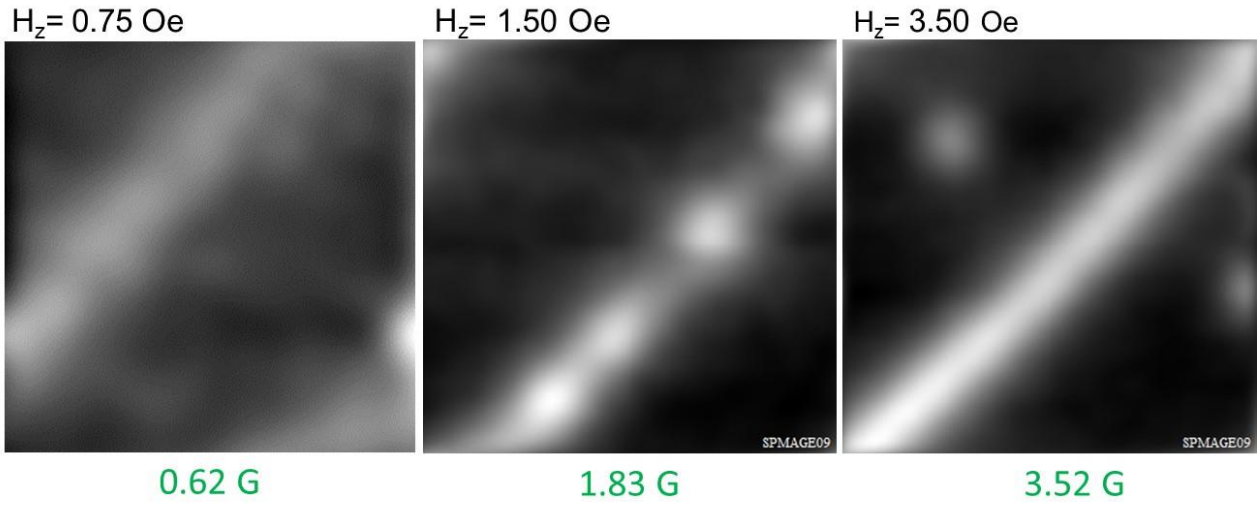

Figure 6.15: SHPM images of a Bi-2212 single crystal as a function of H_z at $H_{//}$ = 50 Oe at T= 85K. The image size is ~20x20 μm^2. Image greyscales are recorded below in green.

The qualitative description for these phases is as follows. When the *c*-axis field is very small, tilted chains are realized in which the Pancake vortex lines are straight and tilted. However, when the *c*-axis field is increased these low-density tilted chains transform by a first-order phase transition into strongly deformed crossing chains. This transition is accompanied by a large jump of the pancake-vortex density. Also, with a further increase of the field, a second-order transition occurs when these crossing chains transform back into tilted chains.

There is currently no theory that describes the oscillations in $C_y(H_z)$, although Alex Koshelev is working on this. However, a qualitative description is as follows. There are two different ways that the system can accommodate more PVs as H_z is increased. Firstly, by decreasing the chain spacing, C_y, and increasing the chain density ($\propto 1/C_y$). This is essentially a continuous change which trades off a reduction in repulsive PV-PV interaction energy (on the JV chains) against some loss of attractive PV/JV energy. Secondly, by creating one (or more) rows of free PVs between the chains. This happens when the interaction energy to put another PV on a chain is higher than to create a free interstitial PV. In practice the competition

between these two mechanisms appears to be quite complicated. In experiments as one increases H_z, C_y initially decreases and then suddenly snaps open again when the first free PV row forms. Clearly when the first row of interstitial PVs forms the system somehow overcompensates and takes extra PVs off the JV chains, allowing the JV stacks to move apart again (and decrease their density). After this C_y starts to decrease again until the second row forms etc giving rise to a "sawtooth-like" dependence of C_y on H_z.

The accepted view is that the JV lattice should melt as soon as the PV system melts as mobile PVs kill JV supercurrents. However, the observation of clear JV chains at very high $H_z > H_m$ (PV) suggests that this may not be entirely correct. Currently no theory exists to address this point but one could speculate that perhaps the JV lattice can survive intact even once the PV system has melted.

Chapter seven

Final conclusions and future work

7.1. Conclusions

In conclusion, the fabrication of sub-micron Bi-Hall effect sensors using electron beam lithography and lift-off techniques with active sizes in the range 0.1 - 2 μm has been demonstrated. The key figures of merit of our sensors have been measured as a function of device dimensions for two different film thicknesses, revealing that the minimum detectable fields of our smallest devices are superior to those fabricated by FIB milling of continuous Bi films. These sensors look very promising for applications in high resolution room temperature scanning Hall probe microscopy, and a number of ways in which their performance could be improved still further are discussed below.

SHPM was used to study interacting JV-PV matter in highly anisotropic $Bi_2Sr_2CaCu_2O_{8+\delta}$ single crystals in very high in-plane fields. For very high values of $H_{//}$ the JV stacks are close enough together that the PVs trapped on adjacent chains interact strongly. In this regime the JV stack spacing becomes dependent on ***both*** in-plane and out-of-plane (= PV density) fields, not just on $(H_{//})^{-0.5}$ as is generally assumed. The structure of JV stacks 'decorated' with PVs was studied at very high in-plane fields while the out-of-plane field was gradually increased. Our experiments indicate that decorated JV chains do not 'melt' at H_z=28.3 Oe at an in-plane field of 200 Oe at T= 85K, although one would expect the melting field to be $H_m \sim 26.2$ Oe. In our experiments, in our range of applied fields, the regime $0.50 \leq \alpha = \lambda_{ab}/\gamma s \leq 0.65$ has been investigated. These measurements are giving us unique new insights into the properties of crossing vortex lattices in highly anisotropic cuprate superconductors at high Josephson vortex densities.

7.2. Possible future developments in nanoscale Hall sensors for applications in SHPM.

The Fabrication of Hall cross sensors with width in the range 20-90 nm should be explored by electron beam lithography and lift-off processes, with Bi film thicknesses in the range 10-100nm in order to optimise the key figures of merit at 300K. In order to obtain a much higher Hall coefficient in Bi films, evaporation at very high deposition rates (~10x faster) should be investigated. High growth rates would also be expect to yield a finer-grained microstructure leading to less current inhomogeneity and lower offset resistances.

These studies should also be repeated with different thin films such as InSb, InAs with variable film thickness to study Hall coefficients, minimum detectable fields and noise characteristics at high and low temperatures. The use of FIB milling is believed to significantly increase the current inhomogeneity in small devices and it was found that devices smaller than 50nm were not operational, presumably due to damage and Ga^{+} ion incorporation during FIB milling. Nevertheless FIB milling and deposition technologies many prove to be able to realise smaller Hall effect sensors than EBL/lift-off and this should be further explored.

7.3. Possible future areas for investigation in interacting vortex lattices in highly anisotropic superconductors.

Microscopic Hall sensors are valuable tools for investigating the magnetic properties of ferromagnetic and superconducting micro- and nano-systems. It was shown that when nanoscale Hall probes are incorporated in scanning Hall probe microscopes, they offer a powerful magnetic visualization tool, having certain advantages and disadvantages with respect to other magnetic imaging techniques which are discussed.

Much could be learned by extending this work to image the interacting JV/PV matter in Bi-2212 at still higher in-plane fields $\gg$ 700 Oe and out-of-plane fields $\gg$ 10 Oe. Also, the vortex lattice melting field/temperature has been measured here as a function of magnetic field. Our results suggest that it would be valuable to study the melting of JVs in a Bi-2212 sample more systematically as a function of temperature at fixed in/out-of-plane fields. In addition, one could use SHPM to search for vortex melting in different materials such as magnesium diboride (MgB_2) or the Fe – based superconductors.

There are a number of natural extensions of this work. In the Bi-2212 system, for instance, the size and shape of mesostructures could be systematically varied to establish the effect of shape on vortex melting and the mesoscopic/macroscopic crossover point. A particularly rich source of new physics is expected from Bi-2212 mesostructures in tilted fields, where the attraction between out-of-plane pancake vortices and in-plane Josephson vortices competes with the effects of quantum confinement. These studies could also be extended to the Bi-2223 phase with lower anisotropy than Bi-2212.

7.4. List of publications

1- Fabrication of nanoscale Bi Hall sensors by lift-off techniques for applications in scanning probe microscopy .Mohammed, H.A.; Bending, S.J. .Semiconductor Science and Technology, 1 August 2014, Vol.**29** (8).

2- A manuscript is in preparation with a provisional title of "Interacting vortex structures in a highly anisotropic superconductor at high in-plane fields".

Bibliography

[1] H. K. Onnes, Leidden Comm, 120b (1911).
[2] H. K. Onnes, Commun. Phys. Lab **12**, 120 (1911).
[3] H. K. Onnes, Nobel lecture **4** (1913).
[4] W. Meissner and R. Ochsenfeld, Die Naturwissenschaften **21**, 787 (1933).
[5] F. London and H. London, Royal Society of London (London) **A149** (1935).
[6] V. L. Ginzburg and L. D. Landau, Zh. Eksperim. i Teor. Fiz **20** (1950).
[7] A. A. Abrikosov, Sov. Phys. JETP **5**, 1174 (1957).
[8] J. Bardeen, L. N. Cooper, and J. R. Schrieffer, Physical Review **108**, 1175 (1957).
[9] G. Bednorz and K. Müller, Z. Phys **B 64**, 189 (1986).
[10] M. Tinkham and V. Emery, Physics Today **49**, 74 (1996).
[11] V. Shamrai, Inorganic Materials: Applied Research **4**, 273 (2013).
[12] A. Schilling, M. Cantoni, J. D. Guo, and H. R. Ott, Nature **363**, 56 (1993).
[13] J. Nagamatsu, N. Nakagawa, T. Muranaka, Y. Zenitani, and J. Akimitsu, Nature **410**, 63 (2001).
[14] Y. Kamihara, T. Watanabe, M. Hirano, and H. Hosono, Journal of the American Chemical Society **130**, 3296 (2008).
[15] Z.-A. Ren *et al.*, EPL (Europhysics Letters) **83**, 17002 (2008).
[16] S. Uchida, J. Phys. Soc. Jpn. **77**, 9 (2008).
[17] W. Meissner and R. Ochsenfeld, Naturwissenschaften **21**, 787 (1933).
[18] D. Shoenberg, Proceedings of the Royal Society of London. Series A-Mathematical and Physical Sciences **155**, 712 (1936).
[19] A. Marouchkine, Cambridge In% ternational Science Publishing, Cambridge (2004).
[20] T. Sheahen, *Introduction to high-temperature superconductivity* (Springer, 1994).
[21] D. R. Tilley and J. Tilley, *Superfluidity and Superconductivity* (Adam Hilger, Bristol and Boston 1986).
[22] A. C. Rose-Innes and A. C. Rhoderick, *Introduction to Superconductivity* (Pergamon Press, 1978).
[23] M. Tinkham, *Introduction to Superconductivity* (McGraw-Hill, New York, 1996), 2nd edn.
[24] V. L. G. a. L. D. Landau, Zh. Eksperim. i. Teor. Fiz. **20**, 1064 (1950).

[25] A. Mourachkine, *Room-temperature superconductivity* (Cambridge Int Science Publishing, 2004).
[26] S. J. Bending, Advances in Physics **48**, 449 (1999).
[27] L. N. Cooper, Physical Review **104**, 1189 (1956).
[28] J. Bardeen, L. N. Cooper, and J. R. Schrieffer, Physical Review **106**, 162 (1957).
[29] J. Bardeen, L. N. Cooper, and J. R. Schrieffer, Physical Review **108**, 1175 (1957).
[30] E. Fermi, Z. Physik **48**, 73 (1928).
[31] M. Cyrot and D. Pavuna, *Introduction to superconductivity and high-Tc materials* 1992).
[32] F. J. Owens and C. P. Poole, *The new superconductors* (Springer, 2002).
[33] M. H. Badr, (2003).
[34] A. Campbell and J. Evetts, Advances in Physics **21**, 199 (1972).
[35] P. Ford and G. Saunders, Contemporary Physics **38**, 63 (1997).
[36] Y. Yeshurun, A. Malozemoff, and A. Shaulov, Reviews of Modern Physics **68**, 911 (1996).
[37] M. A. Roseman, Department of Physics, McGill University, 2001.
[38] D. Cole, S. Bending, S. Savel'Ev, T. Tamegai, and F. Nori, EPL (Europhysics Letters) **76**, 1151 (2006).
[39] D. Feinberg, Physica C: Superconductivity **194**, 126 (1992).
[40] J. Loudon and P. Midgley, Ultramicroscopy **109**, 700 (2009).
[41] R. P. Huebener, *Magnetic flux structures in superconductors: extended reprint of a classic text* (Springer, 2001), Vol. 6.
[42] J. Bardeen and M. J. Stephen, Physical Review **140**, A1197 (1965).
[43] P. W. Anderson and Y. B. Kim, Reviews of Modern Physics **36**, 39 (1964).
[44] A. Abrikosov, L. Gorkov, and I. Dzyaloshinski, JETP **12**, 1243 (1961).
[45] P. Anderson and Y. Kim, Reviews of modern physics **36**, 39 (1964).
[46] Z . Z. Sheng and A. M. Hermann, Nature **332**, 55 (1988).
[47] A. Chubukov, D. Pines, and J. Schmalian, Conventional and High-Tc Superconductors, vol **1**, 495 (2003).
[48] C. Kittel and P. McEuen, *Introduction to solid state physics* (Wiley New York, 1996), Vol. 7.
[49] M. Connolly, University of Bath, 2008.
[50] L. Cohen and H. J. Jensen, Reports on Progress in Physics **60**, 1581 (1997).
[51] L. Bulaevskii and J. R. Clem, Physical Review B **44**, 10234 (1991).
[52] J. Clem, Superconductor Science and Technology **11**, 909 (1998).
[53] L. Bulaevskii, M. Ledvij, and V. Kogan, Physical review letters **68**, 3773 (1992).
[54] G. Blatter, M. Feigel'Man, V. Geshkenbein, A. Larkin, and V. M. Vinokur, Reviews of Modern Physics **66**, 1125 (1994).
[55] L. Bulaevskii, M. Ledvij, and V. Kogan, Physical Review B **46**, 366 (1992).
[56] A. Grigorenko, S. Bending, T. Tamegai, S. Ooi, and M. Henini, Nature **414**, 728 (2001).
[57] A. Koshelev, Physical review letters **83**, 187 (1999).
[58] A. Buzdin and I. Baladie, Physical review letters **88**, 147002 (2002).
[59] V. Vlasko-Vlasov, A. Koshelev, U. Welp, G. Crabtree, and K. Kadowaki, Physical Review B **66**, 014523 (2002).
[60] A. Crisan, S. J. Bending, and T. Tamegai, Superconductor Science and Technology **21**, 015017 (2008).
[61] V. K. Vlasko-Vlasov, A. Koshelev, U. Welp, G. W. Crabtree, and K. Kadowaki, Physical Review B **66**, 014523 (2002).
[62] P. G. Björnsson, Stanford University, 2005.
[63] A. Tonomura, Japanese journal of applied physics **34**, 2951 (1995).
[64] A. Tonomura *et al.*, Nature **412**, 620 (2001).
[65] F. Bitter, Physical Review **38**, 1903 (1931).
[66] U. Essmann and H. Trauble, Physics Letters **24A**, 526 (1967).
[67] E. Yasuda, N. Chikumoto, Y. Nakayama, K. Kishio, T. Nagatomo, and M. Murakami, Physica C: Superconductivity **357**, 564 (2001).

[68] A. Hubert and R. Schafer, *The analysis of magnetic microstructure* (Spring Berlin, New York, 1998).
[69] S. Porthun, L. Abelmann, and C. Lodder, Journal of magnetism and magnetic materials **182**, 238 (1998).
[70] C. Bolle, P. Gammel, D. Grier, C. Murray, D. Bishop, D. Mitzi, and A. Kapitulnik, Physical review letters **66**, 112 (1991).
[71] J. Bland, M. Padgett, R. Butcher, and N. Bett, Journal of Physics E: Scientific Instruments **22**, 308 (1989).
[72] C. Shearwood, A. Mattingley, and M. Gibbs, Journal of magnetism and magnetic materials **162**, 147 (1996).
[73] C. A. Fowler Jr and E. M. Fryer, Physical Review **94**, 52 (1954).
[74] F. Schmidt, W. Rave, and A. Hubert, Magnetics, IEEE Transactions on **21**, 1596 (1985).
[75] Y. Martin and H. K. Wickramasinghe, Applied Physics Letters **50**, 1455 (1987).
[76] D. Vasyukov *et al.*, arXiv preprint arXiv:1308.0694 (2013).
[77] D. Vasyukov *et al.*, Nature nanotechnology **8**, 639 (2013).
[78] V. Mihalache, M. Dede, A. Oral, and V. Sandu, Physica C: Superconductivity **468**, 832 (2008).
[79] M. Dede, K. Urkmen, and A. Oral, in *Magnetics Conference, 2005. INTERMAG Asia 2005. Digests of the IEEE International* (IEEE, 2005), pp. 199.
[80] A. Sandhu, H. Masuda, K. Kurosawa, A. Oral, and S. Bending, Electronics Letters **37**, 1335 (2001).
[81] R. Broom and E. Rhoderick, Proceedings of the Physical Society **79**, 586 (1962).
[82] H. Coffey, Cryogenics **7**, 73 (1967).
[83] A. Geim, S. Bending, and I. Grigorieva, Physical review letters **69**, 2252 (1992).
[84] S. Bending, K. Von Klitzing, and K. Ploog, Physical review letters **65**, 1060 (1990).
[85] S. Bending, K. von Klitzing, and K. Ploog, Physical Review B **42**, 9859 (1990).
[86] D. Brawner and N. Ong, Journal of applied physics **73**, 3890 (1993).
[87] J. Siegel, J. Witt, N. Venturi, and S. Field, Review of scientific instruments **66**, 2520 (1995).
[88] A. Oral, S. Bending, and M. Henini, Journal of Vacuum Science & Technology B **14**, 1202 (1996).
[89] A. Oral, S. Bending, and M. Henini, Applied physics letters **69**, 1324 (1996).
[90] A. Beer, Solid-State Electronics **9**, 339 (1966).
[91] J. Bardeen, R. Kümmel, A. Jacobs, and L. Tewordt, Physical Review **187**, 556 (1969).
[92] R. S. Popovic, *Hall effect devices, magnetic sensors and characterization of semiconductors* (Adam Hilger 1990).
[93] R. Popović, Sensors and Actuators **17**, 39 (1989).
[94] Z. Koziol and J. Franse, Magnetics, IEEE Transactions on **30**, 1172 (1994).
[95] P. Horowitz and W. Hill, *The art of electronics* (Cambridge university press, 1989).
[96] F. Hooge, Electron Devices, IEEE Transactions on **41**, 1926 (1994).
[97] C. Hicks, L. Luan, K. Moler, E. Zeldov, and H. Shtrikman, Applied Physics Letters **90**, 133512 (2007).
[98] K. Vervaeke, E. Simoen, G. Borghs, and V. Moshchalkov, Review of Scientific Instruments **80**, 074701 (2009).
[99] J. Hook and H. Hall, (John Wiley and Sons.
[100] C. J. Chen, *Introduction to scanning tunneling microscopy* (Oxford University Press, USA, 1993), Vol. 4.
[101] C. Harnagea, *Local piezoelectric response and domain structures in ferroelectric thin films investigated by voltage-modulated force microscopy* (Universitäts-und Landesbibliothek, 2001).
[102] L. T. S. H. P. Microscope, (Oxford, UK www. nanomagnetics-inst. com.
[103] H. Scheel, G. Binning, and H. Rohrer, Journal of Crystal Growth **60**, 199 (1982).
[104] J. Pearl, Journal of Applied Physics **37**, 4139 (1966).
[105] S. Kweon, *Study of a ferromagnetic semiconductor by the Scanning Hall Probe Microscope* (ProQuest, 2008).
[106] B. Elkonin, Cryogenics **42**, 147 (2002).

[107] A. Oral, S. Bending, and M. Henini, Journal of Vacuum Science & Technology B: Microelectronics and Nanometer Structures **14**, 1202 (1996).
[108] H. Guillou, A. Kent, G. Stupian, and M. Leung, Journal of applied physics **93**, 2746 (2003).
[109] M. Boffoué, B. Lenoir, A. Jacquot, H. Scherrer, A. Dauscher, and M. Stölzer, Journal of Physics and Chemistry of Solids **61**, 1979 (2000).
[110] H. J. Levinson, *Principles of lithography* (SPIE press, 2005), Vol. 146.
[111] G. Gerlach and W. Dotzel, *Introduction to microsystem technology: a guide for students* (Wiley, 2008).
[112] J. CHLUMSKÁ, V. KOLAŘÍK, S. KRÁTKÝ, M. MATĚJKA, M. URBÁNEK, and M. HORÁČEK.
[113] Z. Cui, *Micro-nanofabrication: technologies and applications* (Higher Education Press Beijing:, 2005).
[114] N. M. Prinsloo, J. P. Engelbrecht, T. N. Mashapa, and M. J. Strauss, Applied Catalysis A: General **344**, 20 (2008).
[115] J. C. Mallinson, *The Foundations of Magnetic Recording 2E* (Academic press, 1993).
[116] K. Novoselov, S. Morozov, S. Dubonos, M. Missous, A. Volkov, D. Christian, and A. Geim, Journal of applied physics **93**, 10053 (2003).
[117] M. Rudolph and J. Heremans, Applied Physics Letters **100**, 241601 (2012).
[118] J. Saenz, N. Garcia, and J. Slonczewski, Applied physics letters **53**, 1449 (1988).
[119] J. Gregory, S. Bending, and A. Sandhu, Review of scientific instruments **73**, 3515 (2002).
[120] A. Sandhu, H. Sanbonsugi, I. Shibasaki, M. Abe, and H. Handa, Japanese journal of applied physics **43**, L868 (2004).
[121] A. Grigorenko, S. Bending, J. Gregory, and R. Humphreys, Applied Physics Letters **78**, 1586 (2001).
[122] O. Kazakova, V. Panchal, J. Gallop, P. See, D. Cox, M. Spasova, and L. Cohen, Journal of Applied Physics **107**, 09E708 (2010).
[123] O. Kazakova, J. C. Gallop, D. C. Cox, E. Brown, A. Cuenat, and K. Suzuki, Magnetics, IEEE Transactions on **44**, 4480 (2008).
[124] A. Pross, A. Crisan, S. Bending, V. Mosser, and M. Konczykowski, Journal of applied physics **97**, 096105 (2005).
[125] R. N. Goren and M. Tinkham, Journal of Low Temperature Physics **5**, 465 (1971).
[126] A. Sandhu, K. Kurosawa, M. Dede, and A. Oral, Japanese journal of applied physics **43**, 777 (2004).
[127] D. Petit, D. Atkinson, S. Johnston, D. Wood, and R. Cowburn, in *Science, Measurement and Technology, IEE Proceedings*- (IET, 2004), pp. 127.
[128] D. Petit, C. Faulkner, S. Johnstone, D. Wood, and R. Cowburn, Review of scientific instruments **76**, 026105 (2005).
[129] M. Kubota, Y. Tokunaga, N. Kanazawa, F. Kagawa, Y. Tokura, and M. Kawasaki, Journal of Applied Physics **114**, 053909 (2013).
[130] G. Jung, M. Ocio, Y. Paltiel, H. Shtrikman, and E. Zeldov, Applied Physics Letters **78**, 359 (2001).
[131] E. Milotti, arXiv preprint physics/0204033 (2002).
[132] V. P. Kunets *et al.*, Journal of applied physics **98**, 014506 (2005).
[133] R. A. Hoffman and D. Frankl, Physical Review B **3**, 1825 (1971).
[134] R. Koseva, I. Mönch, D. Meier, J. Schumann, K.-F. Arndt, L. Schultz, B. Zhao, and O. Schmidt, Thin Solid Films **520**, 5589 (2012).
[135] A. Buzdin and D. Feinberg, Journal de Physique **51**, 1971 (1990).
[136] M. Hellerqvist, S. Ryu, L. Lombardo, and A. Kapitulnik, Physica C: Superconductivity **230**, 170 (1994).
[137] I. Grigorieva, J. Steeds, and K. Sasaki, Physical Review B **48**, 16865 (1993).
[138] V. Vlasko-Vlasov, A. Koshelev, U. Welp, G. Crabtree, and K. Kadowaki, Physical Review B **66**, 014523 (2002).
[139] A. Grigorenko, S. Bending, A. Koshelev, J. R. Clem, T. Tamegai, and S. Ooi, Physical review letters **89**, 217003 (2002).

[140] Y. Segev, Y. Myasoedov, E. Zeldov, T. Tamegai, G. Mikitik, and E. Brandt, Physical review letters **107**, 247001 (2011).
[141] S. Butsch, E. Zeldov, and T. Nattermann, EPL (Europhysics Letters) **103**, 47007 (2013).
[142] N. Avraham *et al.*, Nature **411**, 451 (2001).
[143] S. Bending, A. Grigorenko, I. Crisan, D. Cole, A. Koshelev, J. R. Clem, T. Tamegai, and S. Ooi, Physica C: Superconductivity **412**, 372 (2004).
[144] P. Kes *et al.*, Journal de Physique I **6**, 2327 (1996).
[145] E. Brezin, D. Nelson, and A. Thiaville, Physical Review B **31**, 7124 (1985).
[146] E. Zeldov, D. Majer, M. Konczykowski, V. Geshkenbein, V. Vinokur, and H. Shtrikman, Nature **375**, 373 (1995).
[147] L. Balents and D. R. Nelson, Physical Review B **52**, 12951 (1995).
[148] X. Hu and M. Tachiki, Physical review letters **85**, 2577 (2000).
[149] A. Koshelev, Physical review letters **83**, 187 (1999).
[150] J. Mirković, S. Savel'Ev, E. Sugahara, and K. Kadowaki, Physical review letters **86**, 886 (2001).
[151] B. Ivlev, Y. N. Ovchinnikov, and V. Pokrovsky, EPL (Europhysics Letters) **13**, 187 (1990).
[152] A. E. Koshelev, Physical Review B - Condensed Matter and Materials Physics **71**, 174507 (2005).